Photochemical Synthesis and Spectroscopic Analysis of PAH Oligomers

by

Ian James Webster

(Under the Direction of Michael A. Duncan)

Abstract

Laser photochemistry of pressed-pellet samples of polycyclic aromatic hydrocarbons (PAHs) produces covalently bonded oligomers. This chemistry was discovered initially via laser desorption time-of-flight mass spectrometry experiments, which produced masses (m/z) of 2M-2 and 2M-4 (where M is the monomer parent mass). Dimers are believed to be formed from photochemical dehydrogenation and radical polymerization chemistry in the desorption plume. Replication of these ablation conditions at higher throughput allowed PAH dimers of pyrene, perylene, and coronene to be produced and collected in milligram quantities. Differential sublimation provided purification of the dimers and elimination of residual monomers. The purified dimers were investigated with UV−visible, IR, and Raman spectroscopy, complemented by computational studies using density functional theory at the CAM-B3LYP/def2TZV level. Calculations and predicted spectra were calibrated by comparison with the corresponding monomers and used to determine the lowest energy dimer structures. Infrared and Raman

spectroscopy provided few distinctive signatures, but UV−visible spectra detected new transitions for each dimer. The comparison of simulated and experimental spectra allows determination of the most prevalent structures for the PAH dimers. The work presented here provides interesting insights into the spectroscopy of extended aromatic systems and a new strategy for the photochemical synthesis of large PAH dimers.

Index Words: Aromatic compounds, Hydrocarbons, Materials, Monomers, Oligomers

PHOTOCHEMICAL SYNTHESIS AND SPECTROSCOPIC ANALYSIS OF PAH OLIGOMERS

By

IAN JAMES WEBSTER

B.S., University of Georgia, 2014

A Dissertation Submitted to the Graduate Faculty of the University of Georgia in Partial Fulfillment of the Requirements for the Degree

DOCTOR OF PHILOSOPHY

Athens, Georgia

2023

PHOTOCHEMICAL SYNTHESIS AND SPECTROSCOPIC ANALYSIS OF PAH OLIGOMERS

By

IAN JAMES WEBSTER

Major Professor: Michael A. Duncan

Committee: Tina T. Salguero

Geoffrey D. Smith

Electronic Version Approved:

Ron Walcott
Dean of the Graduate School
The University of Georgia
August 2023

Dedication

I dedicate this dissertation to my fiancée who has always inspired me with her commitment to pursuing her goals. Her dedication to becoming a veterinarian has shown me how much effort it truly takes to pursue your dreams and drives me to do the same. Without her inspiration, I doubt I would be where I am today.

I also dedicate this dissertation to my family and friends who have helped to distract me from my worries. My family has helped provide for my needs and most importantly keep me caffeinated for the extent of my graduate career. My friends have provided hours of entertainment that probably should have been better spent trying to graduate that much sooner. Still, I doubt I could have gotten through my time here without their help and compassion.

Acknowledgements

I have learned much under the tutelage of Dr. Michael Duncan. Mostly about the variety of things that must be done to keep a lab up and running. He never let me get bored and always kept me spinning several plates working on one thing or another. I learned a variety of things, many of which I possibly should have learned before starting graduate school.

I am also thankful for the compassion of my committee who despite my many faults have been kind enough to allow me this opportunity. Tina has always been ready and willing whenever I have needed her and thankfully understanding. Geoff was there to step up after misgivings with my prior committee and kind enough to handle issues with little time or explanation. To both I am grateful for this opportunity.

I would also like to thank my coworkers, who helped me to learn the many different instruments and components that we use. Also for finding a project for me when everything else I tried inevitably didn't workout. Although the names have changed over the years, we have always been there for each other to resolve one issue or another.

"It must be Thursday. I never could get the hang of Thursdays."

- Douglas Adamas, *The Hitchhiker's Guide to the Galaxy*

Table of Contents

Page

Chapter 1

Introduction

The production of polycyclic aromatic hydrocarbons (PAHs) is an interesting area of research due to the challenges present in size-selective synthesis. A variety of PAHs are naturally occurring byproducts from hydrocarbon combustion, automobile exhaust, and crude oil mining.[1-4] Although PAHs are abundant in these different sources, it is rare to see any PAHs larger than coronene ($C_{24}H_{12}$). PAHs of larger sizes are not naturally occurring, but can be synthesized.[5-6] Currently, larger PAHs are synthesized commonly by means of the Scholl reaction, which can be used to form polymer chains.[7] Although polymers have been used for making plastics, the synthesis of size-selected PAHs is still limited in production.[8-10] The production of discrete large PAHs could be useful for the production of nanographene,[11-21] improvement of photovoltaic cells,[22-38] and identification of astrochemical mysteries.[39-54] This dissertation focuses on the synthesis of PAH dimers through a photochemical pathway not yet explored.

The production of sophisticated integrated circuits is based around a procedure known as photolithography. The photolithography process is limited in its capacity based on the diffraction limits of lasers that are available. As laser technology limits the possible future improvements to integrated circuits, the production process may be improved through the use of graphene with its low bandgap.[11-14] Through control of the size and shape of small graphene pieces, known as nanographene, the bandgap can be adjusted to meet the needs of the electronic devices and made to fit the computer's integrated circuit.[15-16] Improvements in this field are largely determined by the ability to produce specific size-selected nanographene pieces as needed.[17-21]

The future of photovoltaic cells is dependent on the production of more efficient energy sources. One possible option for improving these solar powered cells is the development of better singlet fission sources.[22-25] Singlet fission is the process of a singular excited molecule in a singlet electronic state interacting with a second molecule causing both molecules to end up in an excited triplet state. This process doubles the number of excited molecules present and can occur on a pico- to femtosecond timescale since it is spin allowed. Several PAHs, especially linear molecules like pentacene, have been shown to undergo singlet fission.[26-32] The study of longer dimerized PAHs may find future more efficient singlet fission options to progress the development of photovoltaic cells.[33-38]

In the field of astrochemistry, small carbon based molecules, such as C_3 and C_5, are well known to be abundant, especially in carbon-rich dust clouds.[39] Large carbon-based molecules, such as C_{60} cation have also been discovered and identified as a carrier of a diffuse interstellar band (DIB).[40-44] Carbon based molecules between these two sizes have been speculated to exist, but identification of specific molecules has been challenging for astrochemists. There is debate over whether these molecules would develop in a top-down method in which large molecules like C_{60} form in carbon-rich stars and break down into smaller carbon-based molecules or a bottom-up approach in which the small carbon molecules collide and eventually build into larger molecules like C_{60}.[45-51] Regardless of which process is accurate, the presence of PAHs in the interstellar medium is an important field of study. A number of infrared emission peaks, known as the unassigned infrared bands (UIRs), remain a curious problem for astrochemists, though the region in which these signals have been detected is associated with the infrared emission of PAHs.[45-52] Still, the specific molecules responsible have yet to be discovered, and many people speculate that these spectra may be the result of larger PAHs than are commercially available for

study. The development of improved methods for producing large PAHs has the potential to significantly impact other fields of chemistry.

This work focuses on the synthesis of pyrene, perylene, and coronene dimers with an excimer laser and the subsequent identification through spectroscopy.[53] PAH dimers were detected through mass spectrometry studies and further mass spectrometry scans were used to assess the purity of the synthesized dimers. The infrared, Raman, and UV-Visible absorption spectra of the synthesized dimers were measured. Density functional theory (DFT) computations were performed to predict the most likely dimer structures formed. The resulting dimer structures are used to simulate possible spectroscopic peaks which can be used to identify the produced dimers based on the measured spectra of the synthesized dimers.

References

1. Harvey, R. G. *Polycyclic Aromatic Hydrocarbons: Chemistry and Carcinogenicity*; Cambridge University Press, 1991.
2. Harvey, R. G. *Polycyclic Aromatic Hydrocarbons*. Wiley: New York, 1997.
3. Fetzer, J. C. *Large (C>=24) Polycyclic Aromatic Hydrocarbons,* Volume 158; Winefordner, J. D. Ed.; John Wiley and Sons Inc.: United States of America, 2000.
4. Fetzer, J. *The Chemistry and Analysis of the Large Polycyclic Aromatic Hydrocarbons*, New York: John Wiley and Sons, 2007.
5. Dötz, F.; Brand, J. D.; Ito, S.; Gherghel, L.; Müllen, K. Synthesis of Large Polycyclic Aromatic Hydrocarbons: Variation of Size and Periphery. *J. Am. Chem. Soc.* **2000**, *122*, 7707-7717.
6. Yoshimura, K.; Przybilla, L.; Ito, S.; Brand, J. D.; Wehmeir, M.; Räder, H. J.; Müllen, K. Characterization of Large Synthetic Polycyclic Aromatic Hydrocarbons by MALDI- and LD-TOF Mass Spectrometry. *Macromol. Chem. Phys.* **2001**, *202*, 215-222.
7. Cataldo, F.; Ursini, O.; Angelini, G.; Iglesias-Groth, S. On the Way to Graphene: The Bottom-Up Approach to Very Large PAHs Using the Scholl Reaction. *Fullerenes, Nanotubes, Carbon Nanostruct.* **2011**, *19*, 713-725.
8. Comandini, A.; Abid, S.; Chaumeix, N. Polycyclic Aromatic Hydrocarbon Growth by Diradical Cycloaddition/Fragmentation. *J. Phys. Chem. A* **2017**, *121*, 5921-5931.
9. Shinozaki, A.; Mimura, K.; Nishida, T.; Cody, G. D. Polymerization Mechanism of Nitrogen-Containing Heteroaromatic Compound Under High-Pressure and High-Temperature Conditions. *J. Phys. Chem. A* **2021**, *125*, 376-386.

10. Zatsikha, Y. V.; Blesener, T. S.; King, A. J.; Healy, A. T.; Goff, P. C.; Didukh, N. O.; Blank, D. A; Kovtun, Y. P.; Nemykin, V. N. Fully Conjugated Pyrene-BODIPY and Pyrene-BODIPY-Ferrocene Dyads and Triads: Synthesis, Characterization, and Selective Noncovalent Interactions with Nanocarbon Materials. *J. Phys. Chem B* **2021**, *125*, 360-371.
11. Dresselhaus, M. S.; Dresselhaus, G.; Eklund, P. C. *Science of Fullerenes and Carbon Nanotubes: Their Properties and Applications*; Elsevier Science, 1996.
12. Geim, A. K. Graphene: Status and Prospects. *Science* **2009**, *324*, 1530–1534.
13. Rao, C. N. R.; Sood, A. K.; Subrahmanyam, K. S.; Govindaraj, A. Graphene: The New Two-Dimensional Nanomaterial. *Angew. Chem. Int. Ed.* **2009**, *48*, 7752-7777.
14. Allen, M. J.; Tung, V. C.; Kaner, R. B. Honeycomb Carbon: A Review of Graphene. *Chem. Rev.* **2010**, *110*, 132-145.
15. Anthony, J. E. Functionalized Acenes and Heteroacenes for Organic Electronics. *Chem. Rev.* **2006**, *106*, 5028-5048.
16. Wu, J.; Pisula, W.; Müllen, K. Graphenes as Potential Material for Electronics. *Chem. Rev.* **2007**, *107*, 718-747.
17. Ferrari, A. C.; Meyer, J. C.; Scardaci, V.; Casiraghi, C.; Lazzeri, M.; Mauri, F.; Piscanec, S.; Jiang, D.; Novoselov, K. S.; Roth, S.; Geim, A. K. Raman Spectrum of Graphene and Graphene Layers. *Phys. Rev. Lett.* **2006**, *97*, 187401-187404.
18. Talyzin, A. V.; Anoshkin, I. V.; Krasheninnikov, A. V.; Nieminen, R. M.; Nasibulin, A. G.; Jiang, H.; Kauppinen, E. I. Synthesis of Graphene Nanoribbons Encapsulated in Single-Walled Carbon Nanotubes. *Nano Lett.* **2011**, *11*, 4352-4356.
19. Chen, L.; Hernandez, Y; Feng, X.; Müllen, K. From Nanographene and Graphene

Nanoribbons to Graphene Sheets: Chemical Synthesis. *Angew. Chem. Int. Ed.* **2012**, *51*, 7640-7654.

20. Narita, A.; Wang, X.; Feng, X.; Müllen, K. New Advances in Nanographene Chemistry. *Chem. Soc. Rev.* **2015**, *44*, 6616-6643.
21. Tan, C.; Cao, X; Wu, X.; He, Q.; Yang, J.; Zhang, X.; Chen, J.; Zhao, W.; Han, S.; Nam, G.; et al. Recent Advances in Ultrathin Two-Dimensional Nanomaterials. *Chem. Rev.* **2017**, *117*, 6225-6331.
22. Birks, J. B. *Photophysics of Aromatic Molecules*; Wiley-Interscience, 1970.
23. Brédas, J.; Norton, J. E.; Cornil, J.; Coropceanu, V. Molecular Understandings of Organic Solar Cells: The Challenges. *Acc. Chem. Res.* **2009**, *42*, 1691-1699.
24. Smith, M. B.; Michl, J. Singlet Fission. *Chem. Rev.* **2010**, 110, 6891-6936.
25. Smith, M. B.; Michl, J. Recent Advances in Singlet Fission. *Annu. Rev. Phys. Chem.* **2013**, *64*, 361-386.
26. Burdett, J. J.; Bardeen, C. J. The Dynamics of Singlet Fission in Crystalline Tetracene and Covalent Analogs. *Acc. Chem. Res.* **2013**, *46*, 1312-1320.
27. Yang, C.; Hsu, C. First-Principle Characterization for Singlet Fission Couplings. *J. Phys. Chem. Lett.* **2015**, *6*, 1925-1929.
28. Sanders, S. N.; Kumarasamy, E.; Pun, A. B.; Trinh, M. T.; Choi, B.; Xia, J.; Taffet, E. J.; Low, J. Z.; Miller, J. R.; Roy, X.; Zhu, X.; Steigerwald, M. L.; Sfeir, M. Y.; Campos, L. M. Quantitative Intramolecular Singlet Fission in Bipentacenes. *J. Am. Chem. Soc.* **2015**, *137*, 8965-8972.

29. Margulies, E. A.; Wu, Y.; Gawel, P.; Miller, S. A.; Shoer, L. E.; Schaller, R. D.; Diederich, F.; Wasielewski, M. R. Sub-Picosecond Singlet Exciton Fission in Cyano-Substituted Diaryltetracenes. *Angew. Chem. Int. Ed.* **2015**, *54*, 8679-8683.

30. Sanders, S. N.; Kumarasamy, E.; Pun, A. B.; Steigerwald, M. L.; Sfeir, M. Y.; Campos, L. M. Intramolecular Singlet Fission in Oligoacene Heterodimers. *Angew. Chem. Int. Ed.* **2016**, *55*, 3373-3377.

31. Sakuma, T.; Sakai, H.; Araki, Y.; Mori, T.; Wada, T.; Tkachenko, N. V.; Hasobe, T. Long-Lived Triplet Excited States of Bent-Shaped Pentacene Dimers by Intramolecular Singlet Fission. *J. Phys. Chem. A* **2016**, *120*, 1867-1875.

32. Bhattacharyya, K.; Datta, A. Polymorphism Controlled Singlet Fission in TIPS-Anthracene: Role of Stacking Orientation. *J. Phys. Chem. C* **2017**, *121*, 1412-1420.

33. Casanova, D. Theoretical Modeling of Singlet Fission. *Chem. Rev.* **2018**, *118*, 7164-7207.

34. Hart, S. M.; Silva, W. R.; Frontiera, R. R. Femtosecond Stimulated Raman Evidence for Charge-Transfer Character in Pentacene Singlet Fission. *Chem. Sci.* **2018**, *9*, 1242-1250.

35. Pun, J. K. H.; Gallaher, J. K.; Frazer, L.; Prasad, S. K. K.; Dover, C. B.; MacQueen, R. W.; Schmidt, T. W. TIPS-Anthracene: A Singlet Fission or Triplet Fusion Material? *J. Photonics Energy* **2018**, *8*, 022006.

36. Zhao, X.; Bae, Y. J.; Chen, M.; Harvey, S. M.; Lin, C.; Zhou, J.; Schaller, R. D.; Young, R. M.; Wasielewski, M. R. Singlet Fission in Core-Linked Terrylenediimide Dimers. *J. Chem. Phys.* **2020**, *153*, 244306.

37. He, G.; Busby, E.; Appavoo, K.; Wu, Q.; Xia, J.; Campos, L. M.; Sfeir, M. Charge Transfer States Impact the Triplet Pair Dynamics of Singlet Fission Polymers. *J. Chem. Phys.* **2020**, *153*, 244902.

38. Das, S.; Bhauriyal, P.; Pathak, B. Polycyclic Aromatic Hydrocarbons as Prospective Cathodes for Aluminum Organic Batteries. *J. Phys. Chem. C* **2021**, *125*, 49-57.

39. Allamandola, L. J.; Tielens, A. G. G. M.; Barker, J. R. Polycyclic Aromatic Hydrocarbons and the Unidentified Infrared Emission Bands: Auto Exhaust Along the Milky Way! *Astrophys. J.* **1985**, *290*, L25-L28.

40. Allamandola, L. J.; Tielens, A. G. G. M.; Barker, J. R. Interstellar Polycyclic Aromatic Hydrocarbons: The Infrared Emission Bands, the Excitation/Emission Mechanism, and the Astrophysical Implications. *Astrophys. J., Suppl. Ser.* **1989**, *71*, 733-775.

41. Leger, A.; D'Hendecourt, L.; Defourneau, D. Physics of IR Emission by Interstellar PAH Molecules. *Astron. Astrophys.* **1989**, *216*, 148–164.

42. Hartquist, T. W.; Williams, D. A. *The Molecular Astrophysics of Stars and Galaxies*; International Series on Astron; Clarendon Press, 1998.

43. Henning, T.; Salama, F. Carbon in the Universe. *Science* **1998**, *282*, 2204–2210.

44. Bréchignac, P.; Pino, T.; Boudin, N. Laboratory Spectra of Cold Gas Phase Polycyclic Aromatic Hydrocarbon Cations, and Their Possible Relation to the Diffuse Interstellar Bands. *Spectrochim. Acta - Part A Mol. Biomol. Spectrosc.* **2001**, *57*, 745–756.

45. Malloci, G.; Mulas, G.; Joblin, C. Electronic Absorption Spectra of PAHs up to Vacuum UV. *A&A* **2004**, *426*, 105-117.

46. Tielens, A. G. G. M. *The Physics and Chemistry of the Interstellar Medium*; Cambridge University Press, 2005.

47. Snow, T. P.; Bierbaum V. M. Ion Chemistry in the Interstellar Medium. *Annu. Rev. Anal. Chem.* **2008**, *1*, 229-259.

48. Tielens, A. G. G. M. Interstellar Polycyclic Aromatic Hydrocarbon Molecules. *Annu. Rev. Astron. Astrophys.* **2008**, *46*, 289–337.

49. Draine, B. T. *Physics of the Interstellar and Intergalactic Medium*; Princeton University Press; 2011.

50. Tielens, A. G. G. M.; Snow, T. P. *The Diffuse Interstellar Bands*; Astrophysics and Space Science Library; Springer Netherlands, 2012.

51. Tielens, A. G. G. M. The Molecular Universe. *Rev. Mod. Phys.* **2013**, *85*, 1021-1081.

52. Sandford, S. A.; Nuevo, M.; Bera, P. P.; Lee, T. J. Prebiotic Astrochemistry and the Formation of Molecules of Astrobiological Interest in Interstellar Clouds and Protostellar Disks. *Chem. Rev.* **2020**, *120*, 4616-4659.

53. Webster, I. J.; Beckham, J. L.; Johnson, N. D.; Duncan, M. A. Photochemical Synthesis and Spectroscopy of Covalent PAH Dimers. *J. Phys. Chem. A* **2022**, *126*, 1144-1157.

Chapter 2

Sample Preparation & Mass Spectrometry

The study of PAHs was accomplished through use of laser desorption time-of-flight mass spectrometry (LD-ToF-MS). Commercially available PAH samples were prepared as either a thin film on the mass spectrometer probe tip or as a pressed pellet piece attached to the tip with double-sided tape. Thin film samples were prepared by suspending a few milligrams of commercial PAHs, purchased from Tokyo Chemical Inc. and used without further purification, in a few milliliters of HPLC-grade methanol (Sigma-Aldrich). Suspended samples were pipetted onto a copper mass spectrometer probe tip and left to dry. Multiple drops were added to increase the amount of sample, resulting in the thin film of material on the tip. For comparison, pressed pellet samples were prepared using the same commercial material cast in a ½ in diameter die. Two ½ in. diameter Teflon disks were cut from an unused stock piece for each pellet to prevent cross contamination of the samples. 100-150 mg of material would yield a pressed pellet of 1-3 mm thickness. Small pieces of the pellet were broken off from the full disk and attached onto the copper probe tip with double-sided tape. Both thin film and pressed pellet samples were loaded into a time-of-flight mass spectrometer (Comstock) via an airlock and slowly introduced further into the high vacuum region of the instrument. Samples were then ionized through a laser desorption method.

Laser desorption offers a soft ionization method which reduces the amount of fragmentation of the source sample. Laser desorption of the samples was achieved through a neodymium doped yttrium aluminum garnet (Nd:YAG) laser (New Wave Polaris II) providing

light at 1064 nm frequency doubled or tripled to the 532 nm or 355 nm wavelengths. The laser beam was focused through a 20 cm focal length lens down to a 0.5 mm^2 spot size on the sample tip to desorb the material. The laser pulse energy could be adjusted from 100 to 400 μJ/pulse, with a typical value of 200 μJ/pulse operating at a 10 Hz repetition rate, giving an average irradiance of 40 mJ/cm^2/pulse focused onto the probe tip. The position of the laser was periodically adjusted to ensure fresh sample area was being desorbed.

Nd:YAG lasers operate at a variety of possible wavelengths, but the laser used was run at 532 or 355 nm. These wavelengths have photon energies of 2.33 and 3.49 eV respectively. These energies are below the ionization potential of most molecules. Coronene, for example, has an ionization potential of 7.29 eV and most PAHs have ionization potentials near or above this number.[1] As such, even at 355 nm, two photons would not have enough energy to exceed the ionization potential and produce a cation. The absorption of several photons, even at 355 nm, would be required for the production of a cation through photoionization.

Although a multiphoton absorption process is possible, the laser striking the solid surface is near instantaneous and the simultaneous absorption of several photons is not likely. The more probable result is that the absorption produces a super-heated plume that may get hot enough to break bonds and cause fragmentation. The fragmentation process can produce dehydrogenated molecules or break other weak bonds depending on the molecule. Additionally, any impurities, such as abundant salts like NaCl, are often present from glassware or sweat. These salts have a much lower ionization energy and may easily ionize from either photoionization or from the intense heat. The plume of material may be dense enough for the salt ions and fragmented molecules to undergo collisions resulting in ion-molecule reactions between the two. Any electrons produced by the ion formation may also be accelerated by the electronic fields and

collide with neutrals in the desorption cloud resulting in an electron impact ionization mechanism.[2] Through these methods, it is probable that large molecules can be produced as neutrals within the cloud of desorbed material before undergoing ionization through electron impact to form the cations that can be detected by the electron multiplier tube.

The positively charged cloud of ions is pushed into the system by a pair of positively biased plates. The positively biased field produced between the repeller plate and draw-out-grid (DoG) pushes the ion cloud into the system. A third grounded plate produces a smaller positively biased field with the DoG to accelerate the ions into the flight tube. Within the flight tube, the ions are imparted with a certain amount of kinetic energy from the repulsive fields. Based on fundamental physics, the kinetic energy relates to the velocity of an ion by Equation (1).[3] As the ions travel down the collision-free flight tube, the different masses begin to separate due to having different velocities.[4] The ions are detected when they collide with an electron multiplier tube at the far end of the flight tube. By knowing the length of the flight tube and the amount of kinetic energy imparted on the ions by the electric fields, the mass can be calculated by rearranging Equation (1).

$$KE = \tfrac{1}{2}mv^2 \quad (1)^3$$

A figure of the mass spectrometer is presented in Figure 2.1. All samples were examined with both the 532 nm and 355 nm wavelengths and using a variety of laser irradiances, though generally most spectra were taken at the minimum power to see consistent monomer signal. Other mass spectrometer settings were also adjusted to optimize signal intensity and improve resolution to the greatest extent possible.

2.1 Thin Film Samples

The spectra of thin film PAH samples contain mostly only monomer mass peaks. Both pyrene and perylene contain a significant peak representing the monomer peaks at m/z 202 and 252 respectively. Other peaks were common contaminants that result from the handling of the samples. Sodium and potassium peaks commonly show up as a result of natural salts and oils present in human hands. Copper isotope peaks are a result of the laser desorption beam striking the copper mass spectrometer probe tip with enough power to desorb the metal. Stainless steel components, such as iron, chromium, and nickel can also be detected if the laser beam is positioned to hit the stainless steel repellar plate just off the mass spectrometer tip. These contaminant peaks are useful as calibration tests and are significantly lower in mass than the desired PAH monomers.

For comparison, coronene contains a number of significant peaks from abundant contaminants within the coronene sample. The predominant peak for coronene is at m/z = 300. Common contaminants include benzo(ghi)perylene (m/z 276), benzo(pqr)naphtho[8,1,2-bcd]perylene (m/z 350), naphtho[8,1,2(abc)]coronene (m/z 374), and ovalene (m/z 398).[3-11] Coronene thin film spectra also include the electrostatically-bound dimer of coronene at m/z = 600. The presence of the electrostatically-bound dimer has been reported previously within the literature.[8-9] Figure 2.2 contains the spectra of the thin film samples taken under similar spectrometer conditions with the wavelength used reported within the figure. Although only one wavelength is shown for each sample, similar spectra were observed at the other wavelength. No significant changes in the spectra occurred when spectrometer conditions or laser irradiance were altered.

2.2 Pressed Pellet Samples

The pressed pellet samples were examined using similar mass spectrometer settings as the thin film samples. For samples of pyrene, perylene, and coronene, the pressed pellet samples show a curious set of peaks just under the mass of the PAH electrostatically-bound dimer. Expansion of these peaks revealed that they were spaced one mass unit apart with larger peaks for the loss of even numbers of mass from the electrostatically-bound dimer. The primary peaks were found to be the 2M-4 and 2M-2 masses, where M is the monomer unit mass. Without any further studies, these masses were assumed to be the formation of covalently-bonded dimers through the loss of 1 or 2 hydrogen from each monomer, though this topic will be more thoroughly examined in later chapters. Figure 2.3 contains the pressed pellet mass spectra of all three PAHs showing the higher mass dimer and trimer peaks. These covalently-bonded dimers were measured at around 25-50% the intensity of the parent monomer for each of the samples studied. Similar series of peaks were detected at just under the mass of the electrostatically-bound trimer, but the intensities were often below 10% of the monomer peak. Such structures were noted, but not of significant enough intensity to be the focus of these studies. Figures 2.4, 2.5, and 2.6 show the direct comparison between pyrene, perylene, and coronene thin film and pressed pellet spectra respectively. Figure 2.7 zooms in on the dimer region to examine the ratio of the singly and doubly-bonded dimers for all three samples studied. With the evidence of these dimer structures, the next step in the process is to replicate these mass spectrometer conditions to try and collect PAH dimers that can be synthesized in large quantities through laser desorption.

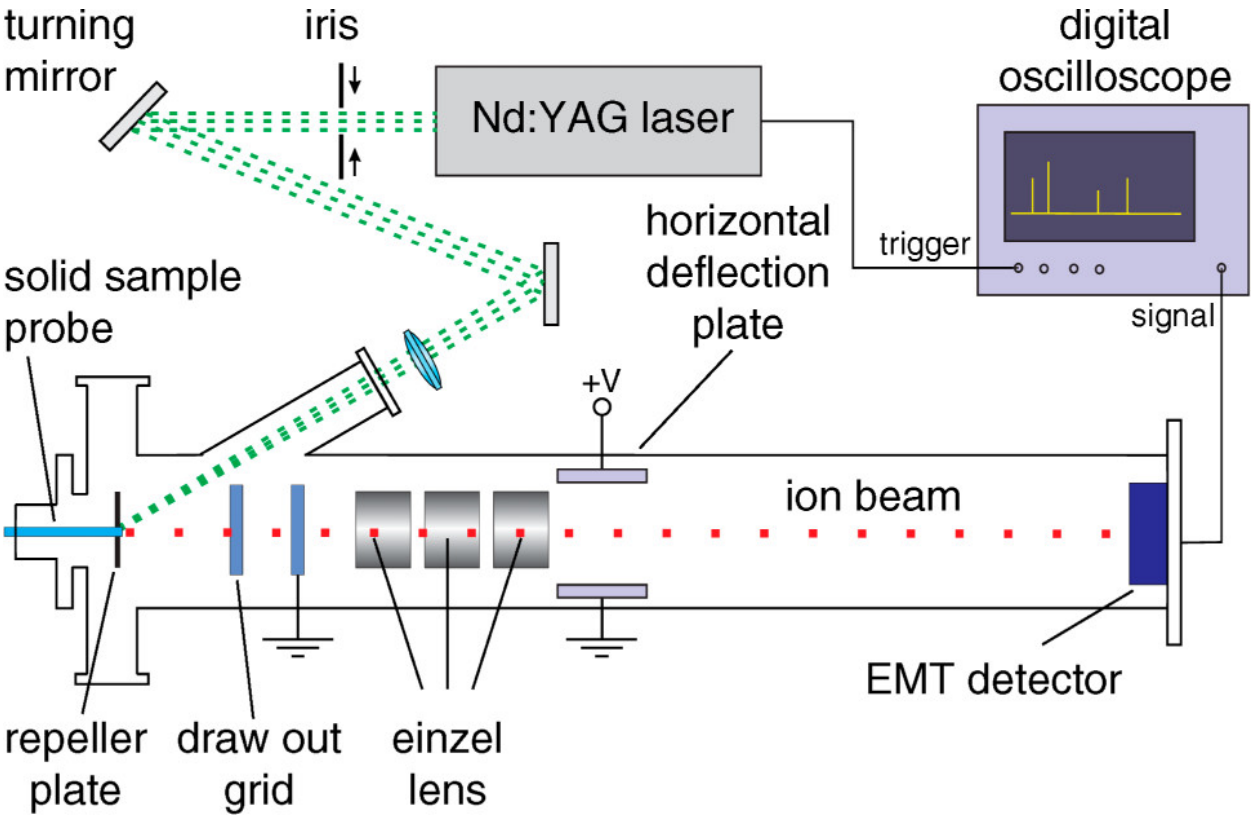

Figure 2.1. Example layout of a LD-ToF-MS.[1]

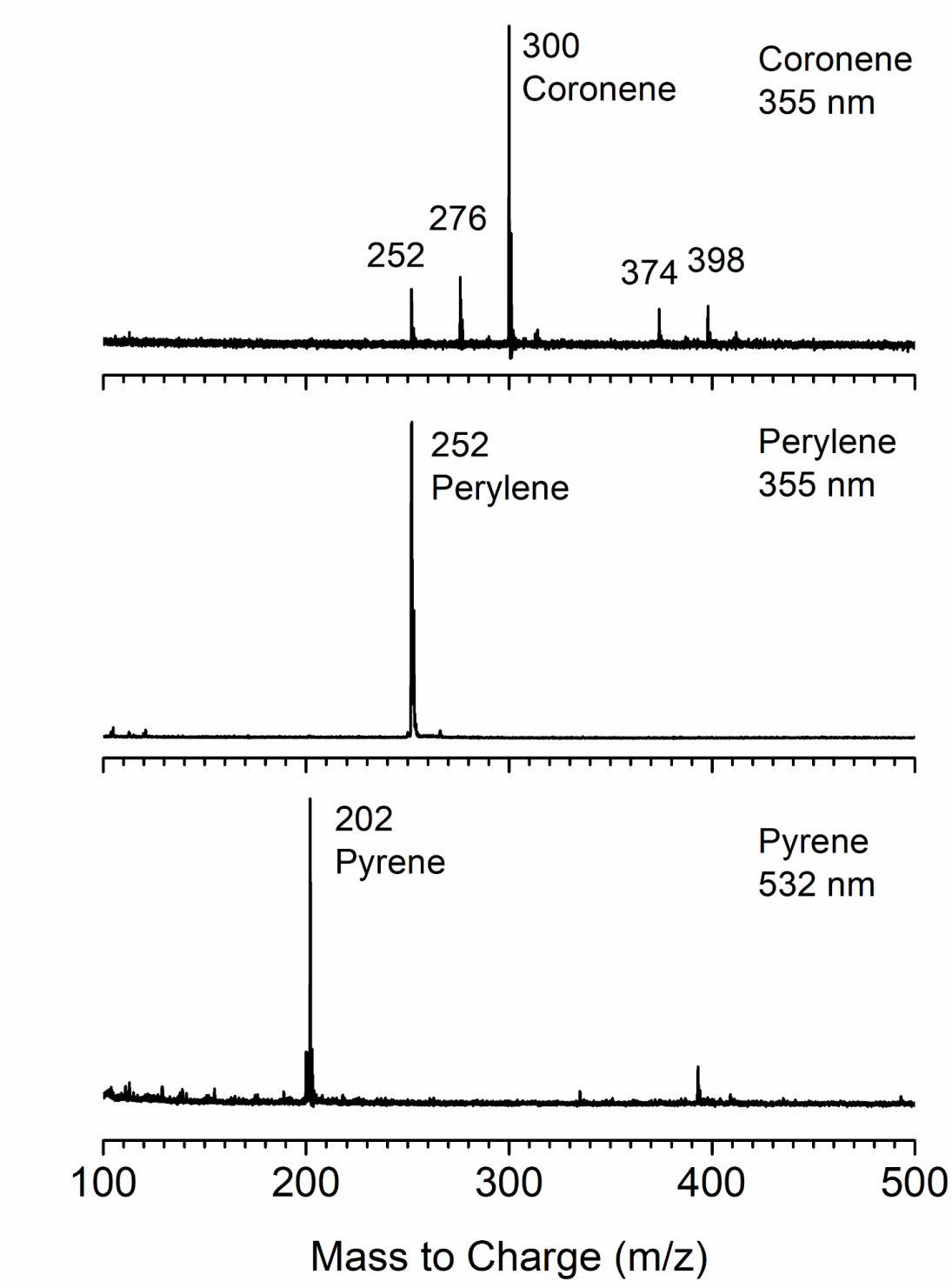

Figure 2.2. Thin film mass spectra of pyrene, perylene, and coronene with significant peaks labeled.

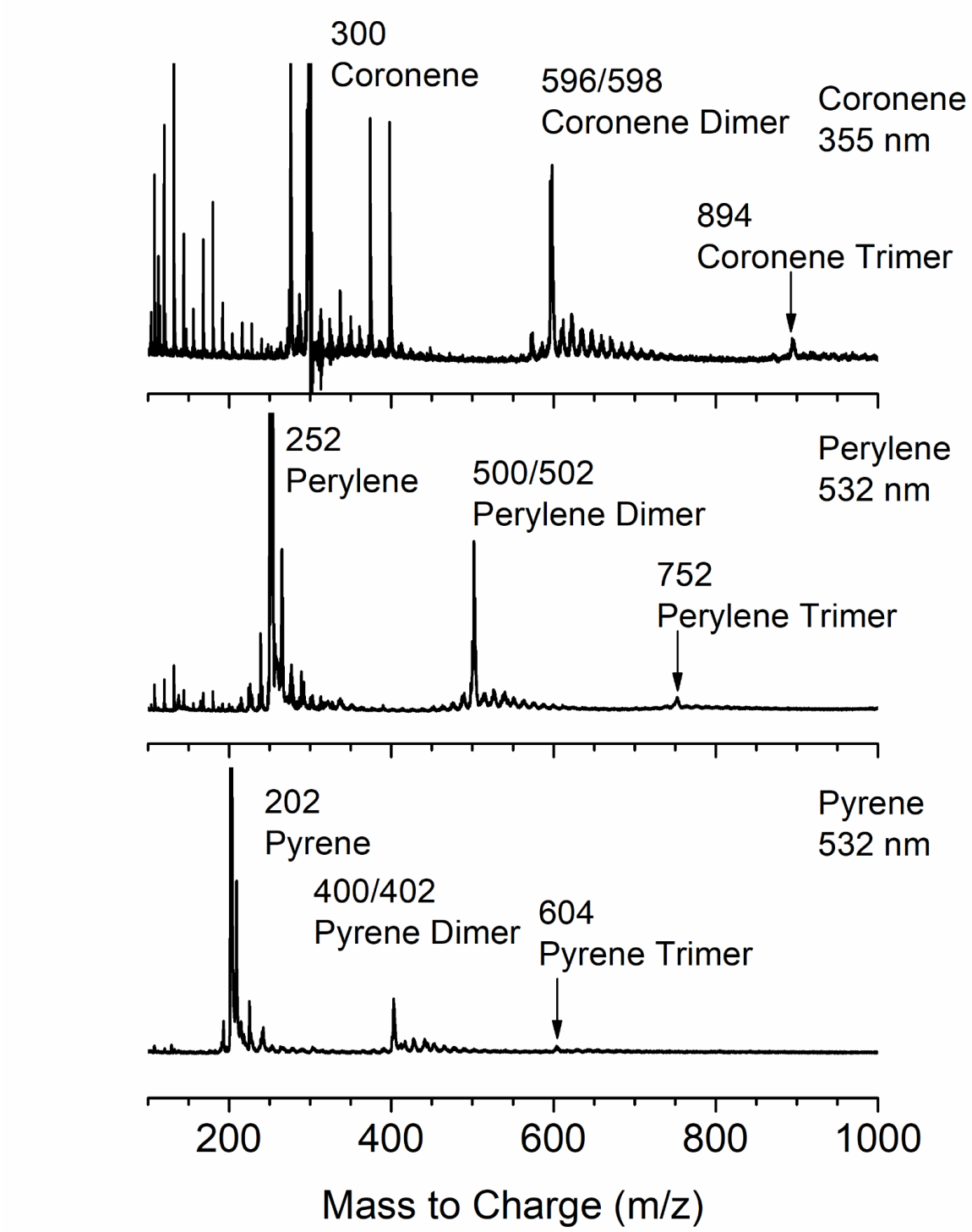

Figure 2.3. Pressed pellet mass spectra of pyrene, perylene, and coronene with indicated dimer and trimer peaks. Monomer peaks are scaled to 25% intensity to show the dimer and trimer peaks more clearly.

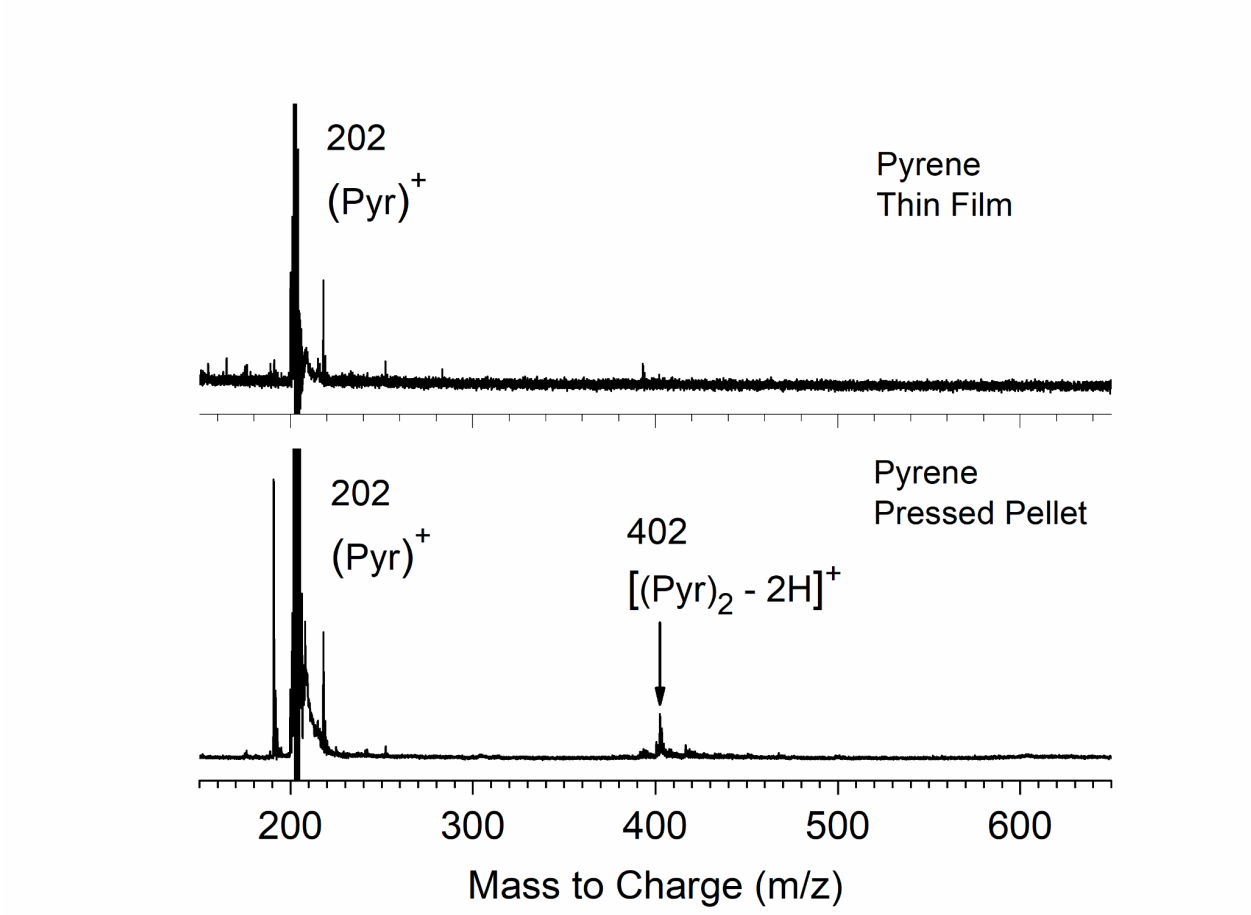

Figure 2.4. Comparison of pyrene thin film and pressed pellet mass spectra taken at 355 nm. Monomer peaks are scaled to 30% intensity to show the dimer peaks more clearly.

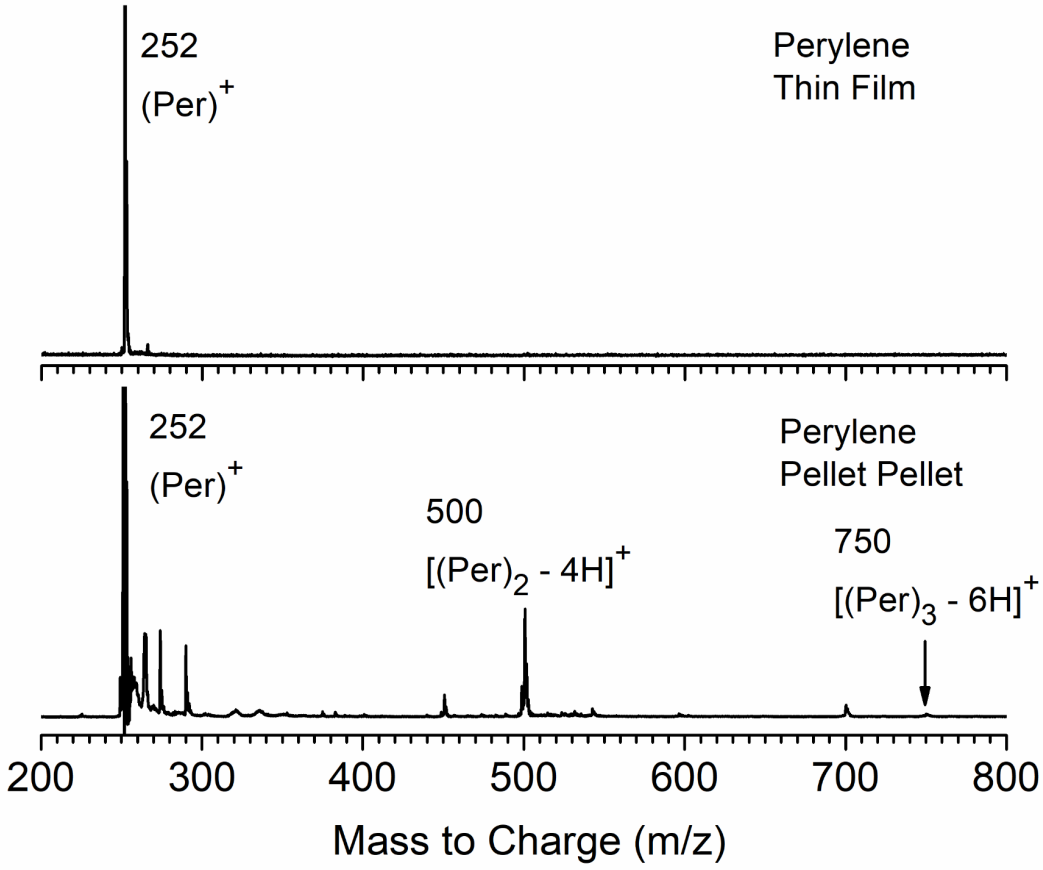

Figure 2.5. Comparison of perylene thin film and pressed pellet mass spectra taken at 355 nm. Monomer peaks are scaled to 70% intensity to show the dimer and trimer peaks more clearly.

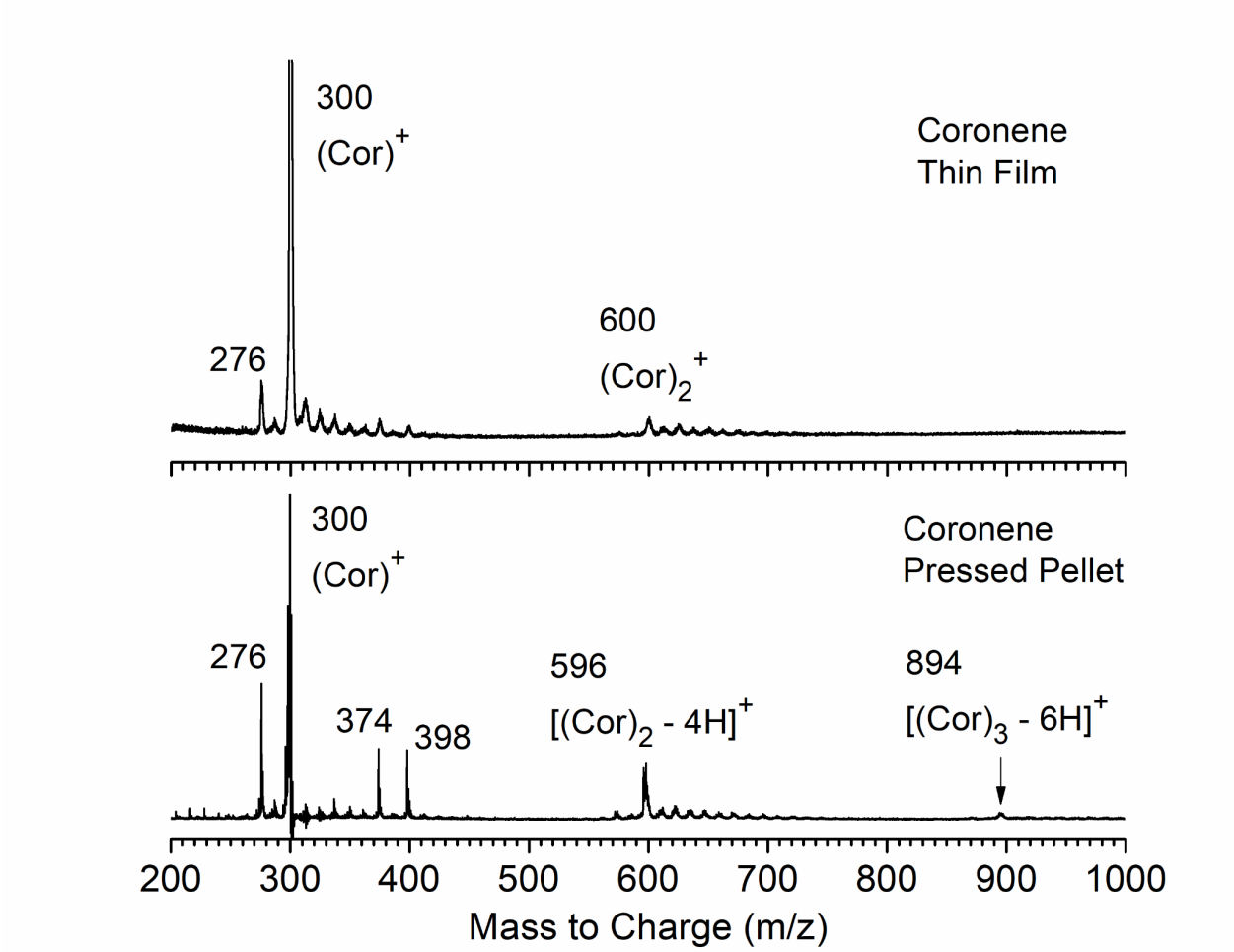

Figure 2.6. Comparison of coronene thin film and pressed pellet mass spectra taken at 532 nm. Monomer peaks are scaled to 75% intensity to show the dimer and trimer peaks more clearly.

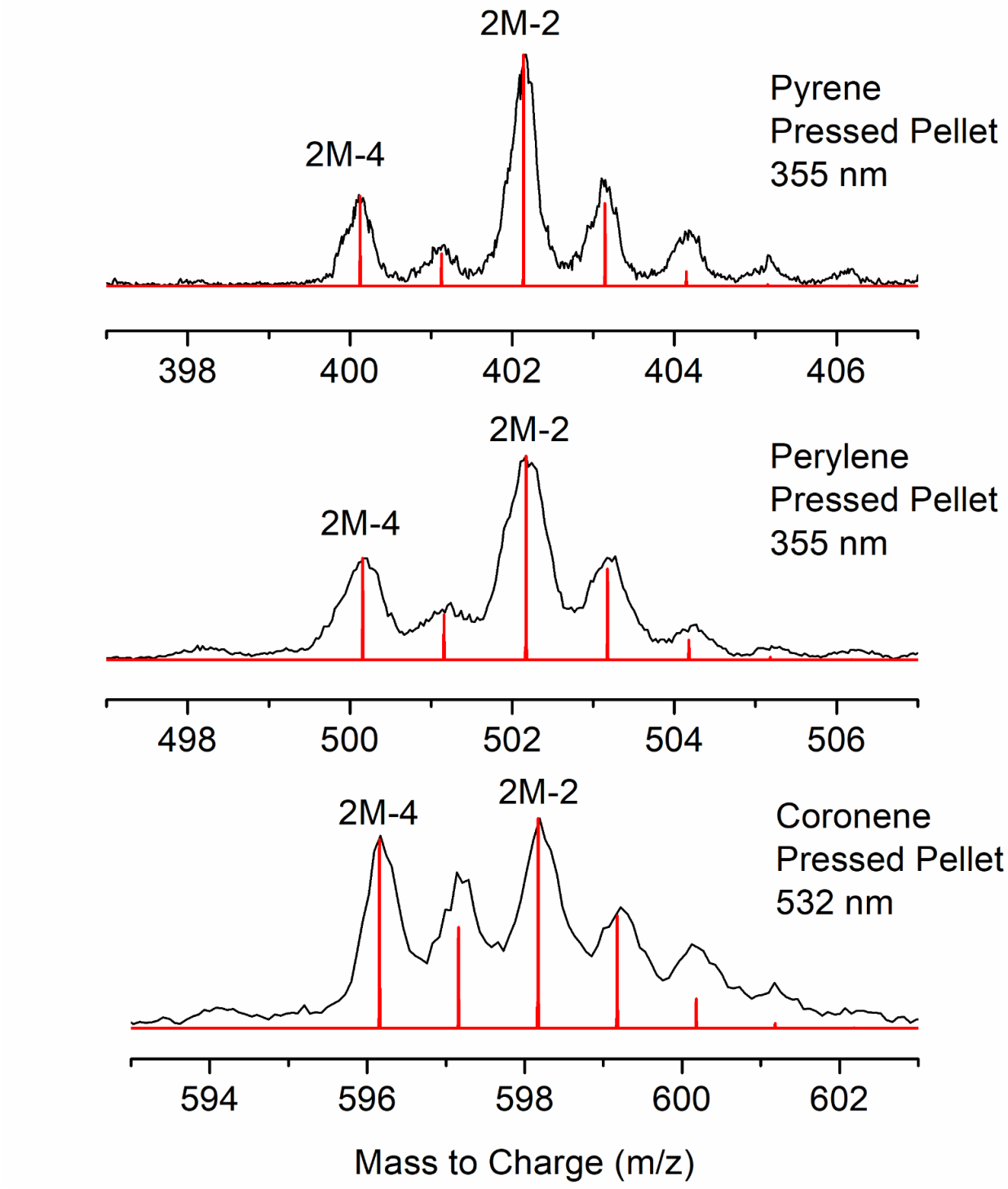

Figure 2.7. Expanded view of the various pellet dimer regions with simulated 2M-4:2M-2 isotope ratios of 2:5, 1:2, and 9:10 for pyrene, perylene, and coronene respectively.

References

1. Lias, S.G. *Ionization Energy Evaluation* in **NIST Chemistry WebBook, NIST Standard Reference Database Number 69**, Eds. P.J. Linstrom and W.G. Mallard, National Institute of Standards and Technology, Gaithersburg MD, 20899.
2. Cheng, T. C.; Akin, S. T.; Dibble, C. J.; Ard, S.; Duncan M. A. Tunable Infrared Laser Desorption and Ionization of Fullerene Films. *Int. J. Mass Spec.* **2013**, *354-355*, 159-164.
3. R. N. Compton, M. A. Duncan, *Laser Experiments for Chemistry and Physics*, Oxford University Press, 2016.
4. Ayers, T. M.; Akin, S. T.; Dibble, C. J.; Duncan, M. A. Laser Desorption Time-of-Flight Mass Spectrometry of Inorganic Nanoclusters: An Experiment for Physical Chemistry or Advanced Instrumentation Laboratories. *J. Chem. Educ.* **2014**, *91*, 291-296.
5. Yoshimura, K.; Przybilla, L.; Ito, S.; Brand, J. D.; Wehmeir, M.; Räder, H. J.; Müllen, K. Characterization of Large Synthetic Polycyclic Aromatic Hydrocarbons by MALDI- and LD-TOF Mass Spectrometry. *Macromol. Chem. Phys.* **2001**, *202*, 215-222.
6. Bréchignac, Ph.; Schmidt, M.; Masson, A.; Pino, T.; Parneix, P.; Bréchignac, C. Photoinduced Products from Cold Coronene Clusters. *Astron. Astrophys.* **2005**, *442*, 239-247.
7. Martínez-Haya, B.; Hortal, A. R.; Hurtado, P.; Lobato, M. D.; Pedrosa, J. M. Laser Desorption/Ionization Determination of Molecular Weight Distributions of Polyaromatic Carbonaceous Compounds and their Aggregates. *J. Mass Spectrom.* **2007**, *42*, 701-713.
8. Cristadora, A.; Räder, H. J.; Müllen, K. Clustering of Polycyclic Aromatic Hydrocarbons in Matrix-Assisted Laser Desorption/Ionization and Laser Desorption Mass

Spectrometry. *Rapid Commun. Mass Spectrom.* **2007**, *21*, 2621-2628.

9. Bréchignac, P.; Garcia, G. A.; Falvo, C.; Joblin, C.; Kokkin, D.; Bonnamy, A.; Parneix, P.; Pino, T.; Pirali, O.; Mulas, G.; et al. Photoionization of Cold Gas Phase Coronene and Its Clusters: Autoionization Resonances in Monomer, Dimer, and Trimer and Electronic Structure of Monomer Cation. *J. Chem. Phys.* **2014**, *141*, 164325.
10. Gámez, F.; Hortal, A. R.; Martínez-Haya, B.; Soltwisch, J.; Dreisewerd, K. Ultraviolet Laser Desorption/Ionization Mass Spectrometry of Single-Core and Multi-Core Polyaromatic Hydrocarbons under Variable Conditions of Collisional Cooling: Insights into the Generation of Molecular Ions, Fragments and Oligomers. *J. Mass Spectrom.* **2014**, *49*, 1127-1138.
11. Joblin, C.; Dontot, L.; Garcia, G. A.; Spiegelman, F.; Rapacioli, M.; Nahon, L.; Parneix, P.; Pino, T.; Bréchignac, P. Size Effect in the Ionization Energy of PAH Clusters. *J. Phys. Chem. Lett.* **2017**, *8*, 3697-3702.

Chapter 3

Photochemical Synthesis & Purification

After the discovery of the oligomerized PAH samples in the mass spectrometer, the next project became attempting the synthesis of these dimer samples in large quantities by replicating the mass spectrometer conditions. Pressed pellet samples were produced as previously described with the same commercially available materials. These samples were mounted with double-sided tape on the tip of an angled metal rod centered in a KF50 6-way cross. A quartz slide was taped in place opposite the mounted pellet. A diagram of the synthesis apparatus is presented in Figure 3.1. The system was attached to a rough vacuum to reach the mtorr pressure range. The system was aligned in front of a Coherent LPX Pro excimer laser, operated at 248 nm (KrF) wavelength. The laser was partially focused through a cylindrical lens to a 0.5 cm^2 rhombus-shaped spot enveloping the pressed pellet. Laser power was adjusted to 20 mJ/pulse to replicate the 40 mJ/cm^2/pulse power from the mass spectrometer experiments. The laser was operated at its 400 Hz repetition rate maximum for approximately 2 hours until the pellet was completely desorbed.

After desorption, the produced material was collected from the quartz slide by scraping with a razor blade. The interior of the 6-way cross was also scraped and cleaned to acquire more material. A sample collection run with a 100 mg pellet of material would yield 70-80 mg of collected material. Collected material had a notably visible difference in color from the commercial material with a darker tint. By adding a mass spectrometer tip near the quartz slide during the collection process, a film of material can be deposited directly onto the tip for examination. Mass spectra of collected films contain the same mass peaks as the pressed pellet

samples. For comparison, collected powdered samples were similarly suspended in methanol and deposited to produce the same type of thin film samples as discussed in the previous chapter. The suspension of the material does not produce any change in the mass spectra. Example spectra of the collected material are presented in Figure 3.2 with no notable difference from the previously seen pressed pellet samples.

Purification of the collected samples was achieved by a differential sublimation method. 10 mg scoops of collected powder samples were placed inside a tungsten boat and mounted within a bell jar vacuum system apparatus. The boat was resistively heated under mtorr vacuum conditions. A variety of temperatures and timeframes were tested to achieve purification of the collected sample. Both pyrene and perylene samples were purified at a temperature near 100°C with lower temperatures yielding little to no change and higher temperatures resulting in no recovered material. Testing found that longer heating times, up to 24 hours, resulted in greater reduction of the monomer peak within the mass spectrometer. Coronene samples required higher temperature runs at at least 150°C with no change in samples at lower temperature. Samples of coronene are seemingly less stable and higher temperatures or heating times exceeding 3 hours would result in no recovered material.

Purified samples could be collected with a yield of approximately 10-20% mass. Residual purified samples often contained possible soot contaminates which causes a darker, often near black coloration for materials. Purified samples were reexamined under the same mass spectrometer conditions and found to have little to no remaining monomer peak without significant decrease in the dimer peak intensity. Figures 3.3-3.5 show the comparison of the pyrene, perylene, and coronene collected material before and after purification at similar mass spectrometer conditions. Figure 3.6 contains the zoom-ins of the dimer region peaks to check for

any notable change in the relative intensities in dimers after purification. Further testing of the purified samples was performed using a variety of other experimental methods as discussed later.

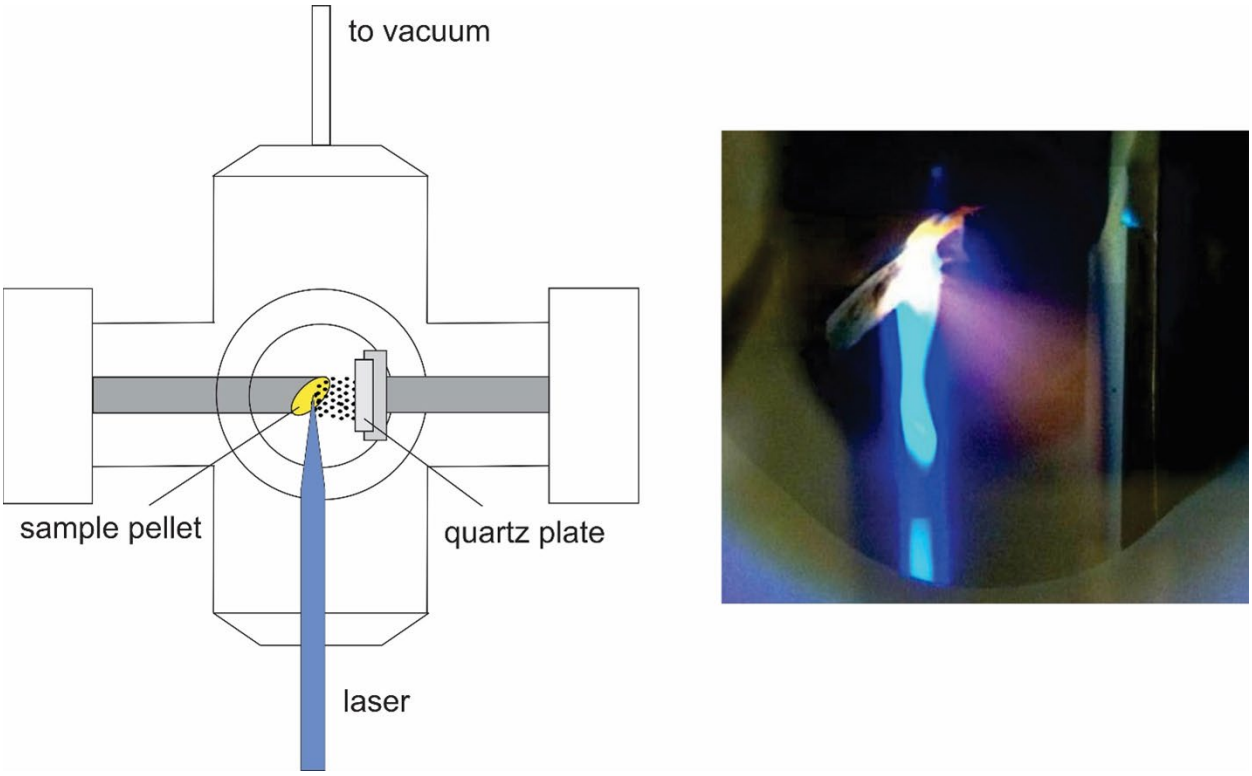

Figure 3.1. Diagram of the PAH synthesis apparatus (left) and photograph of the material collection process (right). The stream of vapor is glowing because of the known phosphorescence of coronene.

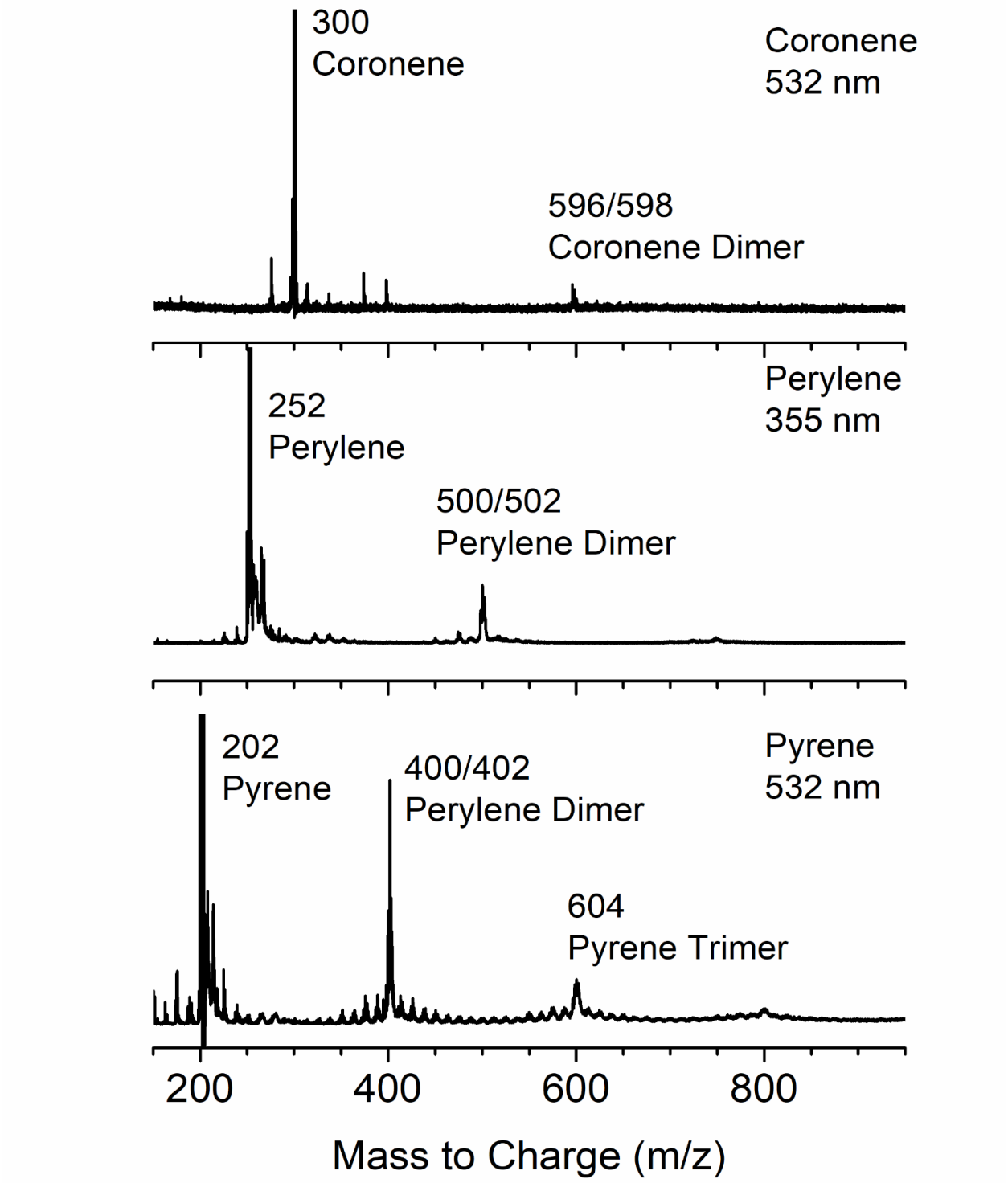

Figure 3.2. Collected mass spectra films of pyrene, perylene, and coronene with indicated dimer peaks. Monomer peaks are scaled to 25% intensity to show the dimer and trimer peaks more clearly.

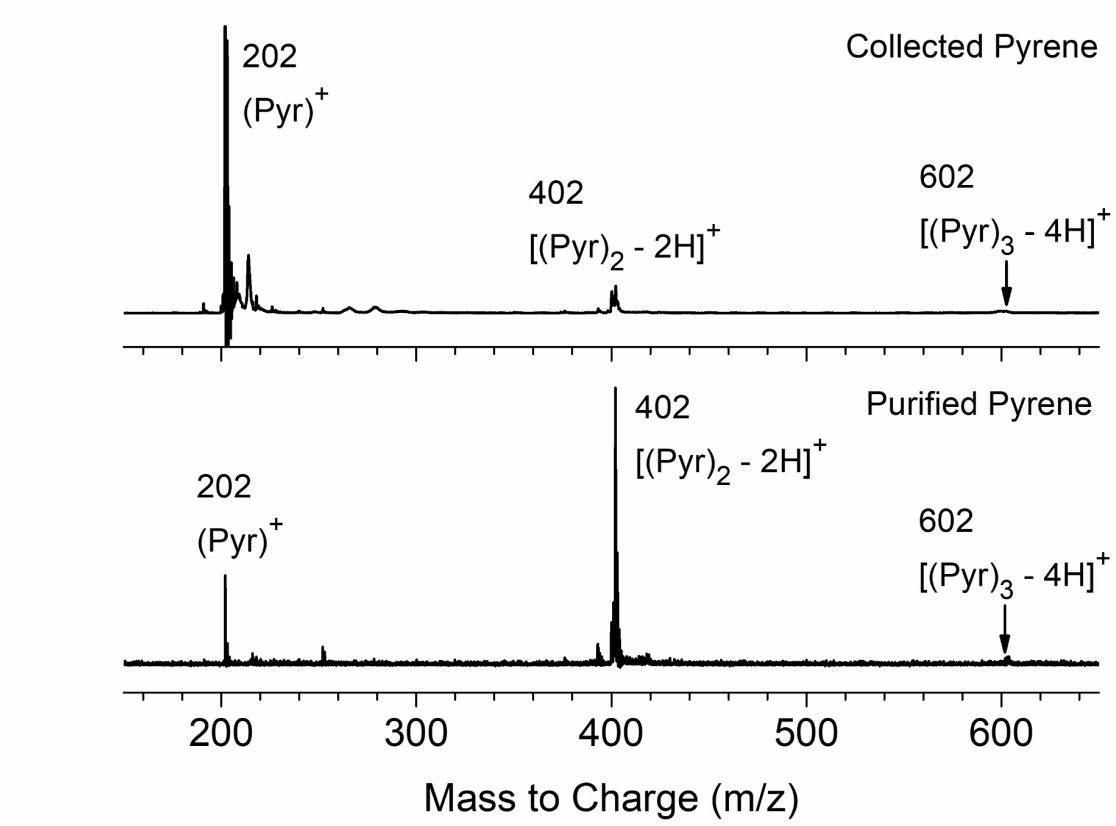

Figure 3.3. Collected vs purified mass spectra of pyrene under similar mass spectrometer conditions with a 355 nm laser desorption source.

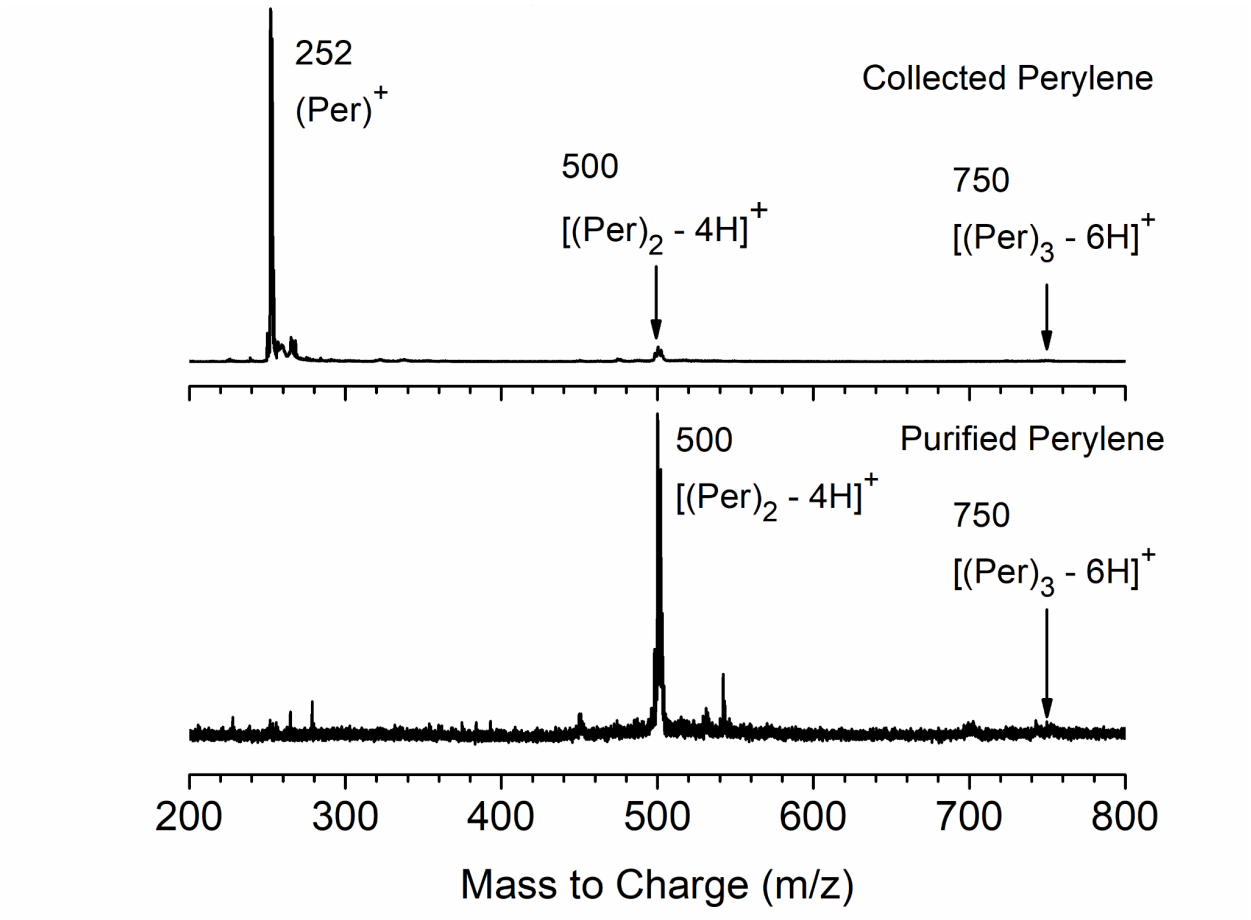

Figure 3.4. Collected vs purified mass spectra of perylene under similar mass spectrometer conditions with a 355 nm laser desorption source.

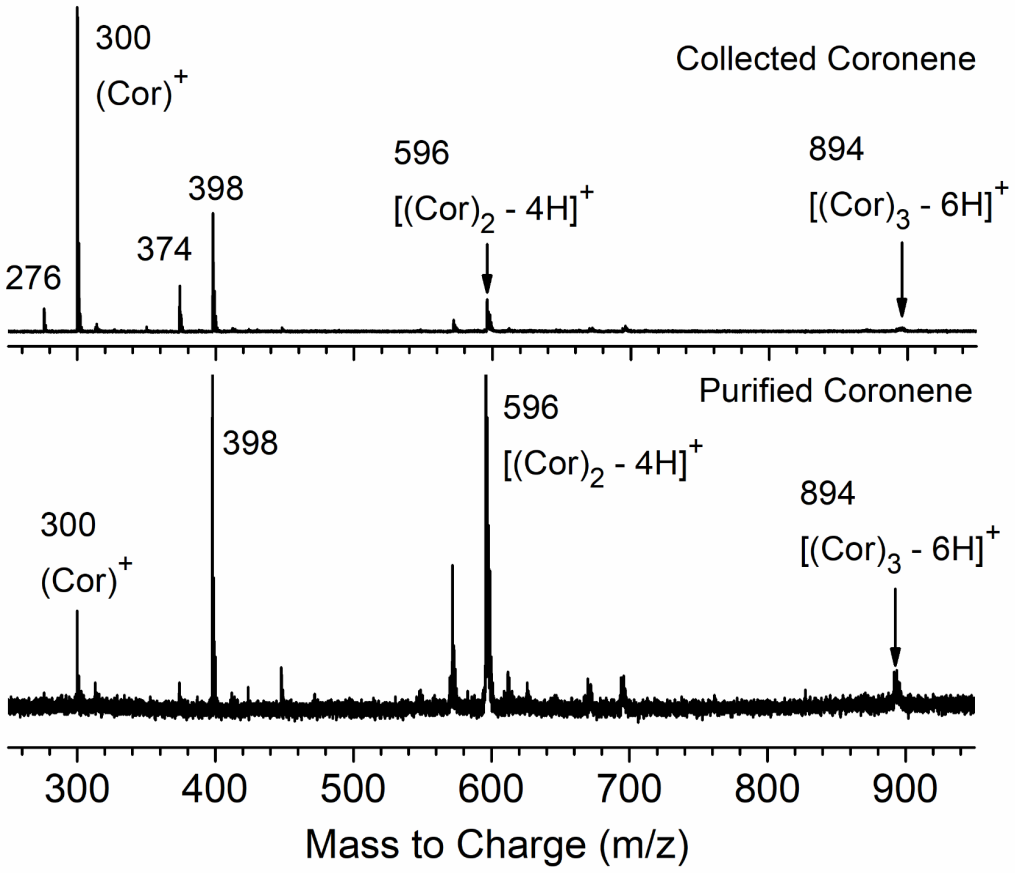

Figure 3.5. Collected vs purified mass spectra of coronene under similar mass spectrometer conditions with a 355 nm laser desorption source.

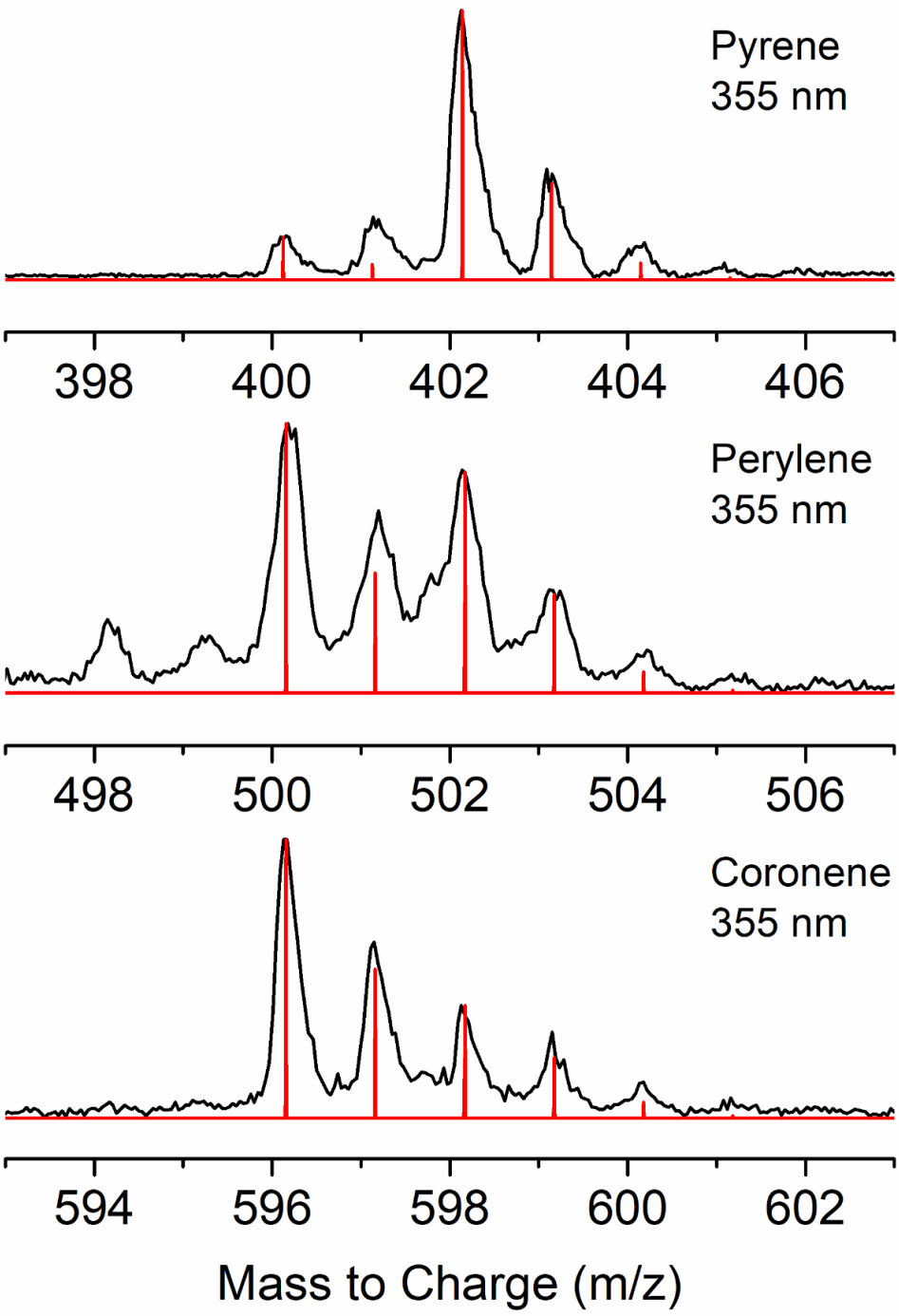

Figure 3.6. Expanded view of the various purified sample dimer regions with simulated 2M-4:2M-2 isotope ratios of 1:5, 5:4, and 5:2 for pyrene, perylene, and coronene respectively.

Chapter 4

Theoretical Computations

In order to fully understand the dimerization process, the possible structures need to be identified. To accomplish this goal, various possible covalently bonded dimers were simulated using the Gaussian 09 program package.[1] Molecules of this size are challenging to compute and to reduce computational costs a density functional theory (DFT) method was preferred over more computationally expensive *ab initio* methods. After some literature searching, the Cambridge B3LYP (CAM-B3LYP) method was chosen, a method specifically designed for carbon based systems.[2] This method offers a convenient compromise between accuracy and computational time for working with larger hydrocarbon based molecules.

A selection of basis sets were tested, with a focus on the def2SVP to def2TZVP levels. Calculations of the dimerized structures were too complex for the def2TZVP basis set and computations failed to converge even at longer runtimes or larger memory allowances. Quick calculations using the def2SVP basis set were used to get a general idea of possible dimer structures, but were deemed not rigorous enough for finalized structure calculations. Ultimately the def2SVPP basis set was used to compute probable structures and the def2TZV basis was used to further optimize these structures. After optimization, both infrared and Raman frequencies were calculated at the same theory level to simulate the vibrational spectra. Vibrational frequencies were also checked for imaginary numbers which would indicate the structural calculation had been hindered by a saddle point. Frequencies were also used to correct for the zero-point energy for comparing the different possible dimer structures examined. A

variety of possible structures were examined for both the singly-bonded and doubly-bonded dimers. Figures 4.1-4.3 depict the examined dimer structures for pyrene, perylene, and coronene respectively with relative energies given. The most stable structures determined are presented in Figure 4.4 with relative energy difference between the doubly-bonded and singly-bonded structures.

Time-dependent density functional theory (TD-DFT) computations were also performed with the optimized structures to determine the electronically excited states. From these excited states, the vertical electronic transitions were calculated with no vibronic structure. The electronic transitions correspond to the UV-Visible absorption spectra of a molecule.

The computed frequencies were used to simulate the infrared absorption bands and compared to the commercial monomer spectra available through NIST.[3] From these comparisons, a scaling factor of 0.956 was determined. The same scaling factor was used for the Raman scattering frequencies and these scaling factors were also applied to the computed dimer structures. A similar comparison was performed for the electronic transitions and used to determine a scaling factor of 1.13 to the wavelength when compared with the monomer. These scaling factors were uniformly applied to all theoretical spectra unless otherwise specified.

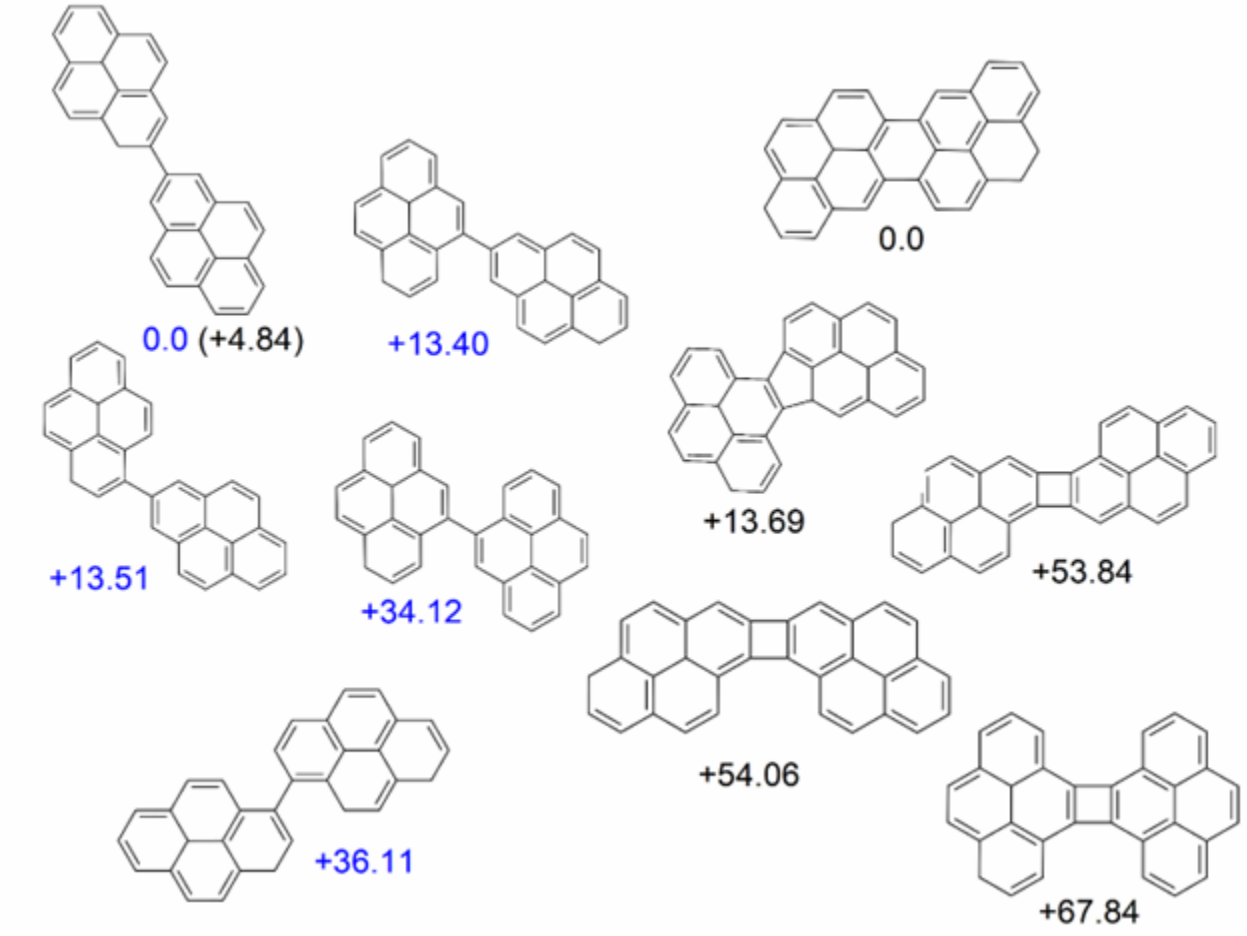

Figure 4.1. Calculated pyrene dimer structures with zero-point corrected relative energies (kcal/mol). The numbers in blue are relative to the most stable singly-bonded dimer, whereas those in black are relative to the most stable doubly-bonded dimer (+H_2).

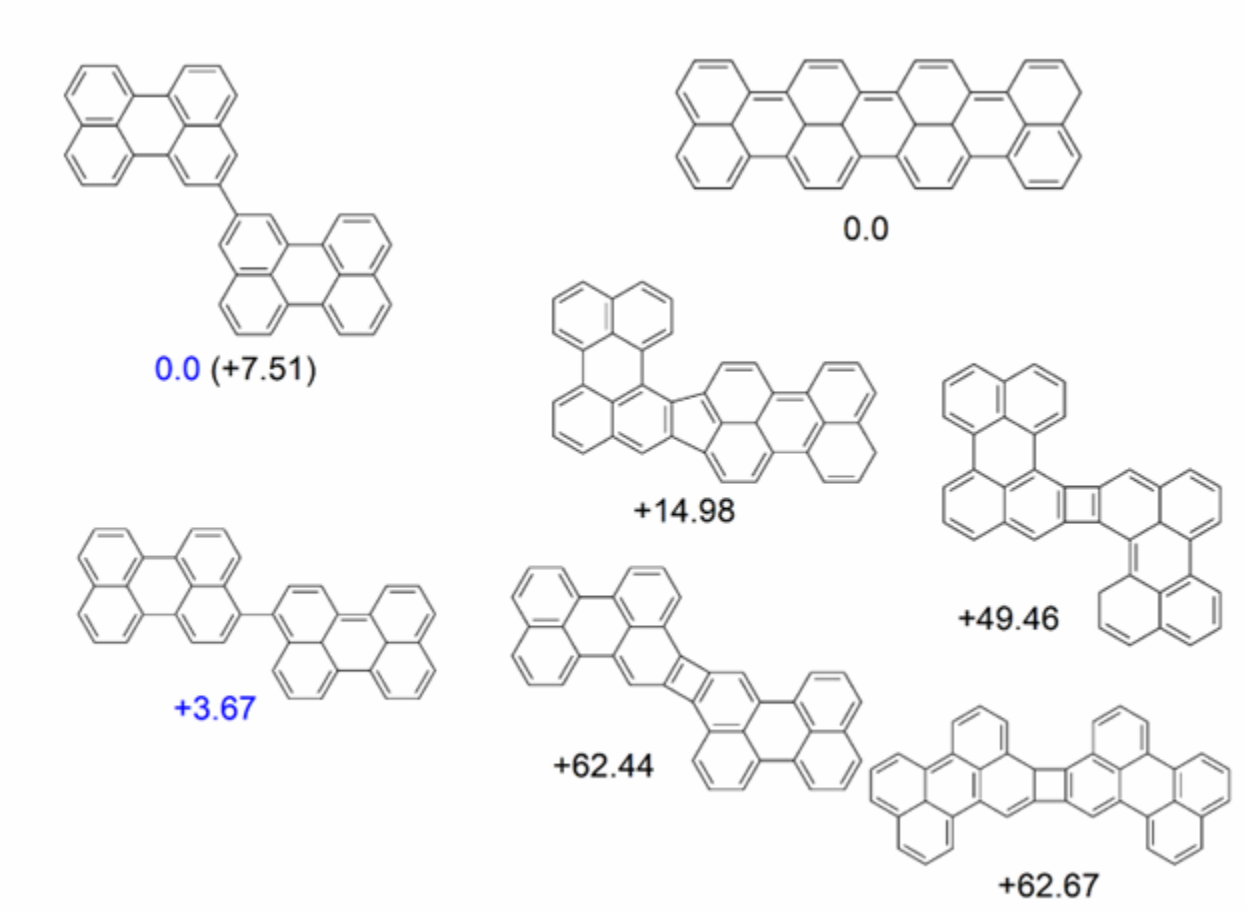

Figure 4.2. Calculated perylene dimer structures and zero-point corrected relative energies (kcal/mol). The numbers in blue are relative to the most stable singly-bonded dimer, whereas those in black are relative to the most stable doubly-bonded dimer (+H_2).

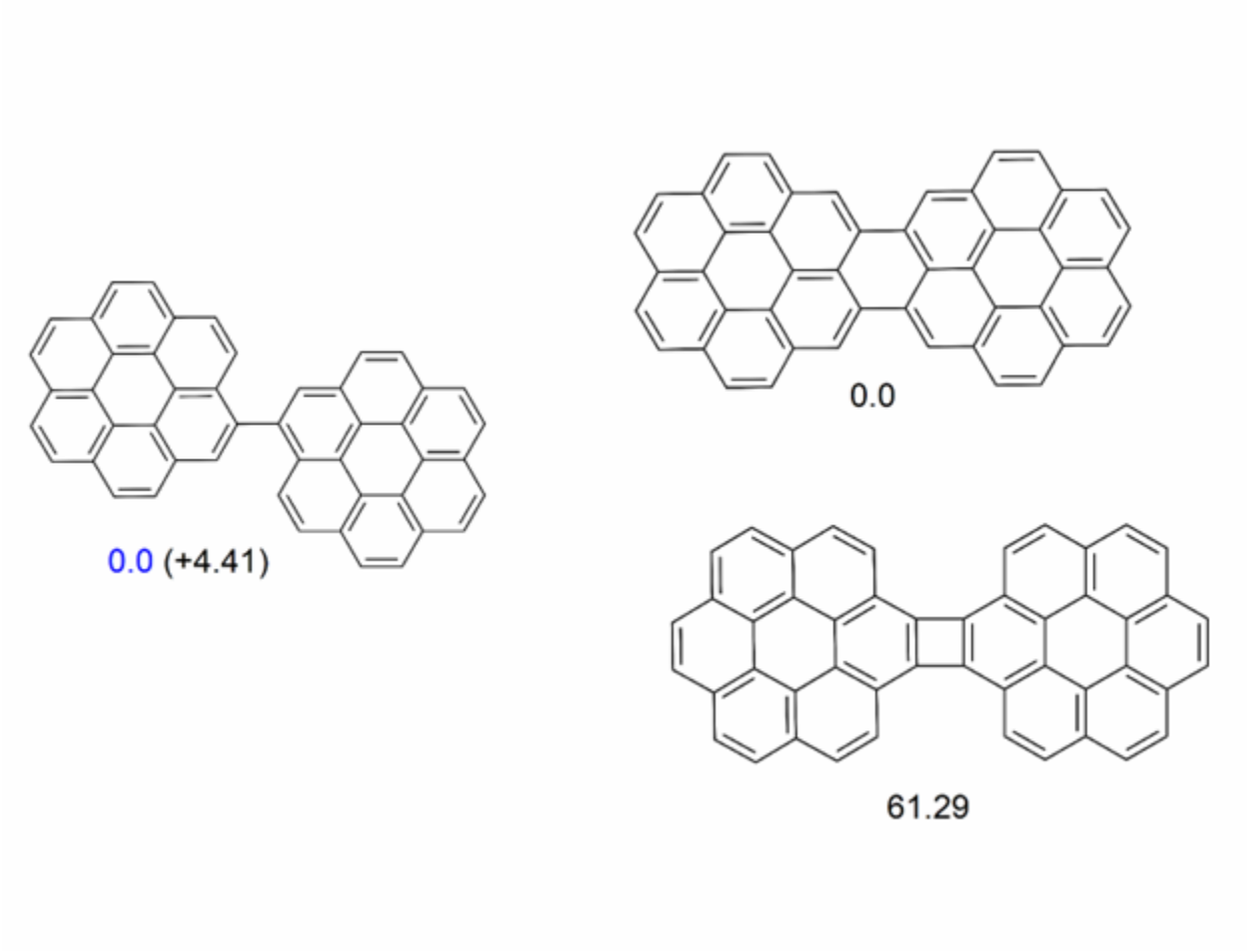

Figure 4.3. Calculated coronene dimer structures and zero-point corrected relative energies (kcal/mol). The numbers in blue are relative to the most stable singly-bonded dimer, whereas those in black are relative to the most stable doubly-bonded dimer (+H_2).

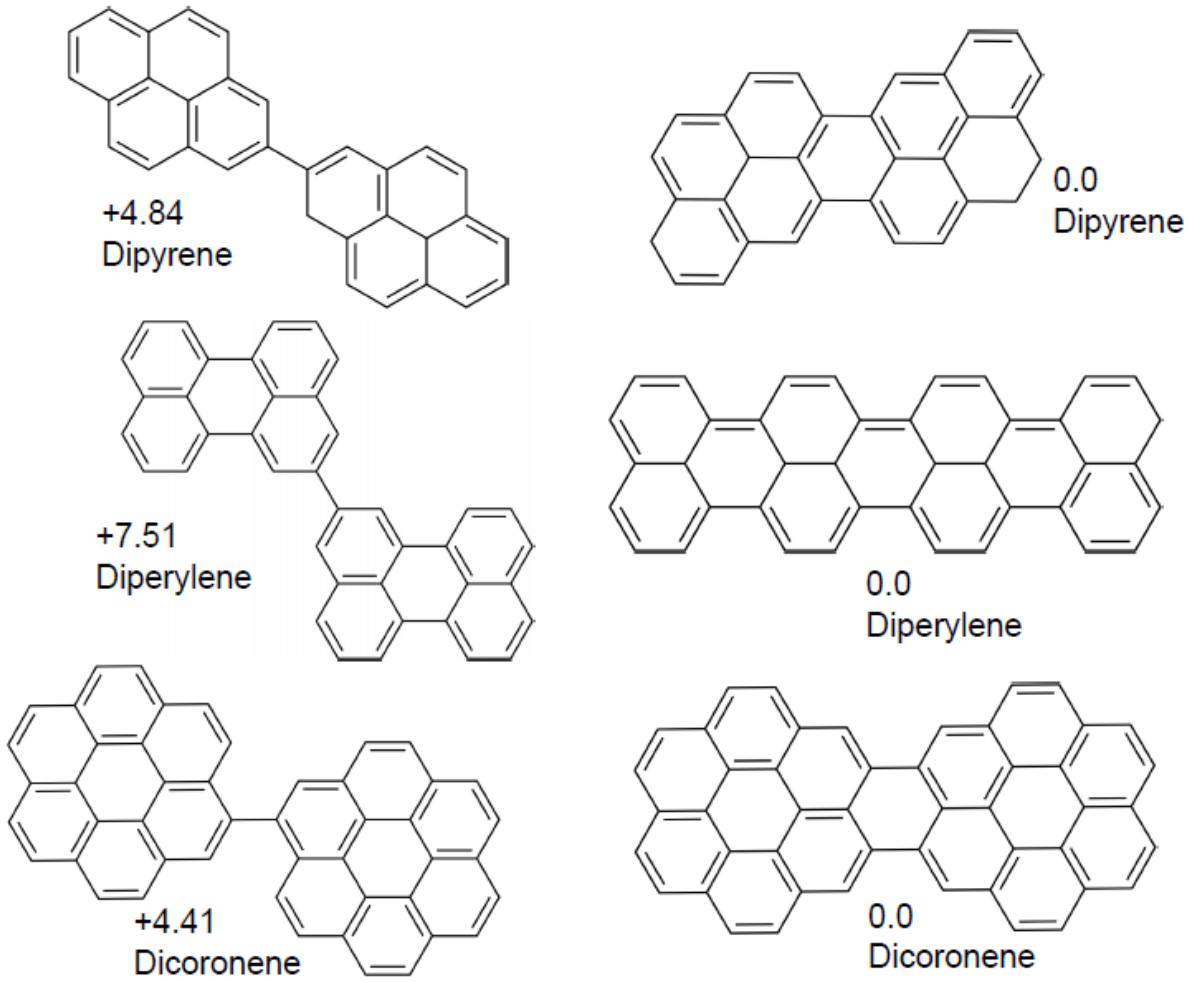

Figure 4.4. Lowest energy structures identified by computational studies for the 2M-2 and 2M-4 dimers of pyrene, perylene, and coronene. The relative energies (kcal/mol) for each of the 2M-2 species include the formation of one H_2 molecule, whereas those for the 2M-4 species include the formation of two H_2 molecules.

References

1. Frisch, M. J.; Trucks, G. W.; Schlegel, H. B.; Scuseria, G. E.; Robb, M. A.; Cheeseman, J. R.; Scalmani, G.; Barone, V.; Mennucci, B.; Petersson, G. A.; et al. Gaussian 09, Revision D.01; Gaussian, Inc.:Wallingford CT, 2009.
2. Bohl, E.; Mignolet, B.; Johansson, J. O.; Remacle, F.; Campbell, E. E. B. Low-lying, Rydberg States of Polycyclic Aromatic Hydrocarbons (PAHs) and Cyclic Alkanes. *Phys. Chem. Chem. Phys.* **2017**, *19*, 24090–24099.
3. NIST Mass Spectrometry Data Center, William E. Wallace, director, "Infrared Spectra" in **NIST Chemistry WebBook, NIST Standard Reference Database Number 69**, Eds. P.J. Linstrom and W.G. Mallard, National Institute of Standards and Technology, Gaithersburg MD, 20899, https://doi.org/10.18434/T4D303.

Chapter 5

Infrared Spectroscopy

The infrared spectroscopy of PAHs is important for determining if these molecules are truly responsible for the unassigned infrared emission bands (UIRs) in the interstellar medium. This series of infrared emission bands ranges from 3.3 (3030.3 cm^{-1}) to 12.7 μm (787.4 cm^{-1}) and has been attributed to a pattern common to PAHs. Despite a frequent consensus that these spectral bands are likely caused by interstellar PAHs, the exact species responsible have not been identified.[1-14] Examination of new PAH species may provide possible candidates that could explain these interstellar bands, and even new spectra that do not explain the UIRs may serve as benchmark data for theoretical computations that may be able to predict the possible species.

The infrared spectra of PAHs were taken on a Shimadzu IRAffinity-1S FT-IR operating in reflectance mode off powder samples. Before each scan, a background of air was taken. Scans were averaged over 32 sweeps across the range of 400 to 4000 cm^{-1} with a 1 cm^{-1} resolution. For each of the collected samples, the dried and purified powder was tested using the infrared reflectance off of the powder sample. For comparison, spectra under the same conditions were taken with the commercially available monomer material.

The infrared spectra of all three PAH dimer systems are similar to those of their corresponding monomers. The C-H stretches at high frequency have a low intensity. More region prominent bands are present in the carbon ring distortion region near 1500 cm^{-1} and in the C-H bending vibrations from 700 - 900 cm^{-1}. The pyrene spectrum does have distinct new spectral signatures as depicted in Figure 5.1. A new multiplet in the C-H stretching region, a new ring

vibration region near 1718.1 cm^{-1}, and a new feature in the C-H bending region at 875.4 cm^{-1} all show up in the dimer spectrum. Theory does not properly predict the multiplet structure within the C-H stretching region with either dimer structure. It is possible that this series of bands may be caused by Fermi resonances between the C-H stretches and overtones of the bands near 1500 cm^{-1}. Harmonic theory would not be able to account for Fermi resonances, but anharmonic theory may be a challenge with the size of the molecules being studied. The 2M-4 dimer has closer agreement to the multiplet in the bending region of the spectrum than the 2M-2 dimer for pyrene. Although the 1500-1700 cm^{-1} region has a number of changes compared to the monomer, theory does not seem to match very well in this region. Theory is far from definitive, and the simulated peaks in the monomer spectrum seem to often be at higher frequency than the actual monomer spectrum. Figure 5.1 focuses only on the most stable structures, but Figures 5.2 and 5.3 show the comparison of the various dimer structures for the singly-bonded and doubly-bonded structures respectively to check for better agreement. Due to the high symmetry of the various structures, the spectra show relatively little change in predicted peaks.

For perylene and coronene, the monomer and dimer spectra are virtually identical as shown in Figures 5.4 and 5.5 respectively. Dimers with nearly equivalent structures would likely have very similar spectra. The comparison between theory and experiment in the infrared region is not ideal, as even the monomer peaks do not perfectly align. Unfortunately, the theory calculations here are harmonic and anharmonicity is only corrected for using a singular scaling factor across the entire spectrum. This method of accounting for the anharmonicity is not likely to account for the anharmonic effects especially across several regions of the infrared. More thorough investigations of the infrared anharmonicity of PAHs would be an important study to pursue. Just to thoroughly check the possible structures for perylene and coronene, all possible

predicted dimers were compared to the purified PAH samples produced. Figures 5.6 and 5.7 show the comparison for the perylene singly-bonded and doubly-bonded dimer respectively. Figure 5.8 depicts the same for the coronene doubly-bonded dimer. All coronene singly-bonded dimers converged to the same structure and no comparison between them could be made.

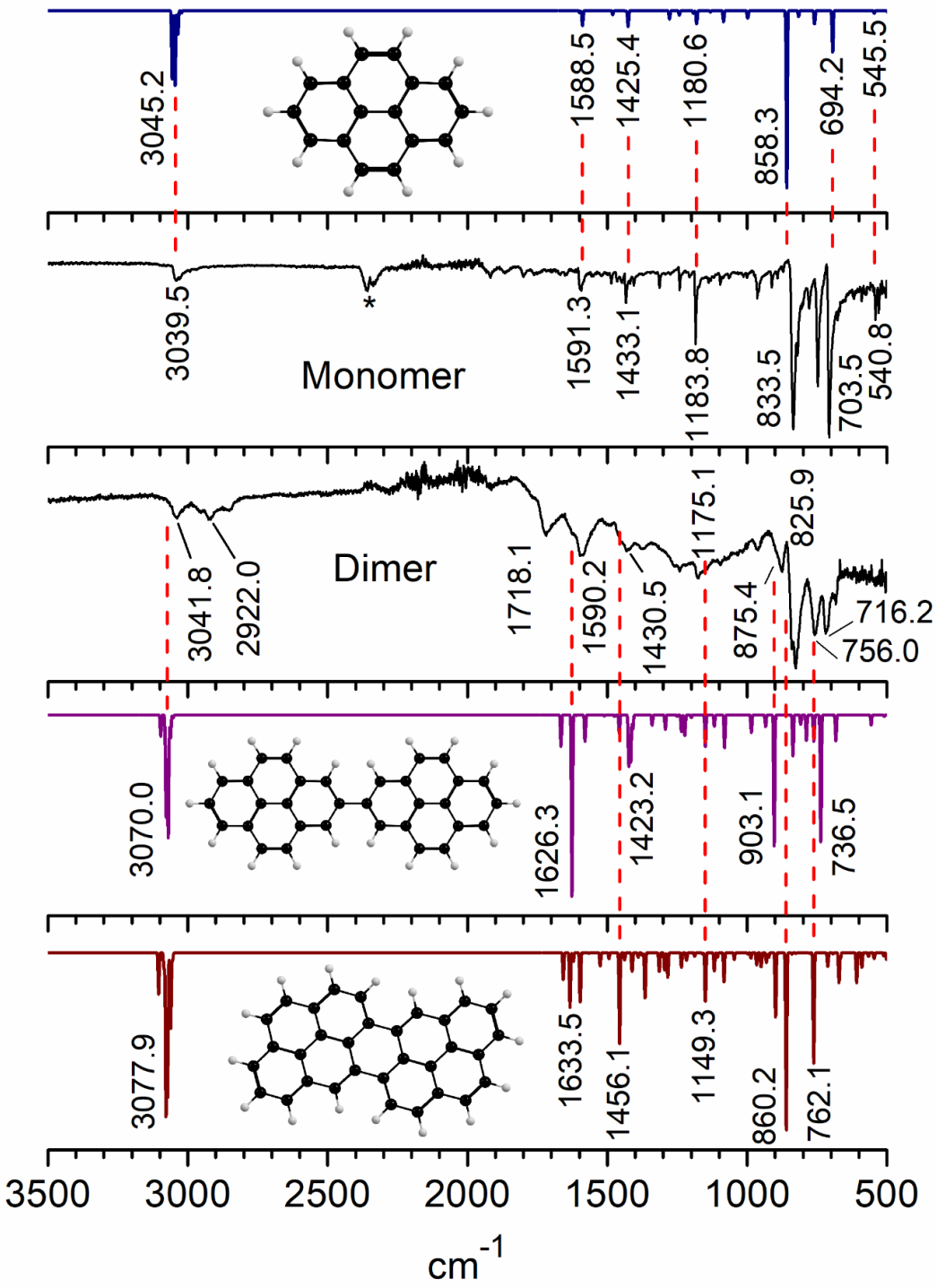

Figure 5.1. Comparison of pyrene monomer and dimer with most stable theoretical structures. Theory vibrations were scaled by 0.956. Asterisk denotes common CO_2 contamination peaks.

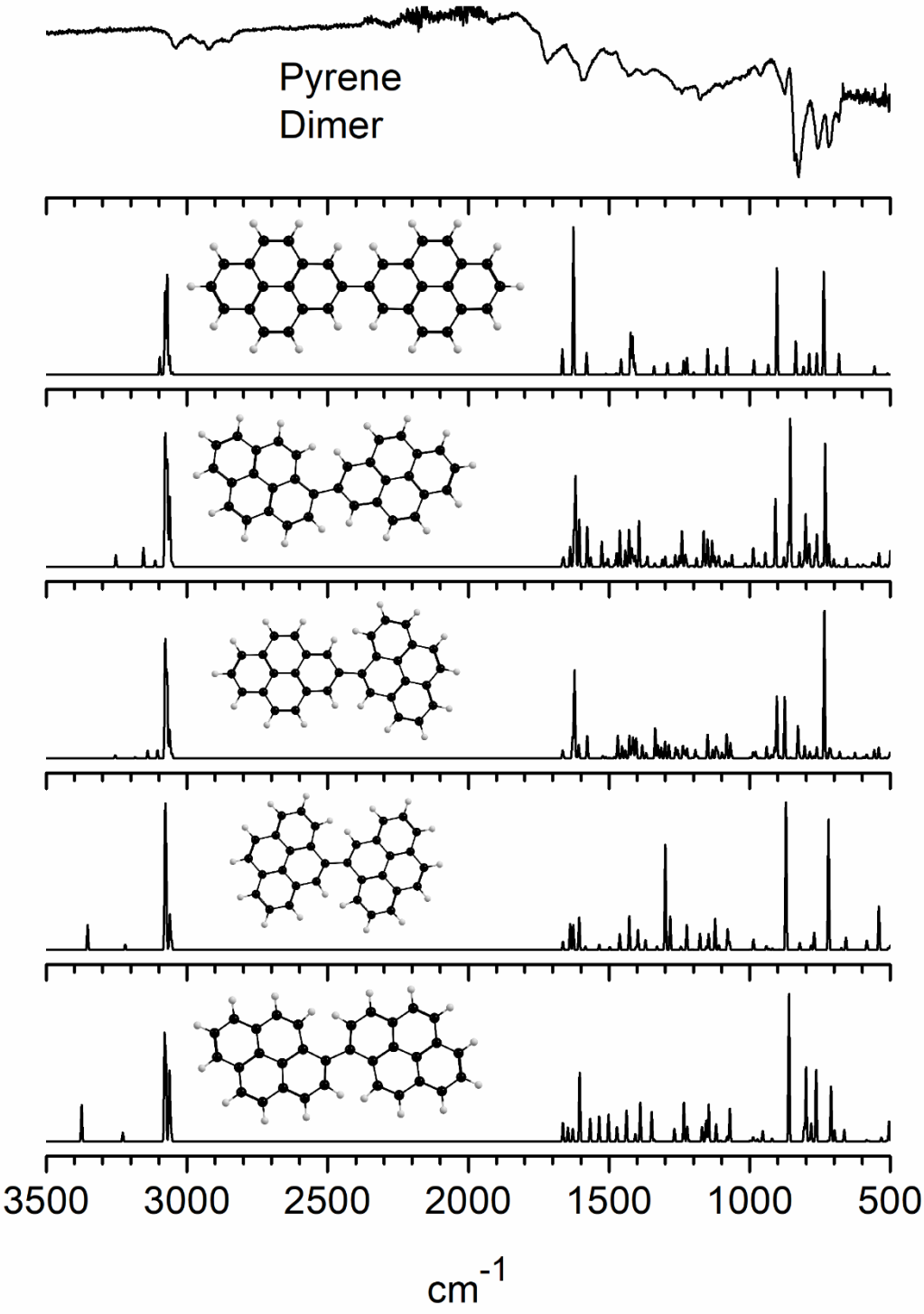

Figure 5.2. Pyrene singly-bonded dimers in comparison to collected purified results.

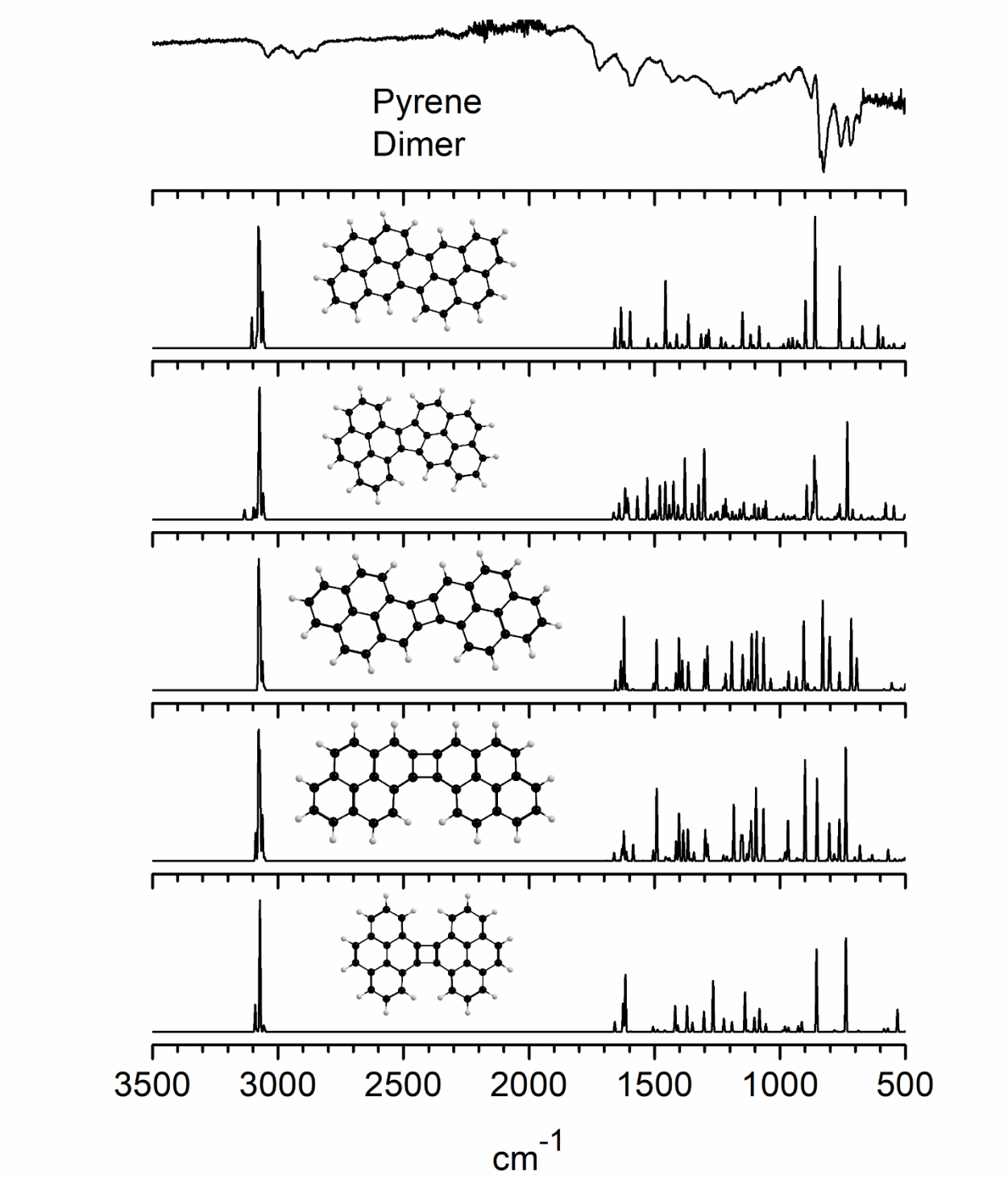

Figure 5.3. Pyrene doubly-bonded dimers in comparison to collected purified results.

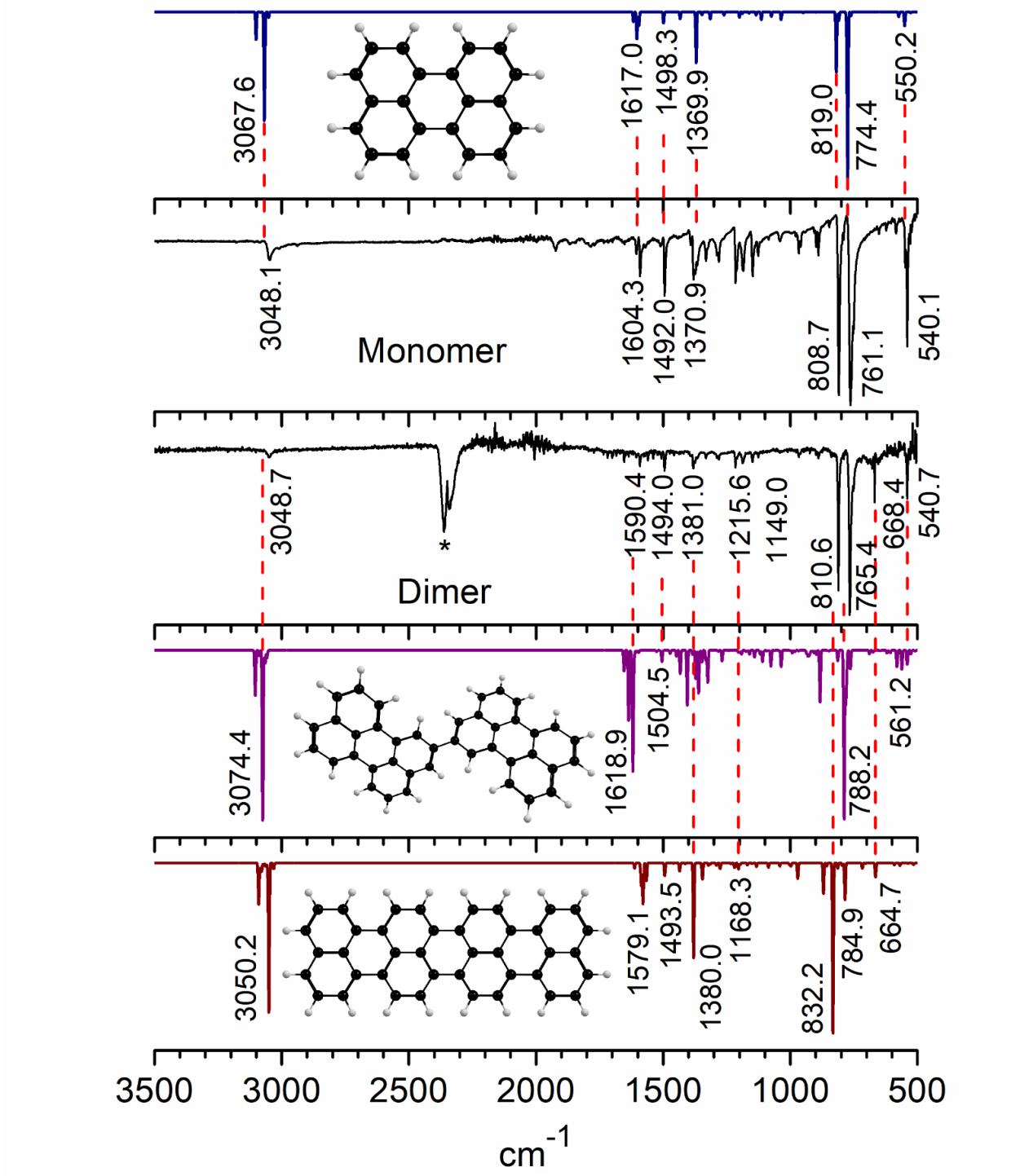

Figure 5.4. Comparison of perylene monomer and dimer with most stable theoretical structures. Theory vibrations were scaled by 0.956. Asterisk denotes common CO_2 contamination peaks.

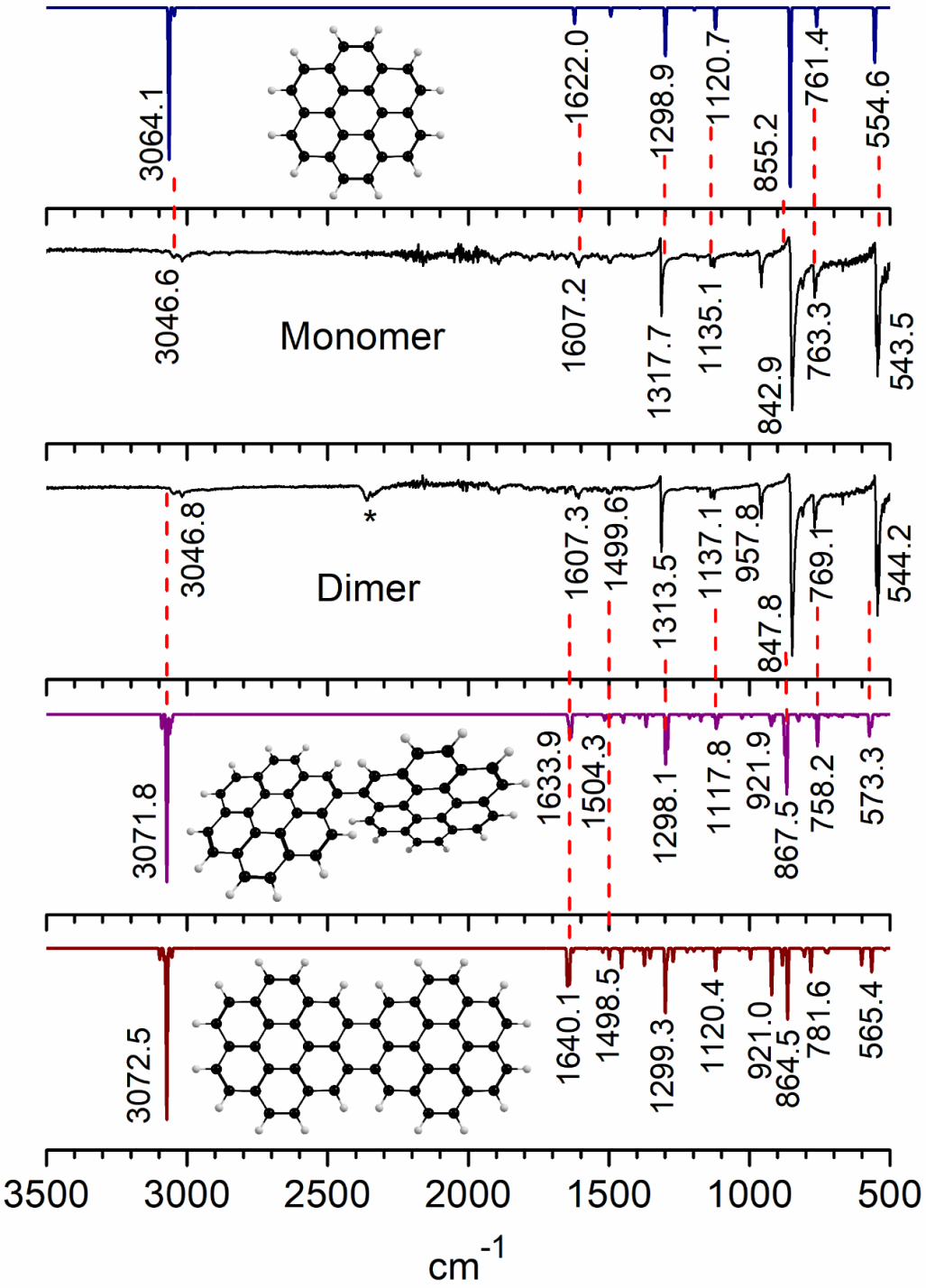

Figure 5.5. Comparison of coronene monomer and dimer with most stable theoretical structures. Theory vibrations were scaled by 0.956. Asterisk denotes common CO_2 contamination peaks.

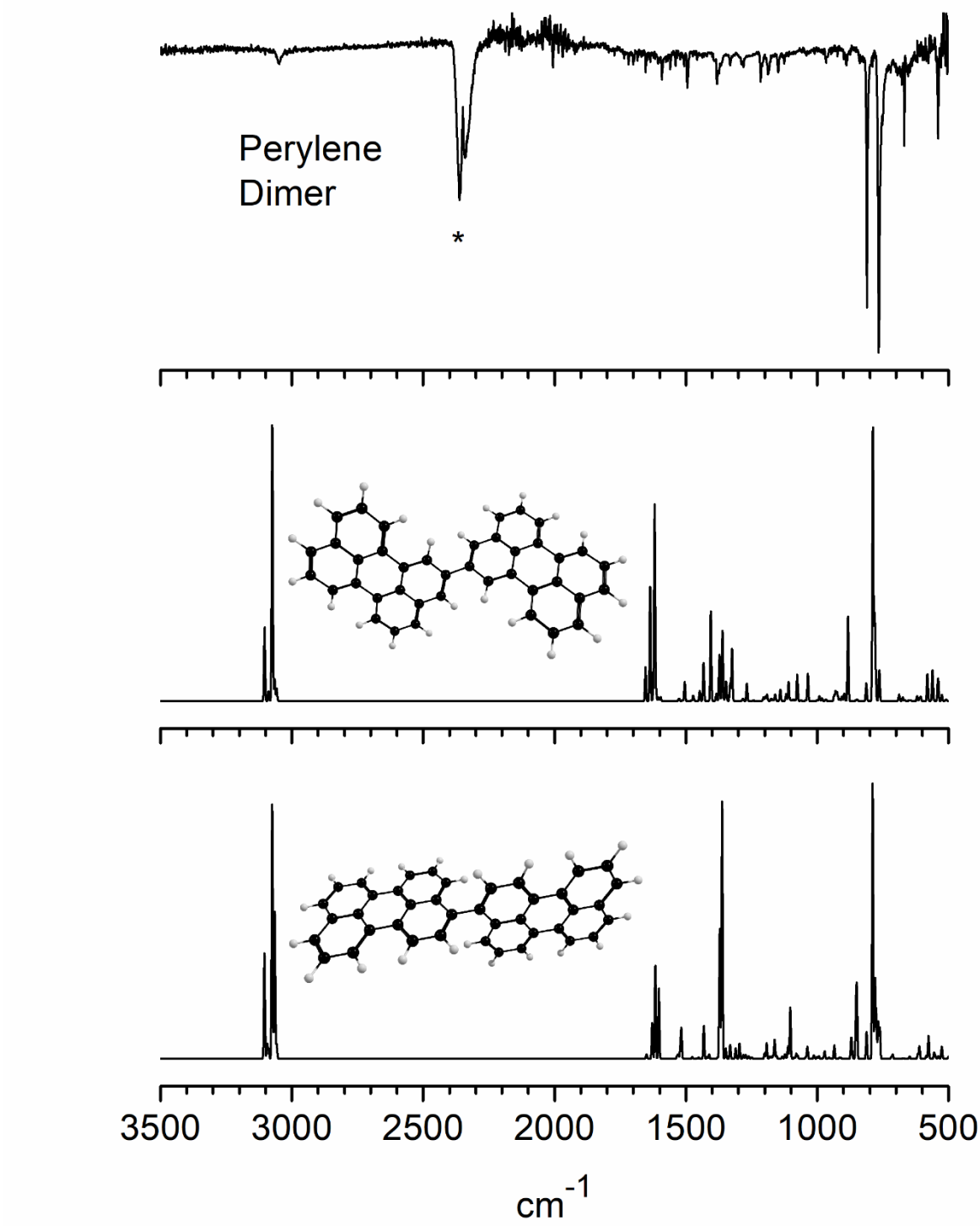

Figure 5.6. Perylene singly-bonded dimers in comparison to collected purified results. Asterisk denotes common CO_2 contamination peaks.

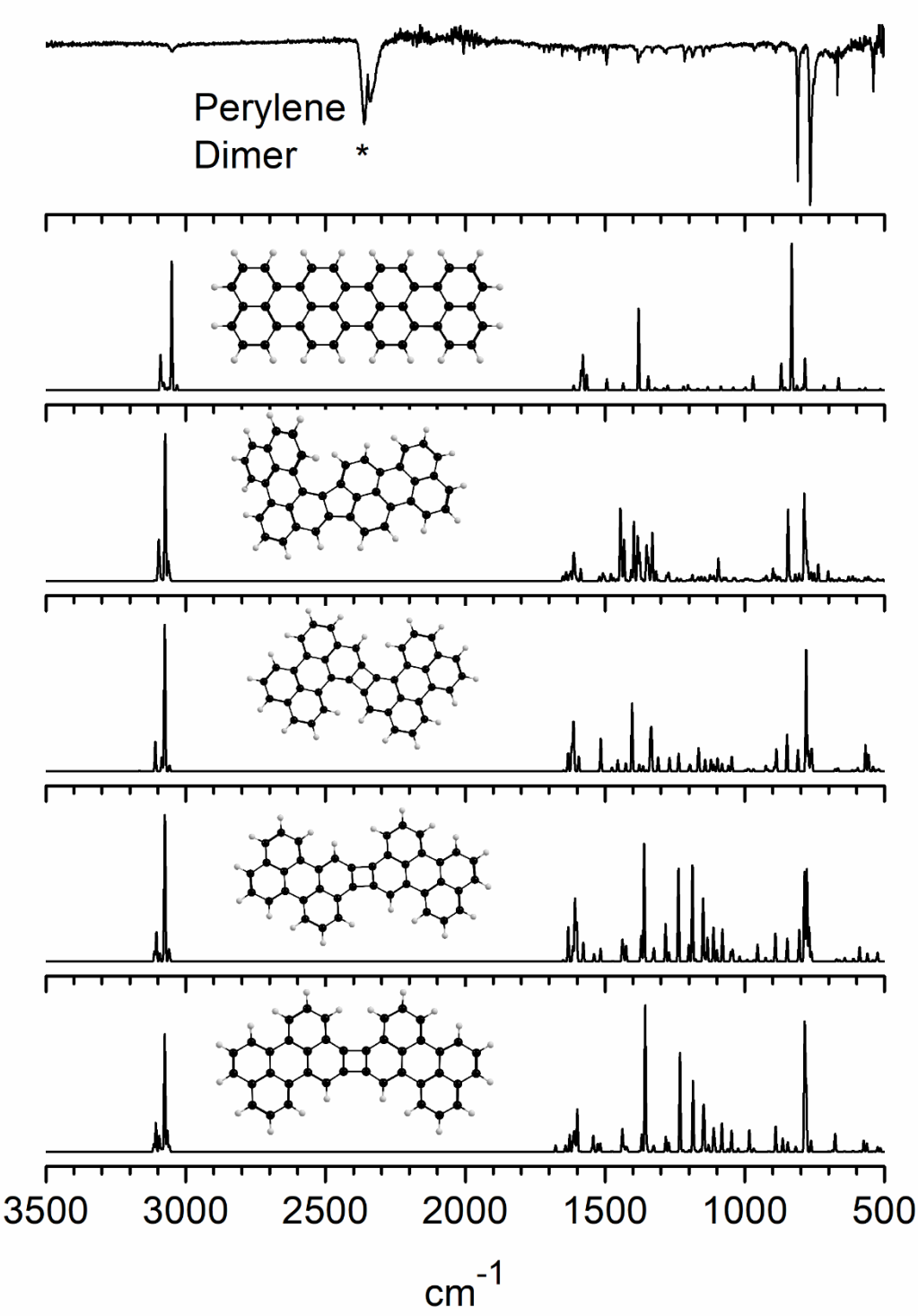

Figure 5.7. Perylene doubly-bonded dimers in comparison to collected purified results. Asterisk denotes common CO_2 contamination peaks.

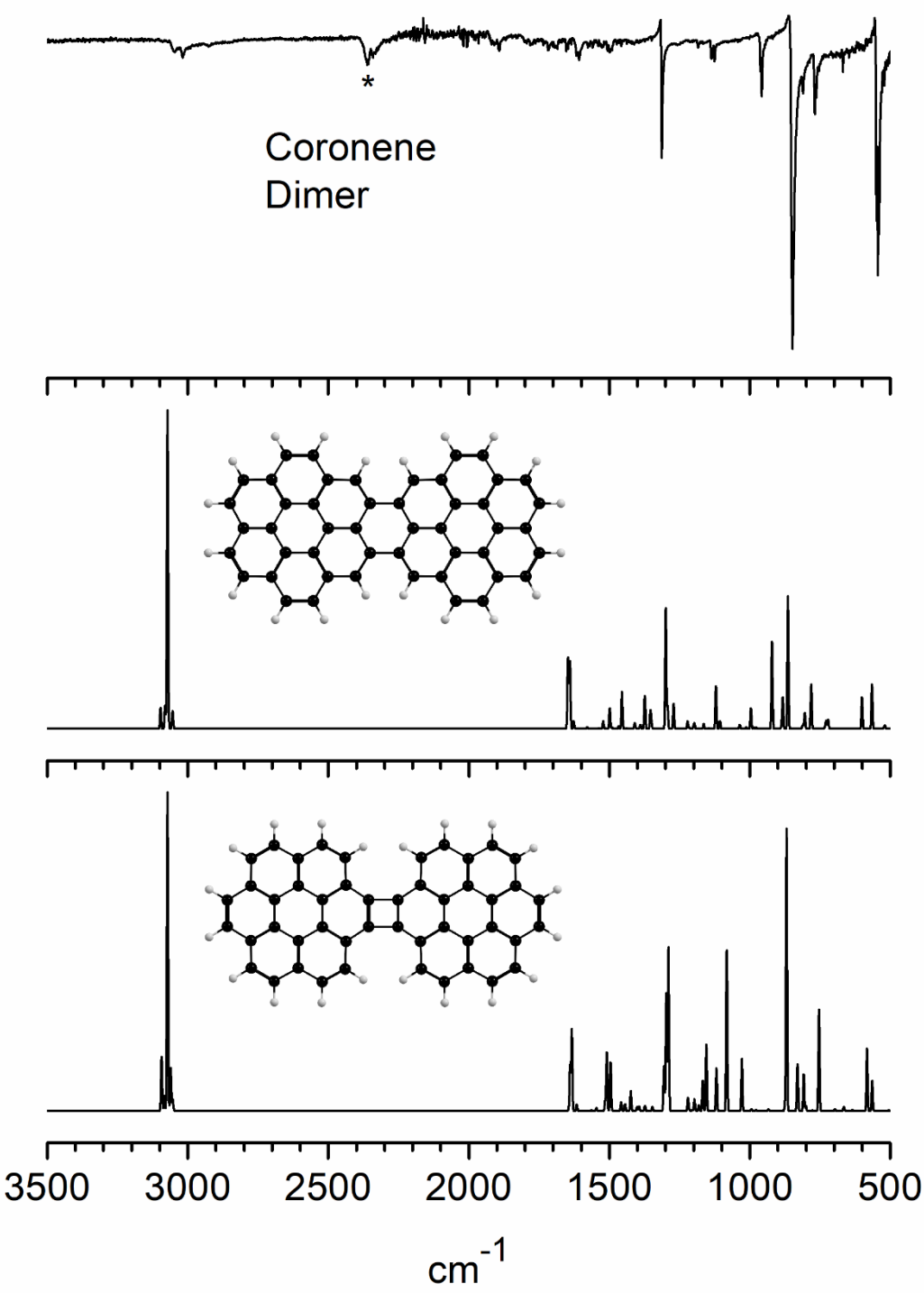

Figure 5.8. Coronene doubly-bonded dimers in comparison to collected purified results. Asterisk denotes common CO_2 contamination peaks.

References

1. Allamandola, L. J.; Tielens, A. G. G. M.; Barker, J. R. Polycyclic Aromatic Hydrocarbons and the Unidentified Infrared Emission Bands: Auto Exhaust Along the Milky Way! *Astrophys. J.* **1985**, *290*, L25-L28.
2. Allamandola, L. J.; Tielens, A. G. G. M.; Barker, J. R. Interstellar Polycyclic Aromatic Hydrocarbons: The Infrared Emission Bands, the Excitation/Emission Mechanism, and the Astrophysical Implications. *Astrophys. J., Suppl. Ser.* **1989**, *71*, 733-775.
3. Leger, A.; D'Hendecourt, L.; Defourneau, D. Physics of IR Emission by Interstellar PAH Molecules. *Astron. Astrophys.* **1989**, *216*, 148–164.
4. Hartquist, T. W.; Williams, D. A. *The Molecular Astrophysics of Stars and Galaxies*; International Series on Astron; Clarendon Press, 1998.
5. Henning, T.; Salama, F. Carbon in the Universe. *Science* **1998**, *282*, 2204–2210.
6. Bréchignac, P.; Pino, T.; Boudin, N. Laboratory Spectra of Cold Gas Phase Polycyclic Aromatic Hydrocarbon Cations, and Their Possible Relation to the Diffuse Interstellar Bands. *Spectrochim. Acta - Part A Mol. Biomol. Spectrosc.* **2001**, *57*, 745–756.
7. Malloci, G.; Mulas, G.; Joblin, C. Electronic Absorption Spectra of PAHs up to Vacuum UV. *A&A* **2004**, *426*, 105-117.
8. Tielens, A. G. G. M. *The Physics and Chemistry of the Interstellar Medium*; Cambridge University Press, 2005.
9. Snow, T. P.; Bierbaum V. M. Ion Chemistry in the Interstellar Medium. *Annu. Rev. Anal. Chem.* **2008**, *1*, 229-259.
10. Tielens, A. G. G. M. Interstellar Polycyclic Aromatic Hydrocarbon Molecules. *Annu. Rev. Astron. Astrophys.* **2008**, *46*, 289–337.

11. Draine, B. T. *Physics of the Interstellar and Intergalactic Medium*; Princeton University Press; 2011.
12. Tielens, A. G. G. M.; Snow, T. P. *The Diffuse Interstellar Bands*; Astrophysics and Space Science Library; Springer Netherlands, 2012.
13. Tielens, A. G. G. M. The Molecular Universe. *Rev. Mod. Phys.* **2013**, *85*, 1021-1081.
14. Sandford, S. A.; Nuevo, M.; Bera, P. P.; Lee, T. J. Prebiotic Astrochemistry and the Formation of Molecules of Astrobiological Interest in Interstellar Clouds and Protostellar Disks. *Chem. Rev.* **2020**, *120*, 4616-4659.

Chapter 6

Raman Spectroscopy

The Raman spectra of PAH dimers are of less interest in comparison to astrophysical spectra, but a comparison with extended carbon framework materials, such as graphene, is of interest. As the PAHs are extended in size, they should start to take on properties of graphene as they reach nanographene sizes. Graphene has several distinct Raman bands that large PAHs may begin to approach. Pure single-layer graphene has a strong Raman band at 1582 cm^{-1} known as the "G" band caused by planar carbon ring distortion. A second band at 1350 cm^{-1}, known as the "D" band, is the result of any defects in the carbon lattice, with an overtone at 2700 cm^{-1} known as the "2D" band. The 2D band is sharp and intense for monolayer graphene and broadens as multiple graphene layers are stacked.[1-12] PAHs are known to have bands at similar frequencies to the G and D bands, but notably lack any bands at the 2D overtone position. The position of these peaks may shift closer to the graphene peaks as the structures begin to reach more graphene-like shapes.

To examine the Raman spectra of the synthesized PAHs, collected samples were suspended in HPLC grade methanol and dropcast onto prepared silver surface enhanced Raman (SERS) substrates. For comparison, the commercial monomer materials were also examined under the same conditions. Samples were examined using a Thermo Scientific DXR Raman Microscope with both a 532 and 780 nm laser. Both lasers were tested to see which wavelength provided better results. Laser powers were adjusted before each scan to optimize signal to noise

ratios. Spectra were scanned from 100 to 3500 cm^{-1} with a 5 cm^{-1} full width at half-maximum. Samples were recorded over 50 average scans with 100 background scans.

The spectra of the PAH samples lack any easily assignable new spectral peaks. In the case of pyrene and perylene, the peaks are significantly broadened compared to the monomer spectra. Figures 6.1 and 6.2 show the comparison of the monomer and dimer spectra with the most stable theory predictions for pyrene and perylene respectively. Similar spectra for coronene are presented in Figure 6.3. The spectrum of coronene dimer shows almost no change compared with the monomer and both spectra keep sharp distinct peaks rather than the dimer broadening present in the pyrene and perylene spectra. The high symmetry of the coronene dimers results in the singly-bonded coronene dimer having a spectrum nearly identical to that of the monomer.

Aside from the broadening of the major peaks of the Raman spectra, there is a shift in the low-frequency bands in the 500-600 cm^{-1} region. For pyrene, the 591.9 cm^{-1} band of the monomer shifts to 477.6 cm^{-1} for the dimer. In perylene's spectra, the 549.0 cm^{-1} band shifts to 481.8 cm^{-1}. The shift in coronene is significantly smaller, changing from 482.6 cm^{-1} to 481.9 cm^{-1} in the dimer. These bands are assigned to the C-H bending modes and the increased steric hindrance of the dimer structures would shift the peaks. Much the same as the previously discussed infrared spectra, agreement between the theory and experiment is not perfect. Possibly more rigorous theoretical calculations could also improve the agreement between the computational Raman spectra and the experiment. Other possible PAH dimer structures were examined to check for significant agreement as a possible identifier of the dimer structures formed. Figures 6.4 and 6.5 present the other pyrene structures. Figures 6.6 and 6.7 show the same for perylene. Figure 6.8 presents the coronene doubly-bonded structures.

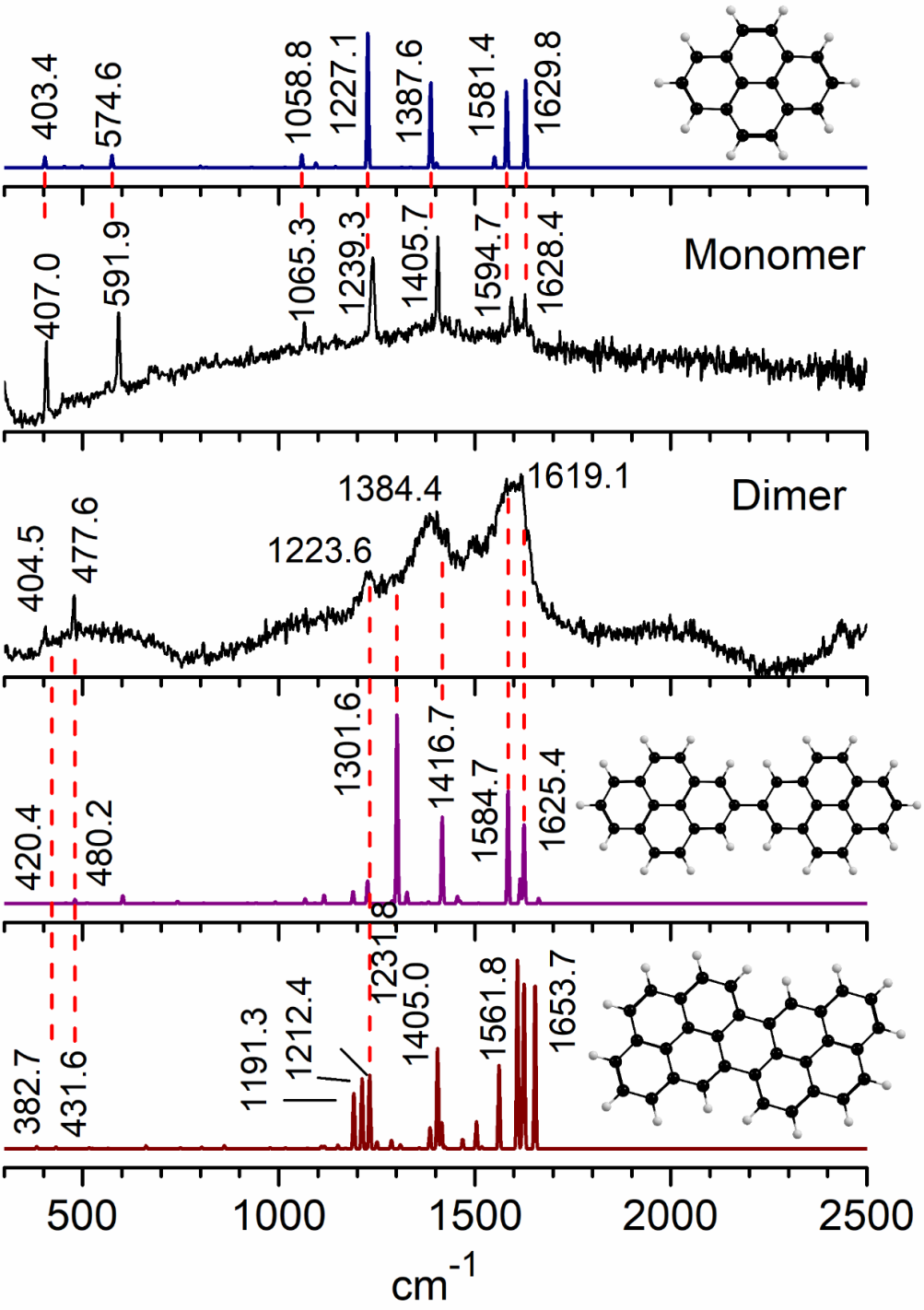

Figure 6.1. Comparison of pyrene monomer and dimer with most stable theoretical structures. Theory vibrations were scaled by 0.956.

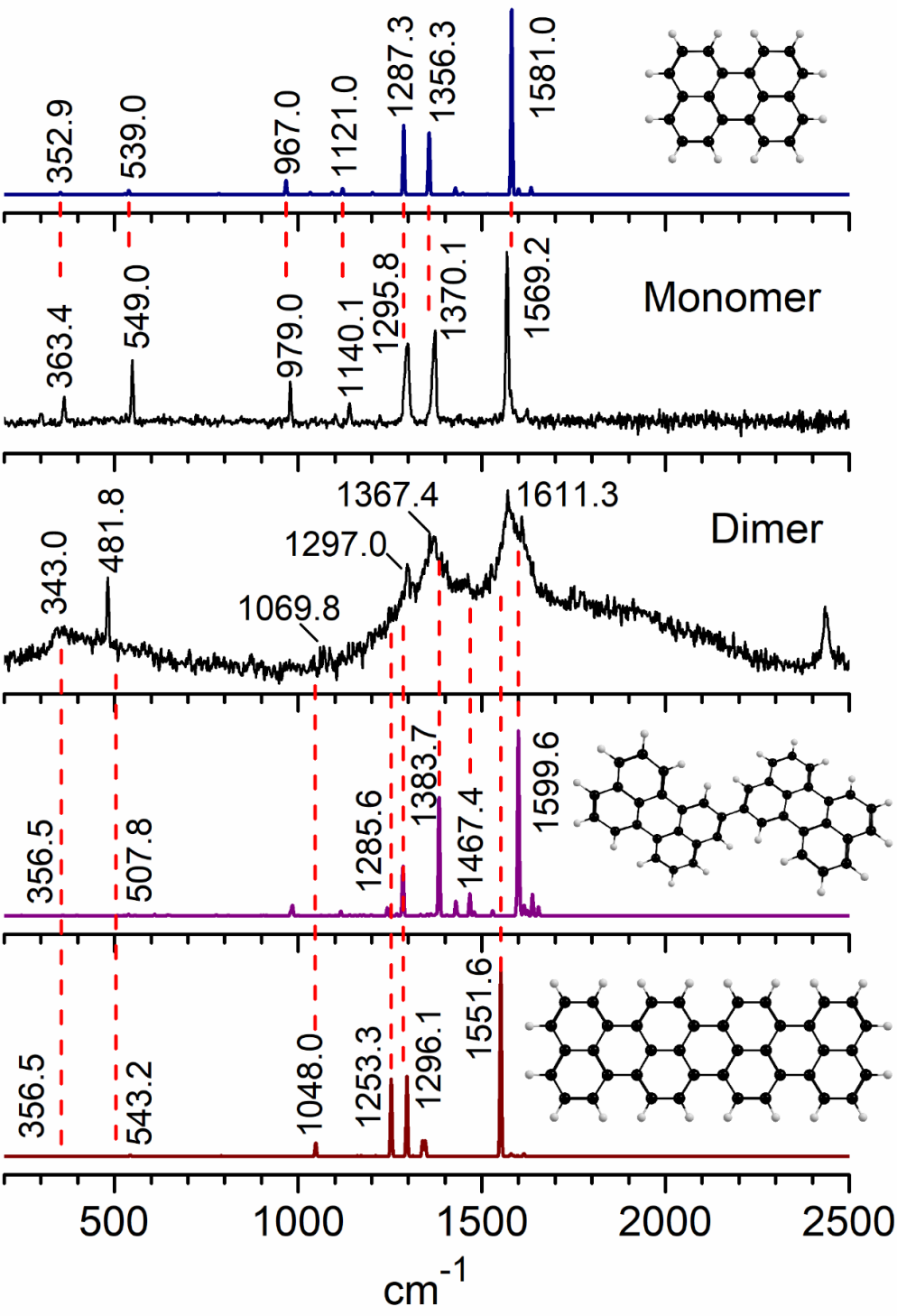

Figure 6.2. Comparison of perylene monomer and dimer with most stable theoretical structures. Theory vibrations were scaled by 0.956.

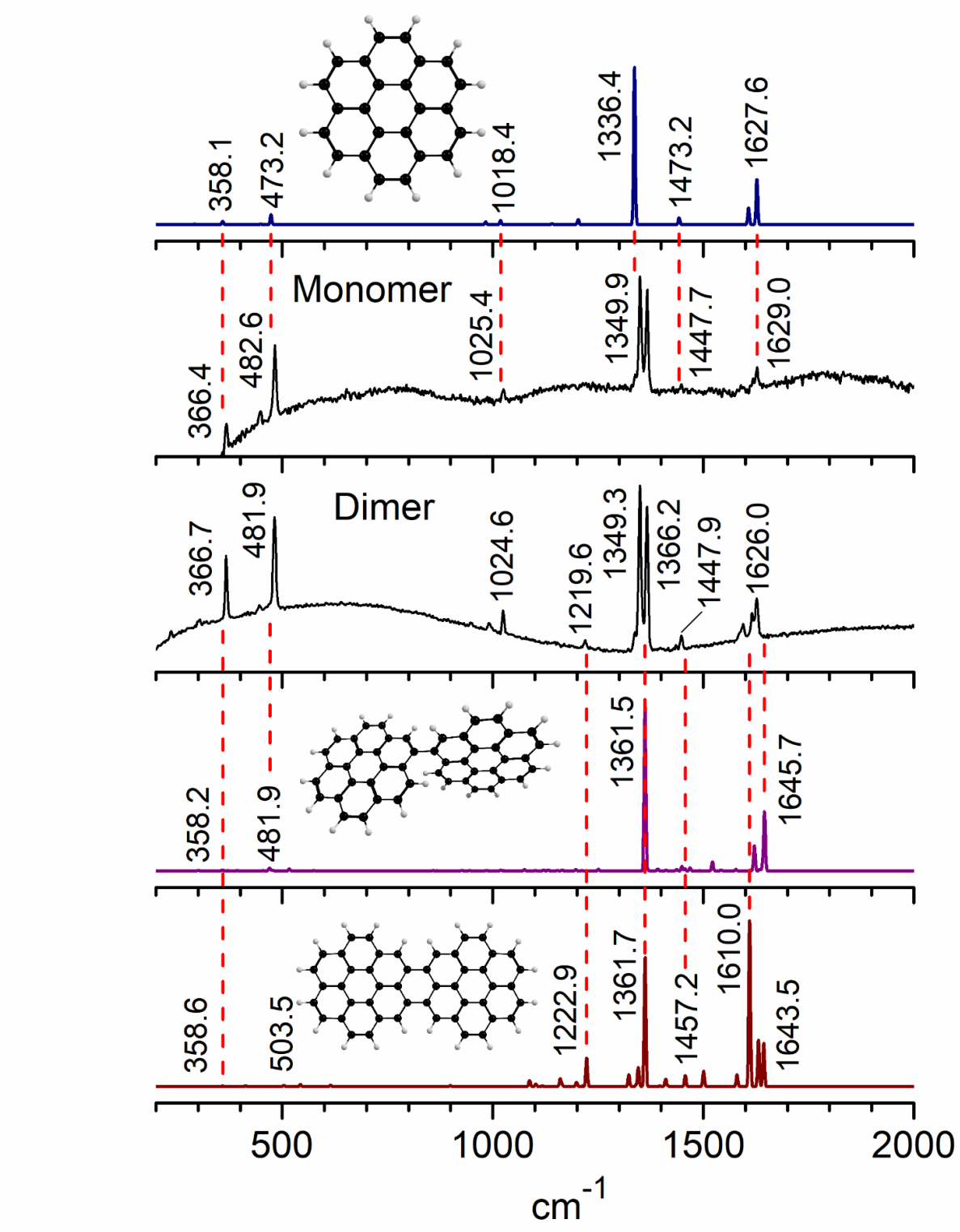

Figure 6.3. Comparison of coronene monomer and dimer with most stable theoretical structures. Theory vibrations were scaled by 0.956.

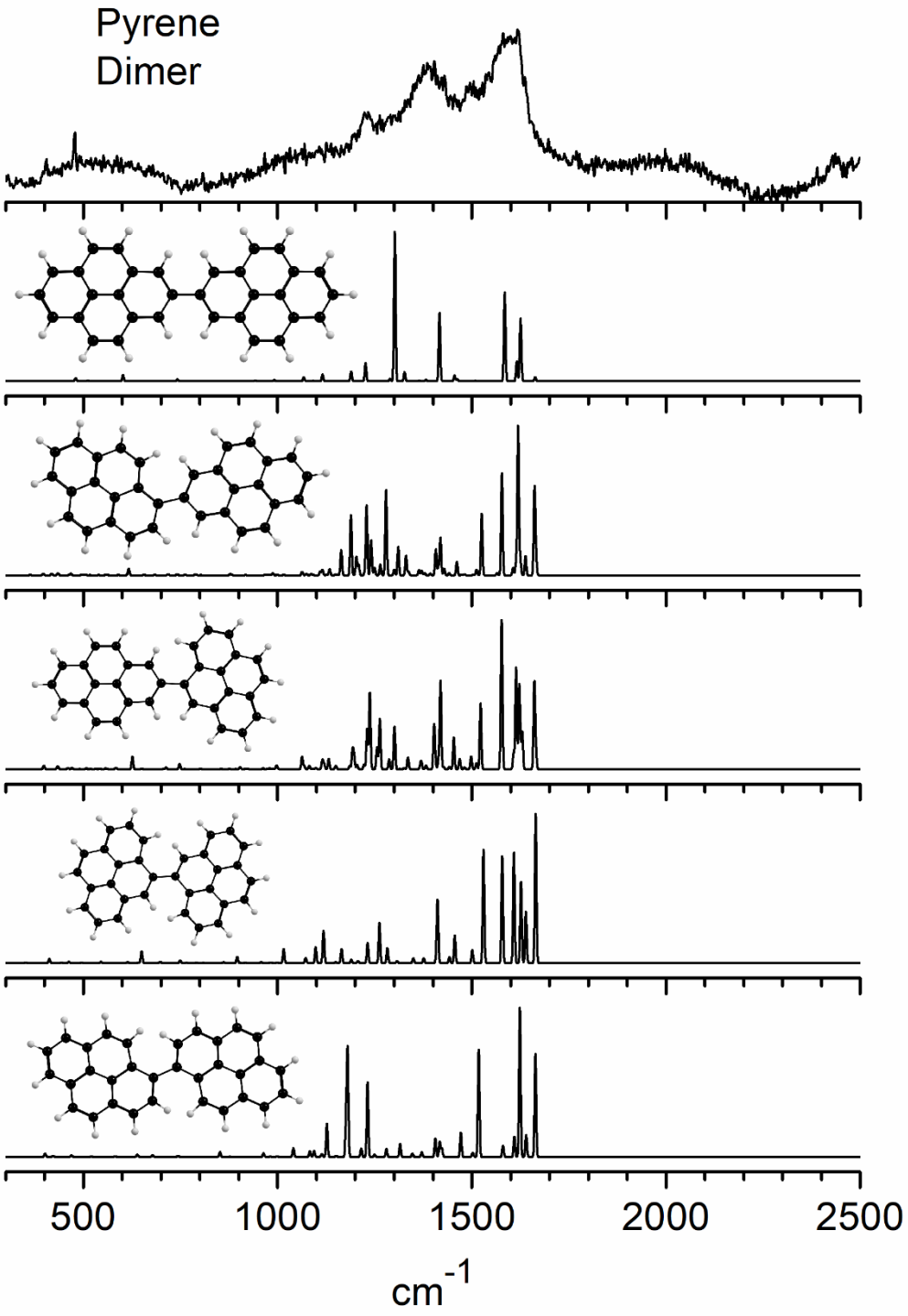

Figure 6.4. Pyrene singly-bonded dimers in comparison to results for the collected purified samples.

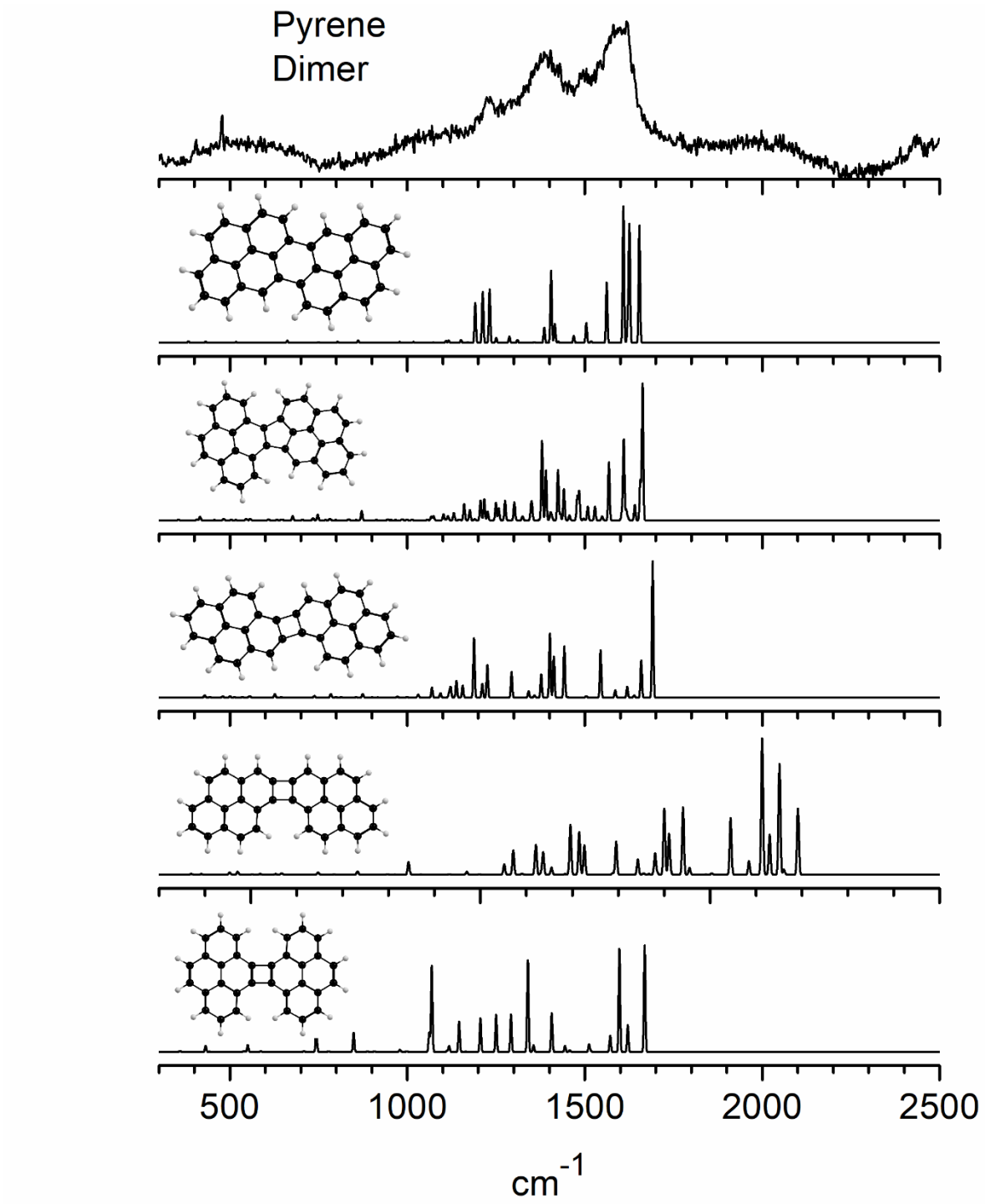

Figure 6.5. Pyrene doubly-bonded dimers in comparison to results for the collected purified samples.

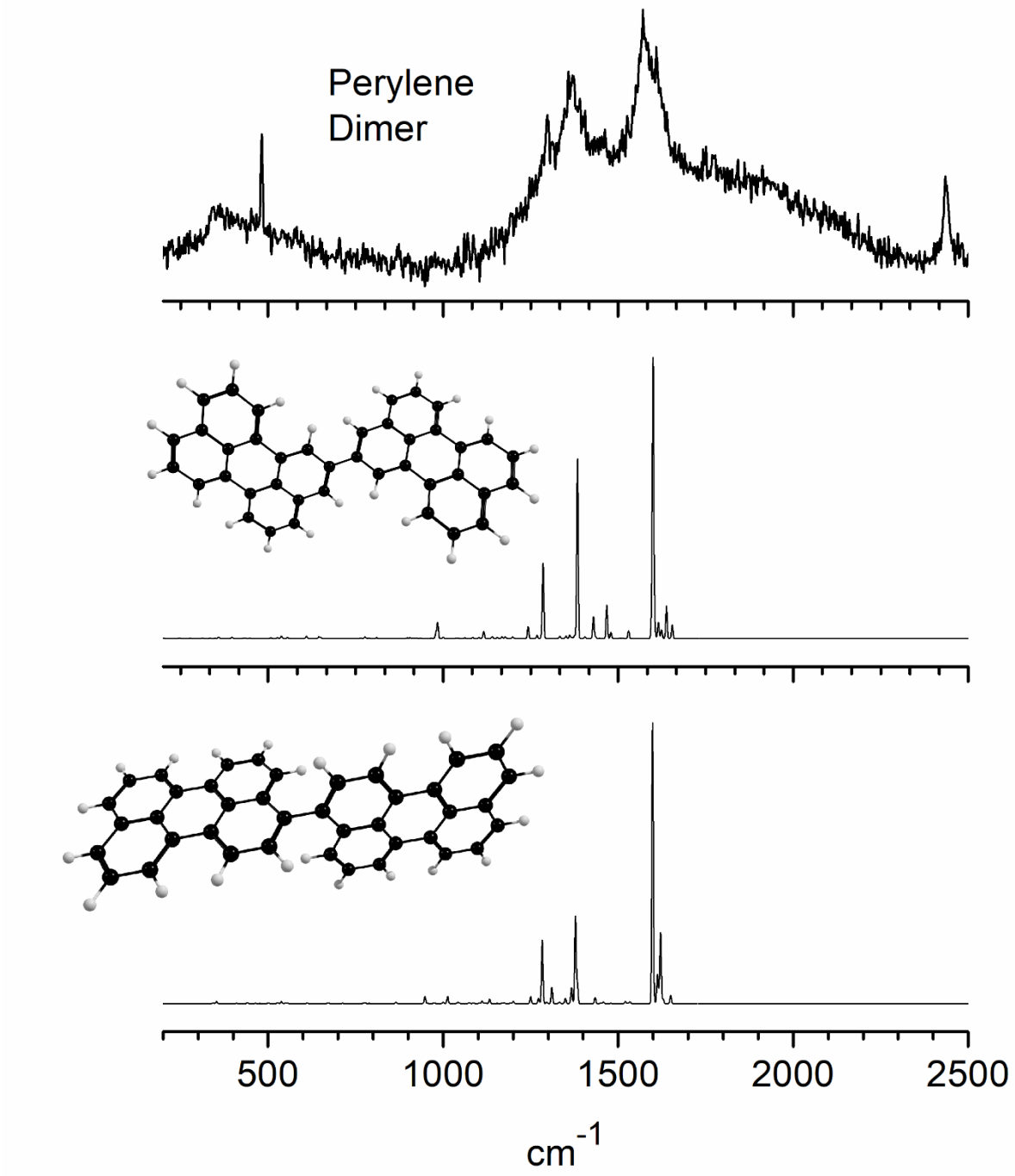

Figure 6.6. Perylene singly-bonded dimers in comparison to results for the collected purified samples.

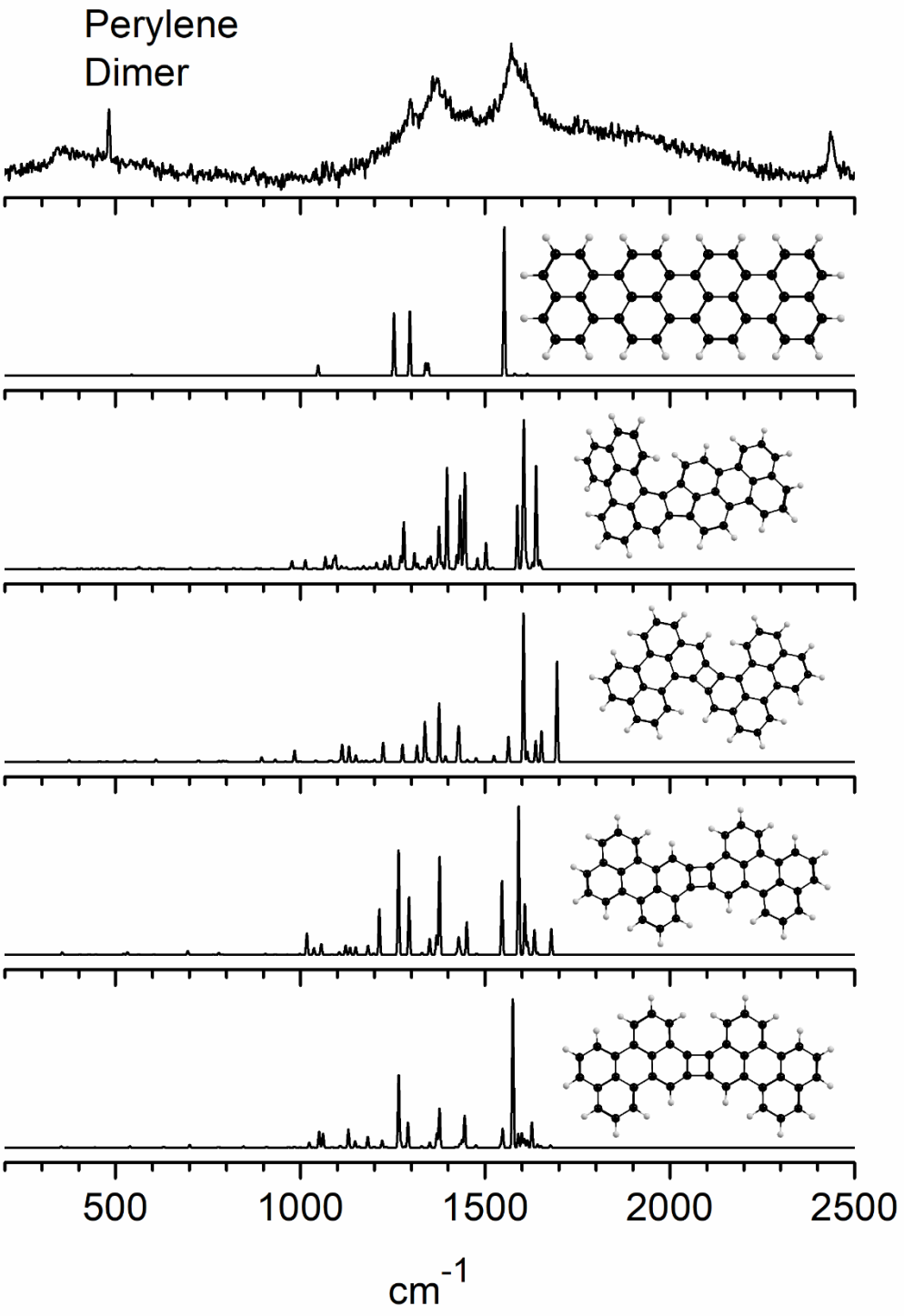

Figure 6.7. Perylene doubly-bonded dimers in comparison to results for the collected purified samples.

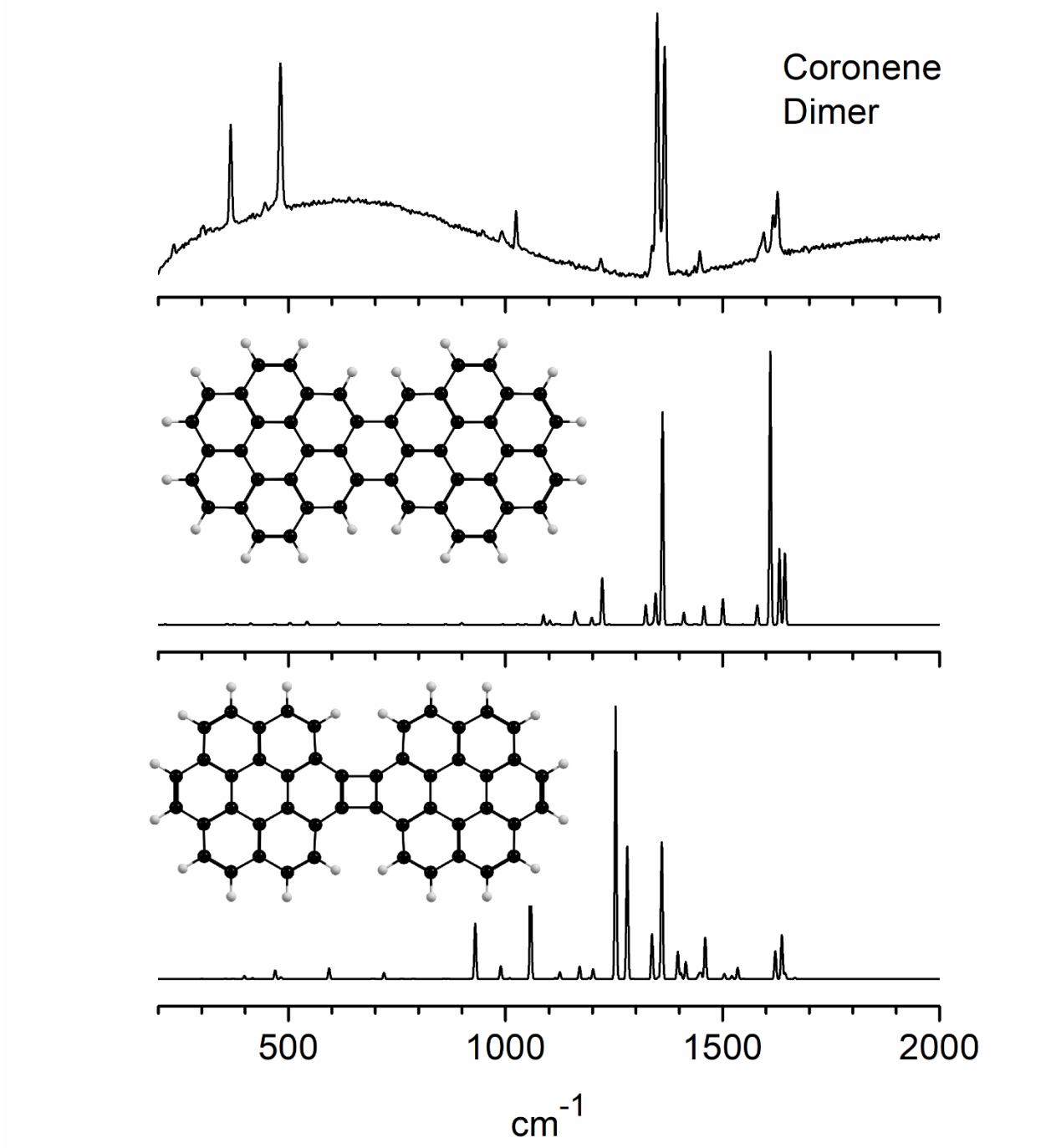

Figure 6.8. Coronene doubly-bonded dimers in comparison to results for the collected purified samples.

References

1. Dresselhaus, M. S.; Dresselhaus, G.; Eklund, P. C. *Science of Fullerenes and Carbon Nanotubes: Their Properties and Applications*; Elsevier Science, 1996.
2. Anthony, J. E. Functionalized Acenes and Heteroacenes for Organic Electronics. *Chem. Rev.* **2006**, *106*, 5028-5048.
3. Ferrari, A. C.; Meyer, J. C.; Scardaci, V.; Casiraghi, C.; Lazzeri, M.; Mauri, F.; Piscanec, S.; Jiang, D.; Novoselov, K. S.; Roth, S.; Geim, A. K. Raman Spectrum of Graphene and Graphene Layers. *Phys. Rev. Lett.* **2006**, *97*, 187401-187404.
4. Wu, J.; Pisula, W.; Müllen, K. Graphenes as Potential Material for Electronics. *Chem. Rev.* **2007**, *107*, 718-747.
5. Geim, A. K. Graphene: Status and Prospects. *Science* **2009**, *324*, 1530–1534.
6. Malard, L. M.; Pimenta, M. A.; Dresselhaus, G.; Dresselhaus, M. S. Raman Spectroscopy in Graphene. *Phys. Rep.* **2009**, *473*, 51–87.
7. Rao, C. N. R.; Sood, A. K.; Subrahmanyam, K. S.; Govindaraj, A. Graphene: The New Two-Dimensional Nanomaterial. *Angew. Chem. Int. Ed.* **2009**, *48*, 7752-7777.
8. Allen, M. J.; Tung, V. C.; Kaner, R. B. Honeycomb Carbon: A Review of Graphene. *Chem. Rev.* **2010**, *110*, 132-145.
9. Dresselhaus, M. S.; Jorio, A.; Hofmann, M.; Dresselhaus, G.; Saito, R. Perspectives on Carbon Nanotubes and Graphene Raman Spectroscopy. *Nano Lett.* **2010**, *10*, 751–758.
10. Talyzin, A. V.; Anoshkin, I. V.; Krasheninnikov, A. V.; Nieminen, R. M.; Nasibulin, A. G.; Jiang, H.; Kauppinen, E. I. Synthesis of Graphene Nanoribbons Encapsulated in Single-Walled Carbon Nanotubes. *Nano Lett.* **2011**, *11*, 4352-4356.
11. Chen, L.; Hernandez, Y; Feng, X.; Müllen, K. From Nanographene and Graphene

Nanoribbons to Graphene Sheets: Chemical Synthesis. *Angew. Chem. Int. Ed.* **2012**, *51*, 7640-7654.

12. Tan, C.; Cao, X; Wu, X.; He, Q.; Yang, J.; Zhang, X.; Chen, J.; Zhao, W.; Han, S.; Nam, G.; et al. Recent Advances in Ultrathin Two-Dimensional Nanomaterials. *Chem. Rev.* **2017**, *117*, 6225-6331.

Chapter 7

UV-Visible Spectroscopy

Samples dissolved in HPLC grade cyclohexane, purchased from Sigma-Aldrich, were examined using a Horiba Scientific Duetta Fluorescence and Absorbance Spectrometer. Reflectance off thin-film samples drop cast onto quartz slides was attempted, but results were lower quality than those for the dissolved samples. Samples were scanned from 200 to 800 nm with a resolution of 1 and a 0.5 nm stepsize. Background scans of pure cyclohexane were taken before each run to account for solvent peaks. Sample concentrations were adjusted to prevent saturation of the detector.

As discussed in Chapter 4, the theoretical computations for simulating the UV-Visible absorption spectra of the dimers were achieved through the use of TD-DFT calculations. Predicted spectra are the vertical transitions from the optimized ground electronic state without inclusion of vibronic activity via Franck-Condon factors. Comparison of the predicted spectra with known monomer peaks was used to determine a scaling factor of 1.13 for the wavelength shift. The scaling factor was uniformly applied across the full spectral range for all computational results.

Figure 7.1 shows the spectral comparison of pyrene monomer and dimer with the most stable dimer predictions. The pyrene monomer contains three primary bands at 238.6, 271.9, and 333.8 nm with higher energy structure on each of the peaks. These higher energy bands are attributed to vibronic activity which is not accounted for with theory calculations. With the scaling factor, the pyrene monomer theory matches fairly well with the known transitions. The

dimer spectrum contains additional peaks including a strong new transition at 301.5 nm and a second series of peaks doubling up on the bands at 333.8 nm at slightly lower energy. The singly-bonded structure explains the new 301.5 nm transition with fairly close accuracy and other peaks fit within the spectrum. The doubly-bonded dimer should have a lower energy transition around 487.0 nm with rather strong intensity, but no significant peaks can be detected in that region. A pair of transitions around 273.9 nm could explain the new multiplet of peaks around 272.2 nm and other predicted spectral features overlap with already present monomer peaks but may explain some of the broadening seen in the dimer spectrum. These new peaks suggest that the dimer is made up of a mixture of both the singly and doubly-bonded dimers which is in agreement with the mass spectra previously shown. The samples also may still contain residual monomer material that needs to be removed through further purification. The only significant unaccounted for peak is the HOMO-LUMO transition at 478.0 nm in the doubly-bonded dimer, but theory calculations struggle with accurately predicting the HOMO-LUMO transition in aromatic molecules as the other samples also show. For comparison, a spectrum of the pyrene doubly-bonded dimer without scaling is presented in Figure 7.2 compared against experiment. The theoretical data could still be accounted for by the peaks present in the experimental spectrum, with the exception of the HOMO-LUMO transition at 423.0 nm. To check the other possible structures, Figures 7.3 and 7.4 present the theoretical transitions of the singly and doubly-bonded dimers respectively.

Figure 7.5 shows the comparison of the perylene monomer and dimer UV-Vis absorption spectra with the most stable singly and doubly-bonded structures predicted by theory. The monomer has two main transitions at 430.6 and 252.0 nm. Monomer theory with scaling matches fairly well with transitions predicted at 439.8 and 250.1 nm. Again, the transitions also have

vibronic structure at slightly higher energy than the main transitions. The dimer spectrum loses much of the peak around 252.0 nm to a rising background that blocks out most of the spectrum below 278 nm. A couple of multiplets around 302.3 and 338.6 nm also show up in the dimer spectrum along with a small broad transition at 567.9 nm. The theoretical transitions do not match up with any of the major transitions for either of the most stable dimers and the HOMO-LUMO transition of the doubly-bonded dimer does not align with the new small broad peak at 567.9. However, the major peaks from the two predicted dimers align with the same transitions as the monomer peaks. Interestingly, the dimer theory without scaling more closely aligns with the dimer transitions. Figure 7.6 compares the experimental perylene dimer transitions to the most stable perylene doubly-bonded dimer theory without scaling. The HOMO-LUMO transition at 551.6 now more closely aligns with the 567.9 transition in the dimer, though the intensity is very different. The other peaks from the dimer align with the rising baseline below 278 nm. For other comparisons of the perylene spectra, Figures 7.7 and 7.8 present the spectra of scaled singly and doubly-bonded dimers of perylene to the experimental data. The most stable structures align best with the experimental data.

Coronene has even fewer transitions than the other two molecules as presented in Figure 7.9. The monomer theory predicts a peak at 301.0 and 206.5 nm with scaling. The first transitions match well with the most prominent transition in the spectrum and the second peak is present in the region starting to be covered by the cyclohexane solvent, though some amount of rising background there might indicate a transition aside from the solvent. Interestingly, the first transition in the coronene monomer spectrum at 338.0 is not predicted to align with any transitions, though the issues with predicting aromatic HOMO-LUMO transitions has already been noted from the prior two molecules. The dimer spectrum contains a sharp increase in the

intensity of the transition at 292.0 nm which appears to be a higher energy vibronic structure in the monomer spectrum. Additionally, two new peaks at 225.0 and 239.0 nm also provide important new transitions. However, the scaled theory spectra match rather poorly both in position and intensity to the dimer spectrum obtained. The singly-bonded dimer transitions align rather well with the monomer transitions, which is not too surprising given the structure of the dimer. The doubly-bonded dimer bands are slightly off from the new dimer peaks in the higher region, and the HOMO-LUMO transition does not match with any spectral intensity in the dimer experiment. However, if the scaling for the doubly-bonded dimer is removed, as depicted in Figure 7.10, the spectrum aligns much more closely. The HOMO-LUMO transition is now at 418.8 nm which is relatively close to a small bump at 410.5 nm. The main transitions are shifted to 292.7 and 297.7 nm which match closely with the two largest peaks at 292.0 and 299.8 nm respectively in the experiment. The two new transitions at 255.0 and 239.0 nm are fairly close to two new intense transitions predicted at 216.3 and 235.2 nm respectively and would match up with a slight positive scaling factor in this region. The coronene theory matches fairly well with the new spectral transitions when scaling is not accounted for. The doubly-bonded structures may need less scaling when compared with the monomer or singly-bonded options. For full comparison, the other doubly-bonded structure is also compared against the experimental results in Figure 7.11. The most stable dimer continues to have closer agreement to the collected dimer data.

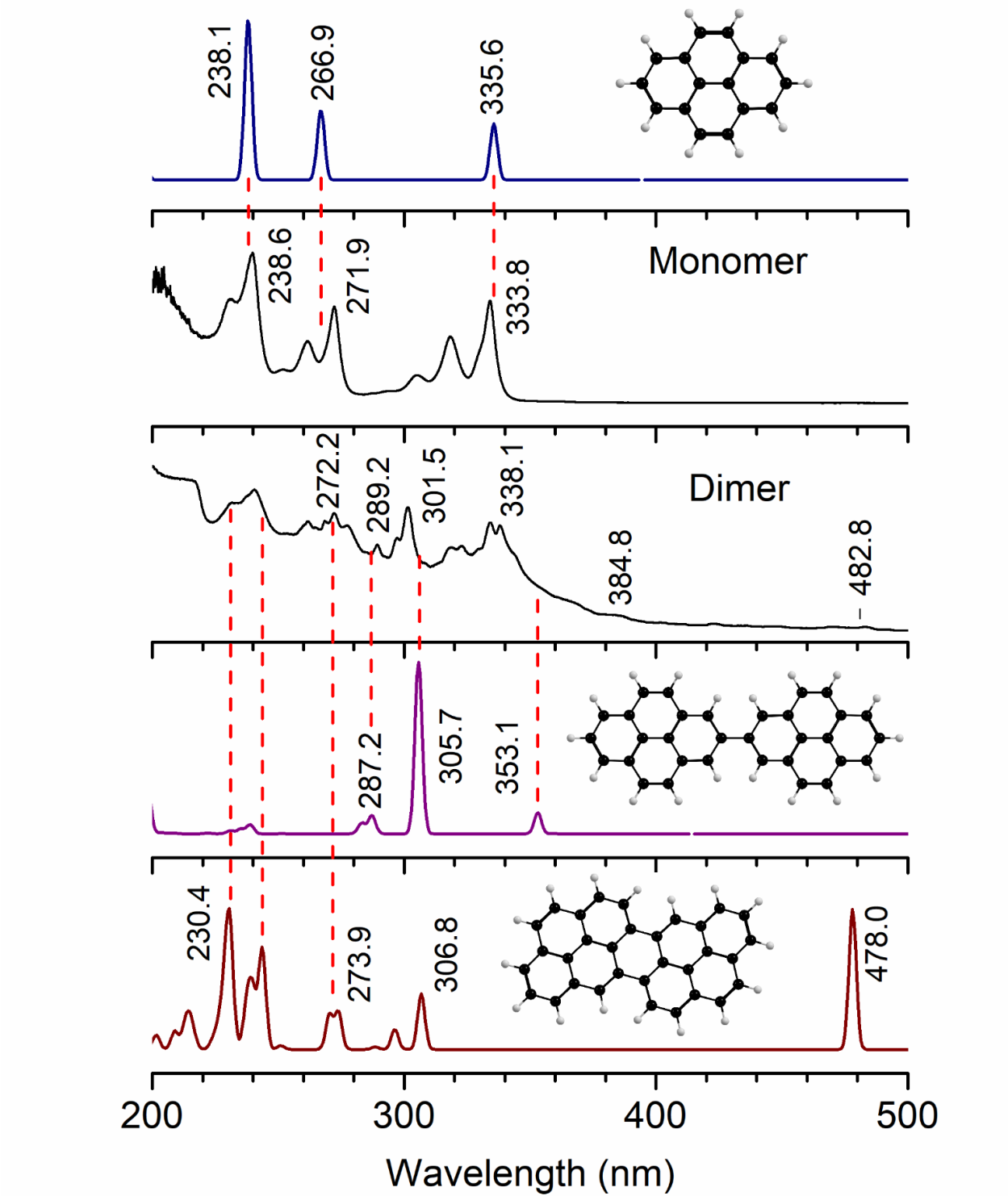

Figure 7.1. Comparison of pyrene monomer and dimer dissolved in cyclohexane with most stable theoretical structures. Theory transitions were scaled by 1.13.

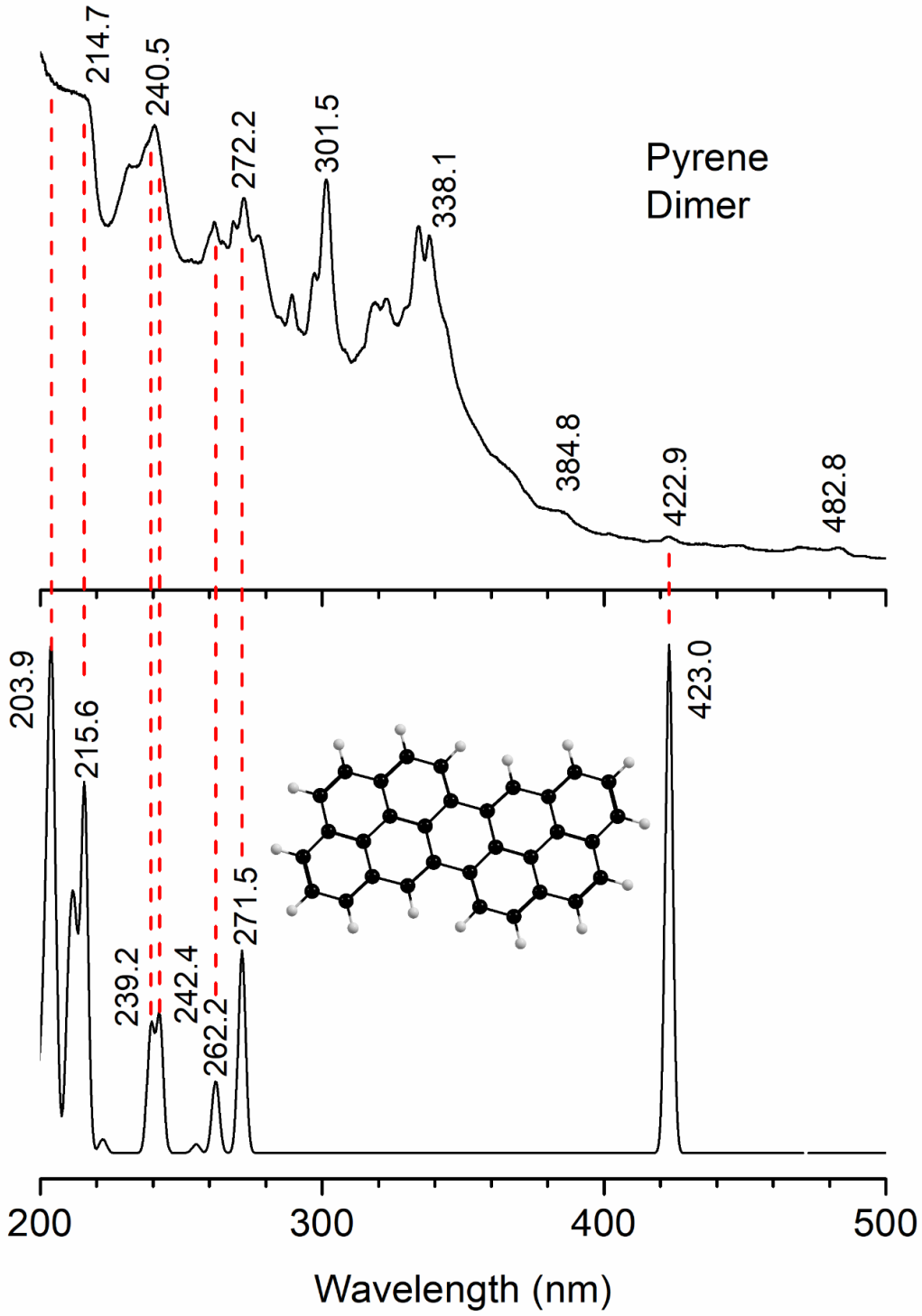

Figure 7.2. Comparison of pyrene dimer dissolved in cyclohexane with theory dimer without scaling factor.

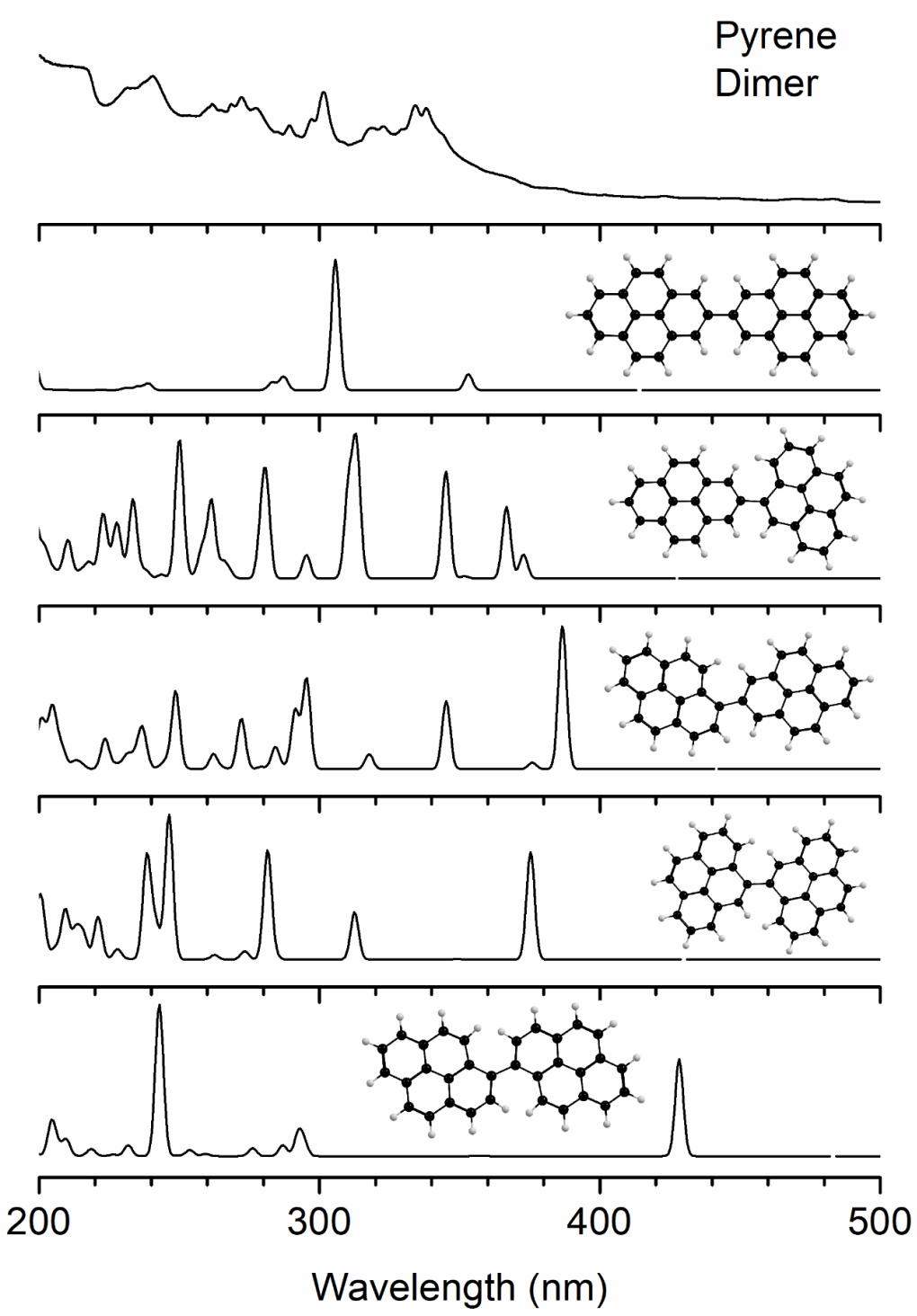

Figure 7.3. Comparison of pyrene singly-bonded dimers with experimental data. Theory transitions are scaled by 1.13 on the wavelength axis.

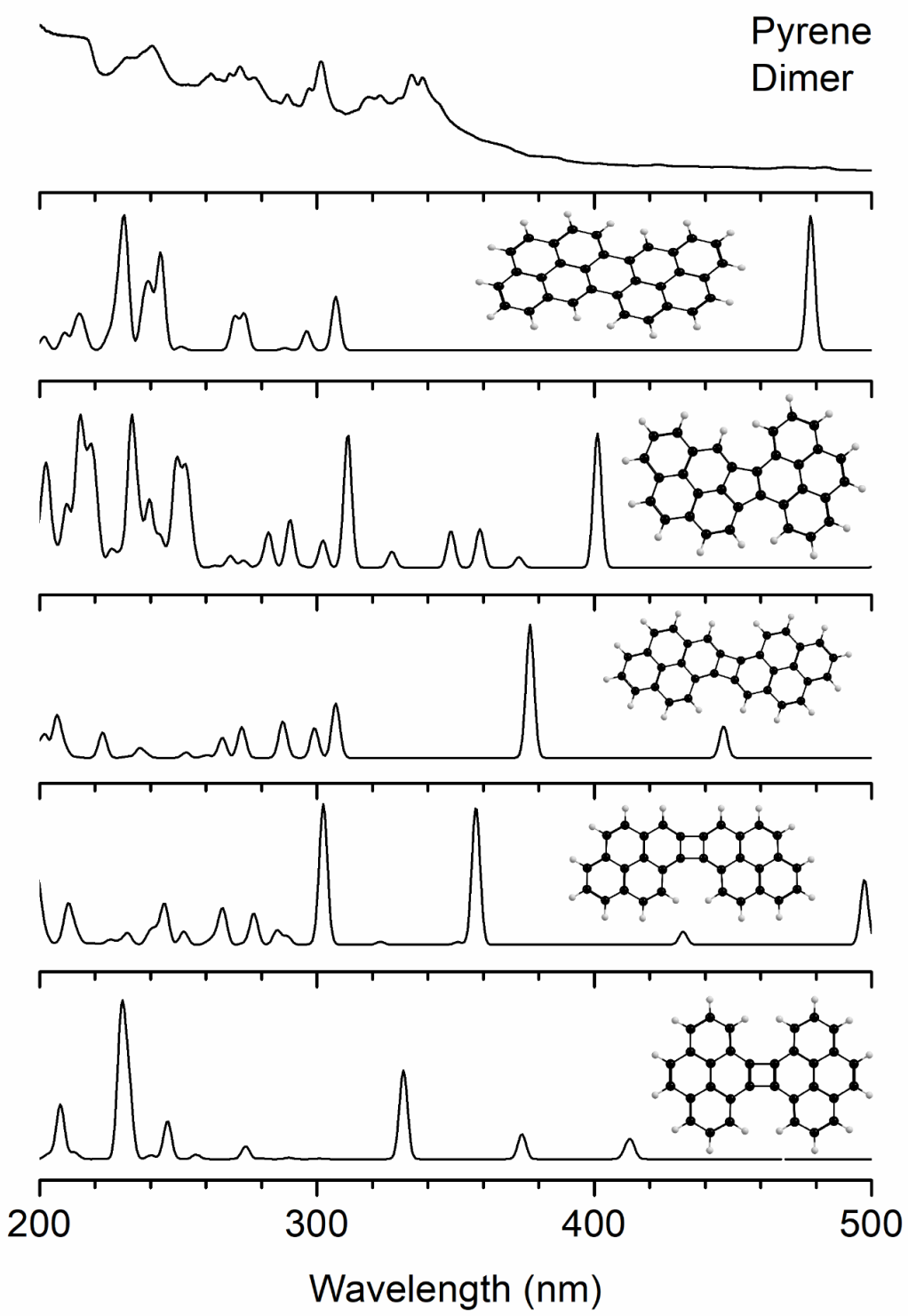

Figure 7.4. Comparison of pyrene doubly-bonded dimers with experimental data. Theory transitions are scaled by 1.13 on the wavelength axis.

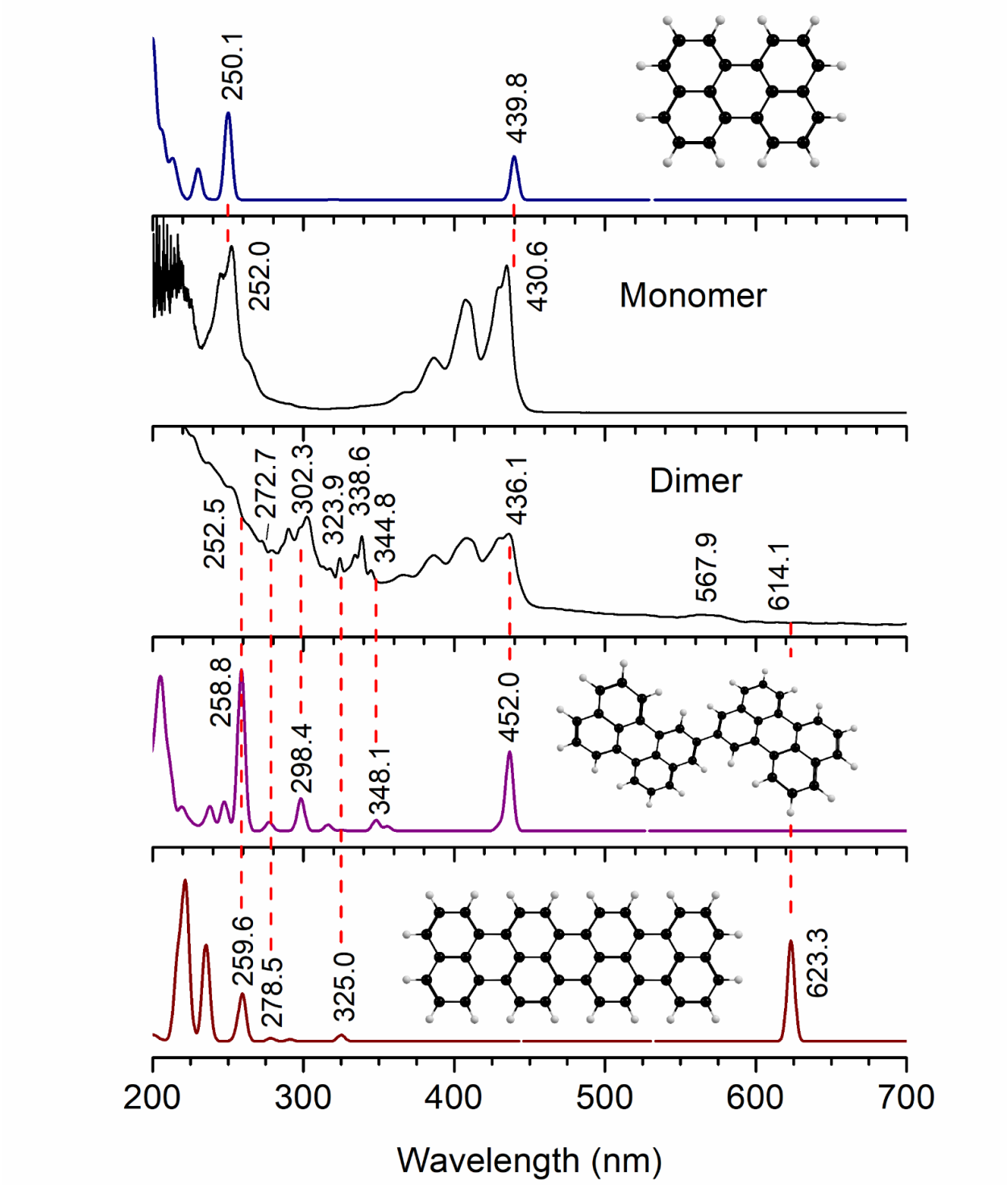

Figure 7.5. Comparison of perylene monomer and dimer dissolved in cyclohexane with most stable theoretical structures. Theory transitions were scaled by 1.13.

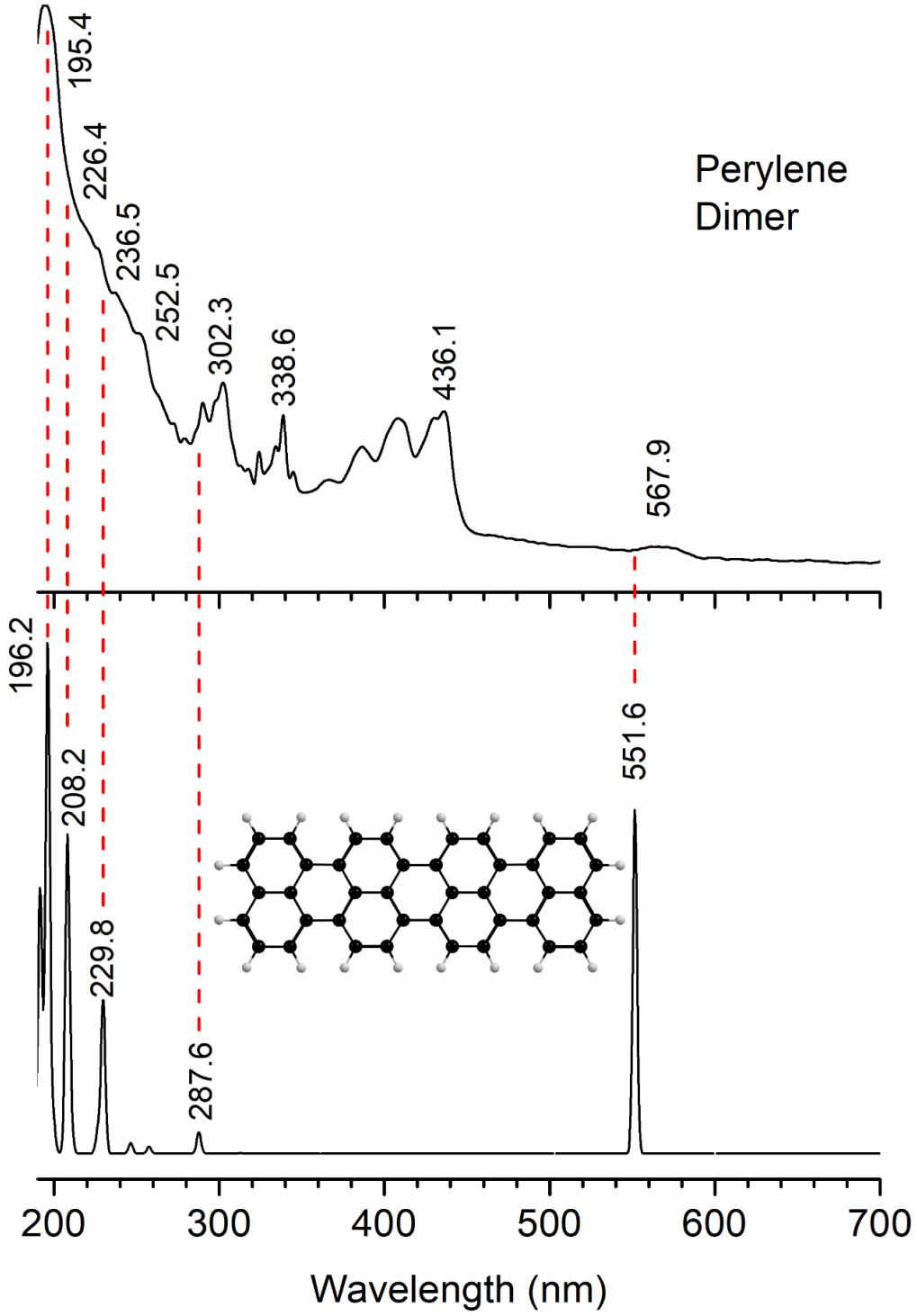

Figure 7.6. Comparison of perylene dimer dissolved in cyclohexane with theory dimer without scaling factor.

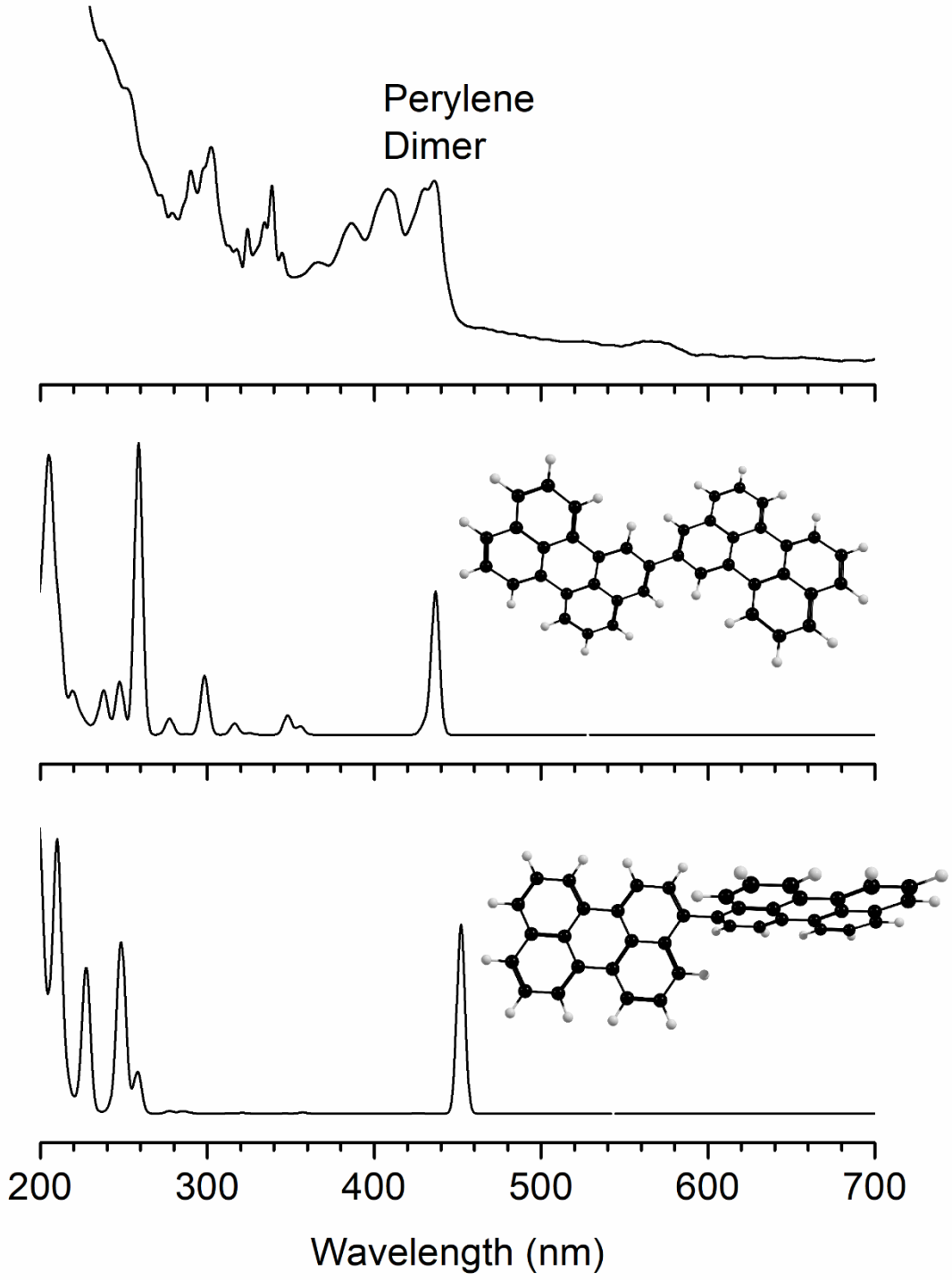

Figure 7.7. Comparison of perylene singly-bonded dimers with experimental data. Theory transitions are scaled by 1.13 on the wavelength axis.

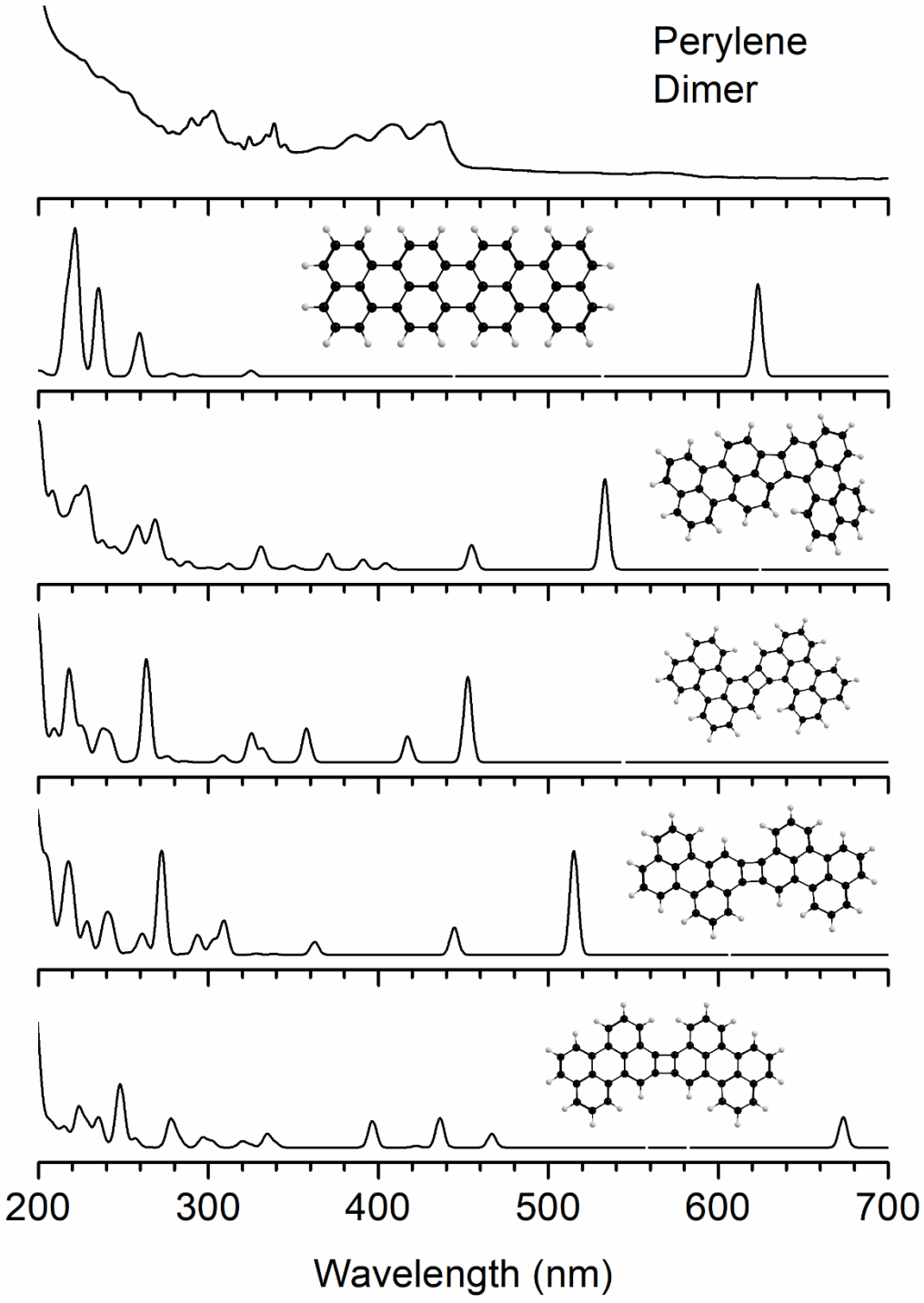

Figure 7.8. Comparison of perylene doubly-bonded dimers with experimental data. Theory transitions are scaled by 1.13 on the wavelength axis.

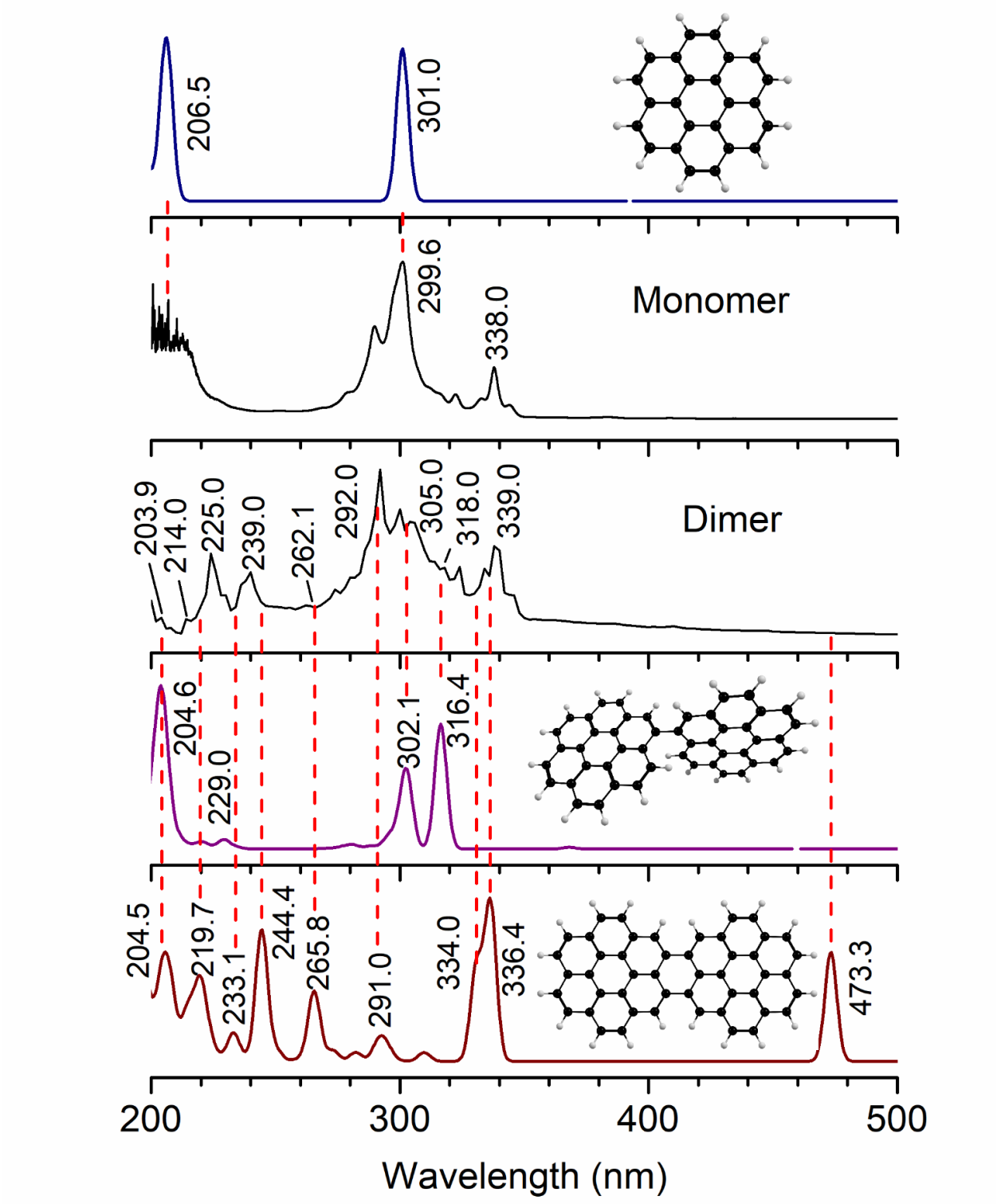

Figure 7.9. Comparison of coronene monomer and dimer dissolved in cyclohexane with most stable theoretical structures. Theory transitions were scaled by 1.13.

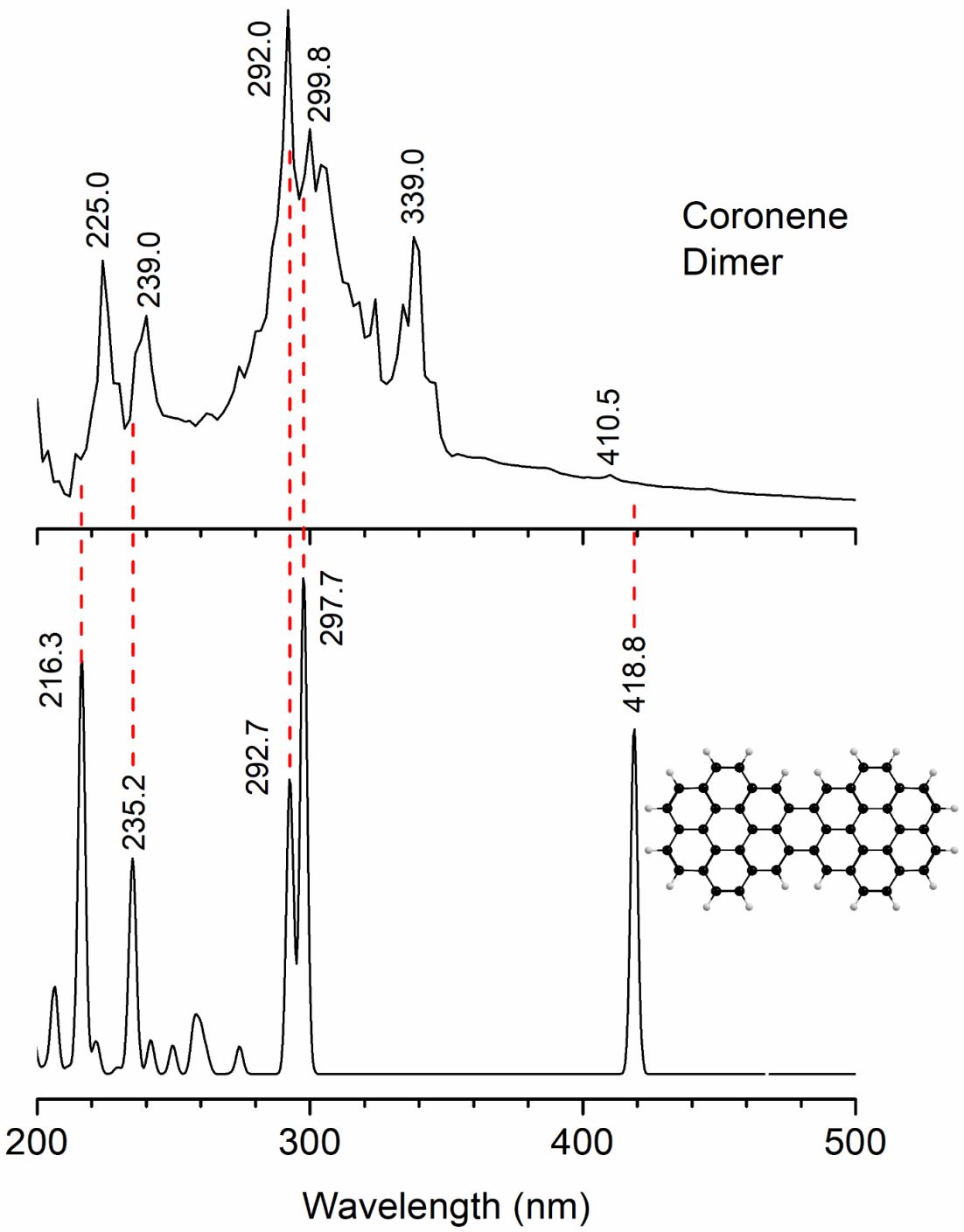

Figure 7.10. Comparison of coronene dimer dissolved in cyclohexane with theory dimer without any scaling factor.

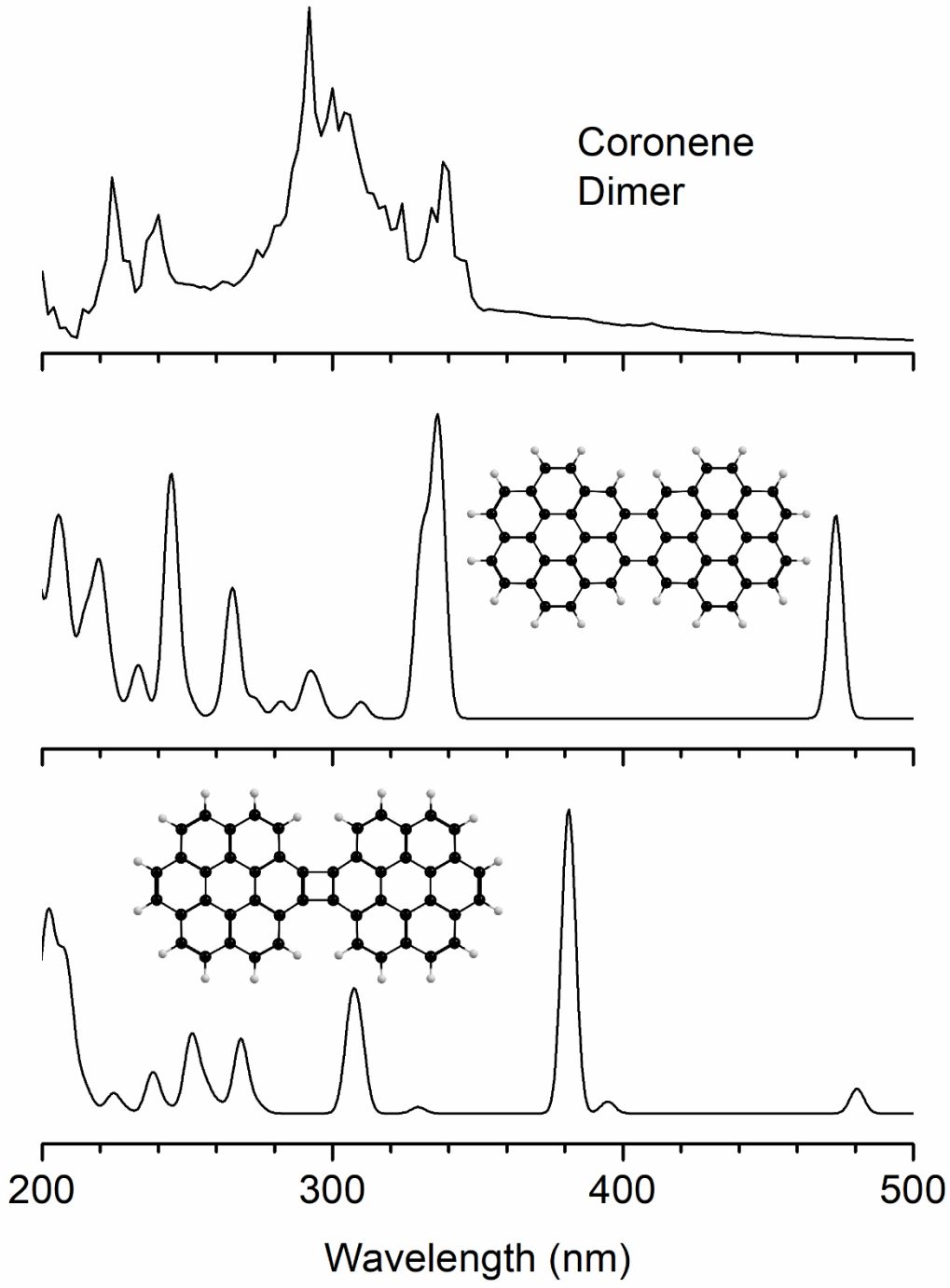

Figure 7.11. Comparison of coronene doubly-bonded dimers with experimental data. Theory transitions are scaled by 1.13 on the wavelength axis.

Chapter 8

Other Spectral Methods & Molecules

Although the focus of discussion has currently been on the vibrational and electronic transitions of pyrene, perylene, and coronene, several other methods were briefly examined. Unfortunately, these methods proved unsuccessful at identifying the dimer structures produced, but the issues with their attempts provide certain pieces of information about the dimers. The other methods here did not provide any conclusive evidence, but these methods may be further optimized to examine the formed dimer structures in the future.

Among the methods tried, one of the more successful was the study of dissolved PAHs with a high-performance liquid chromatography (HPLC). A new normal phase HPLC column was purchased specifically designed for use on aromatic molecules. The Phenogel column is a size selective column which allows larger molecules to pass through faster. Among the different PAHs studied, pyrene samples successfully yielded distinct results with a UV-Visible absorption multiwavelength detector. Figure 8.1 shows the resulting spectra of pyrene samples with a 0.1 mg/mL concentration dissolved in HPLC grade cyclohexane detected by the 230 nm wavelength detector. Similar results were obtained at other detection wavelengths. The first small peak around 4 minutes is attributed to the solvent cyclohexane, and the larger peaks are caused by different sized molecules. High purity dimer samples did not have multiple peaks for the monomer and dimer samples but had different elution time compared to the commercial monomer. Unfortunately, other samples did not yield similar results and even the pyrene sample took several tries to perfect.

An analysis of the spectral signatures would be ideal for confirmation of the theory based structures. Solid phase samples were examined by powder x-ray diffraction (XRD), but the mixture of different dimer samples made for a difficult analysis of the spectral signals. The addition of new peaks in the spectrum did indicate a change in the structures from the monomer, but these changes could be also caused by any sort of contaminants formed from the synthesis. Similarly, samples were also submitted for analysis with a scanning electron microscope (SEM). Samples were prepared by drop-casting onto silver substrates after being suspended in HPLC grade methanol. The resulting images were complex with no distinct shapes being easily noticeable. Samples were likely aggregated and may be a mixture of both singly and doubly-bonded species or contaminated with possible synthesis byproducts as shown in Figure 8.2. Samples would need to be exfoliated to try and produce single layer samples to analyze the structure. Similar studies were performed using atomic force microscopy on the same samples. No data was able to be obtained as the cantilever tip broke when attempting to scan the samples. Aggregated samples, as indicated by the SEM data, could have been thick enough to prevent the collection of microscopy data. One last attempt to acquire structural data was through the use of nuclear magnetic resonance (NMR) spectroscopy of samples dissolved in d12-cyclohexane purchased from Sigma-Aldrich as shown in Figure 8.3. The high symmetry of the PAH structures and limited purity of the dimer samples saw mostly the same ^{13}C peaks as present in the monomer samples. Although a couple of new peaks may have been present in the perylene samples, intensities were low. None of these methods provided conclusive evidence of the dimer structures synthesized in the experiment. Still some information can be gained from knowledge regarding the aggregated size of the dimers.

8.1 Other PAH Samples

In addition to pyrene, perylene, and coronene, other PAHs have been examined to determine some preliminary results. Samples of benzopyrene, pentacene and rubrene were studied beginning as before with the mass spectrometry studies. Benzopyrene, an isomer of perylene, has the potential to form a triply-bonded dimer structure. The thin film versus pellet spectra were nearly identical to the spectra for perylene with no particular contaminants and a sharp monomer peak at 252 m/z. Figure 8.4 shows the first peaks indicating the potential of being able to use benzopyrene as another PAH for synthesis. A sample of benzopyrene was run and even contained possible triply-bonded dimers as indicated in Figure 8.5. Purification was attempted on the samples but was not achieved after several attempts. Benzopyrene may be a future molecule to examine for similar synthesis properties, and the mass spectra data indicates possibly interesting dimer formation. Unfortunately, without further improvements to the purification process, benzopyrene dimer has yet to be isolated for spectroscopic analysis.

Pentacene is a linear acene made up of five aromatic rings. Initial mass spectra on the thin film of pentacene contained several interesting peaks, and close examination found the formation of both a ketone and quinone structure of pentacene. Figure 8.6 shows the thin film mass spectrum of pentacene with the ketone peaks at higher mass. Literature review found that these molecules were byproducts of pentacene's tendency to react with air. Pellet samples contained some curious dimer peaks that were higher in mass than the pentacene electrostatically-bound dimer. Samples were synthesized and purification was attempted, but much like benzopyrene, full purification was not achieved. Figure 8.7 examines the collected pentacene samples after attempted synthesis. The singular quinone peak which was previously at

310 m/z has almost completely disappeared. Despite the loss of the quinone peak, the dimer of the quinone around 582 m/z is the most prevalent dimer peak with even higher mass dimers also present. The addition of the ketone species created an increase in the difficulty of performing computations on the potential pentacene dimers and issues with purification and low dimer signal prevented pentacene spectra from being as thoroughly examined as the pyrene, perylene, and coronene PAHs examined in the earlier chapters. Pentacene could become an interesting molecule to continue studying in the future especially once theoretical calculation methods of PAHs have been improved.

The analysis of rubrene ended up being studied with a different piece of equipment that has not yet been explained. The results of that study are relegated to the following chapter to allow for a more in depth discussion of the findings.

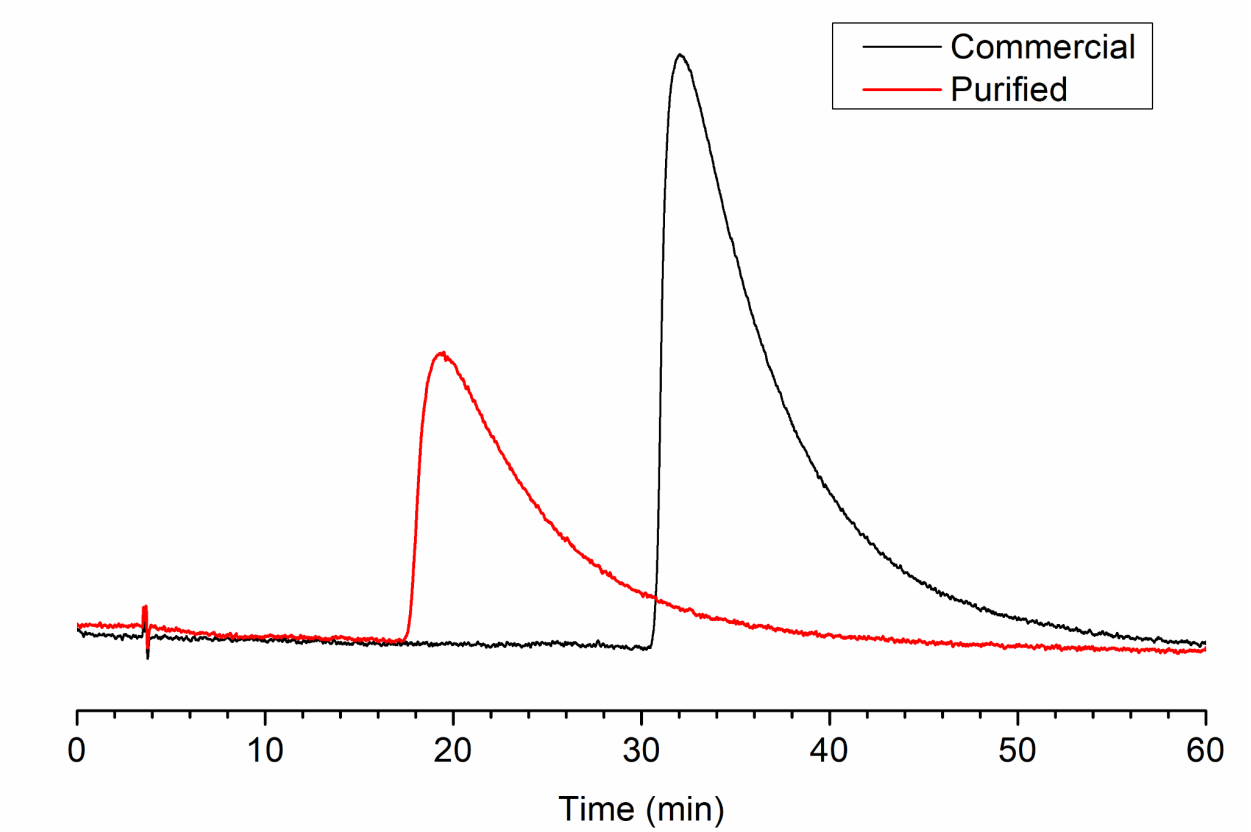

Figure 8.1. HPLC of pyrene and pyrene dimer in cyclohexane separated with a size-selection Phenogel column and detected with 230 nm wavelength detector. The onset peak around 4 minutes is a result of the solvent.

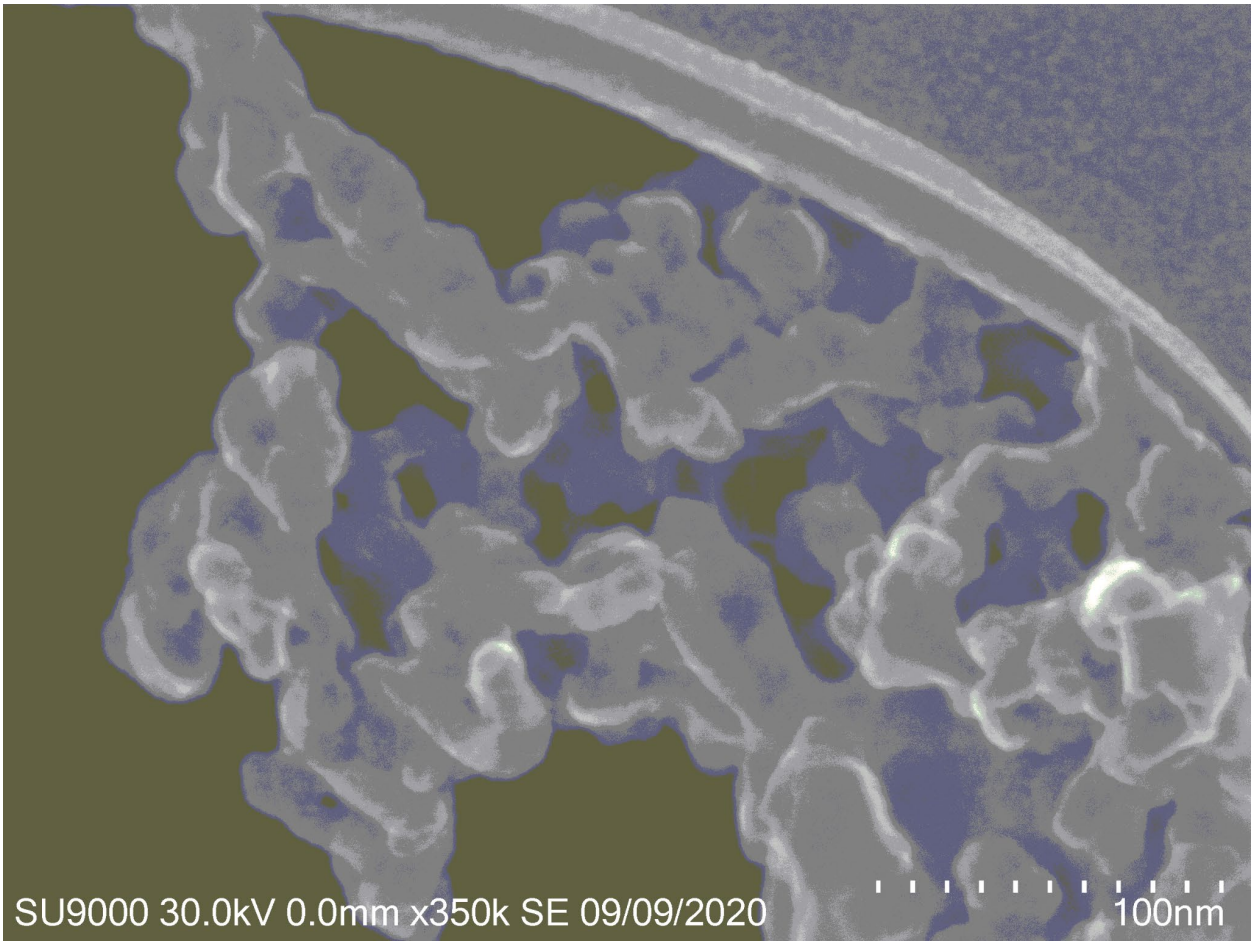

Figure 8.2. SEM image of perylene dimer.

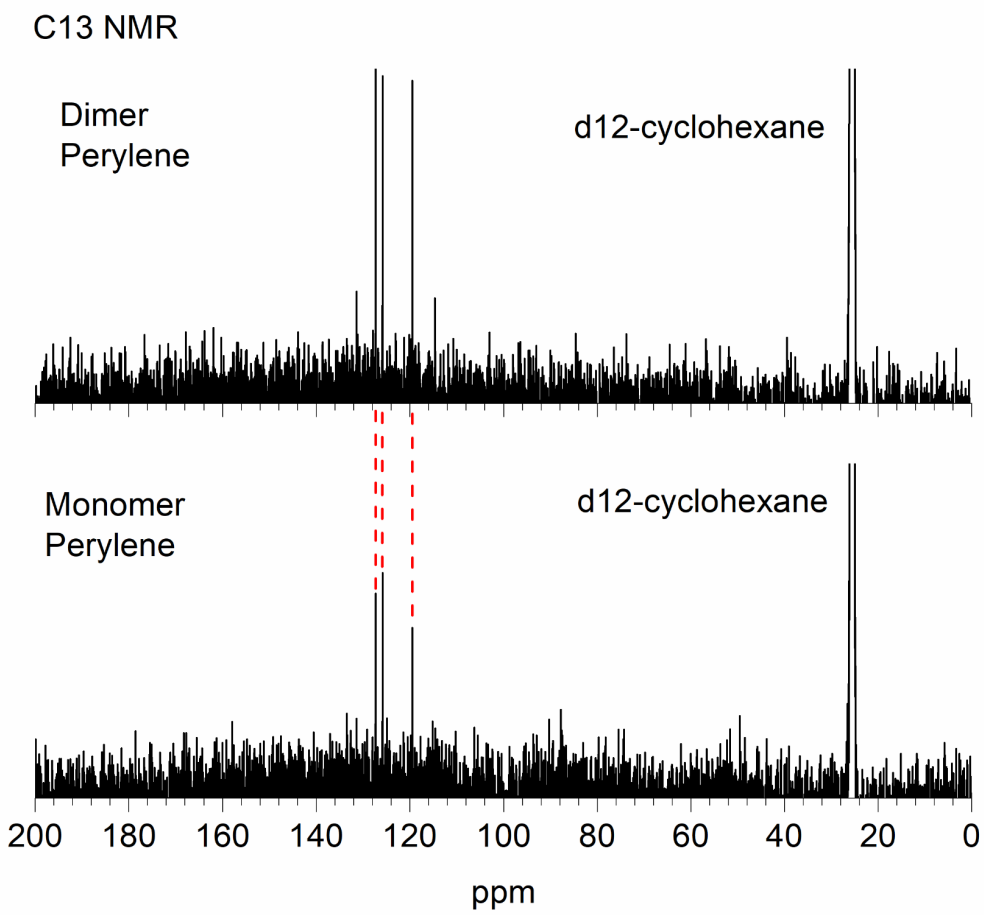

Figure 8.3. NMR of perylene dimer and monomer in d12-cyclohexane

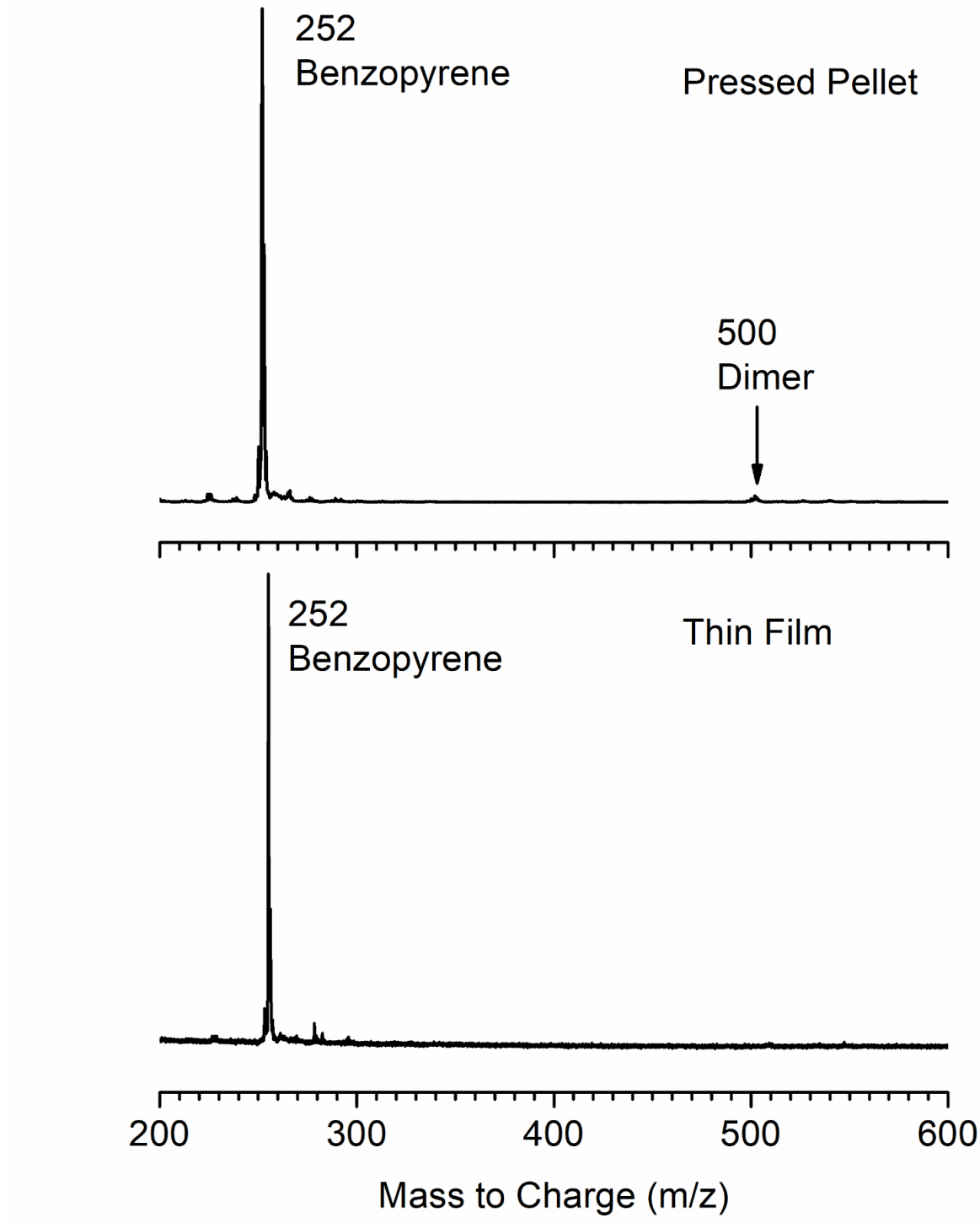

Figure 8.4. Thin film vs pressed pellet mass spectra of benzopyrene taken at 532 nm.

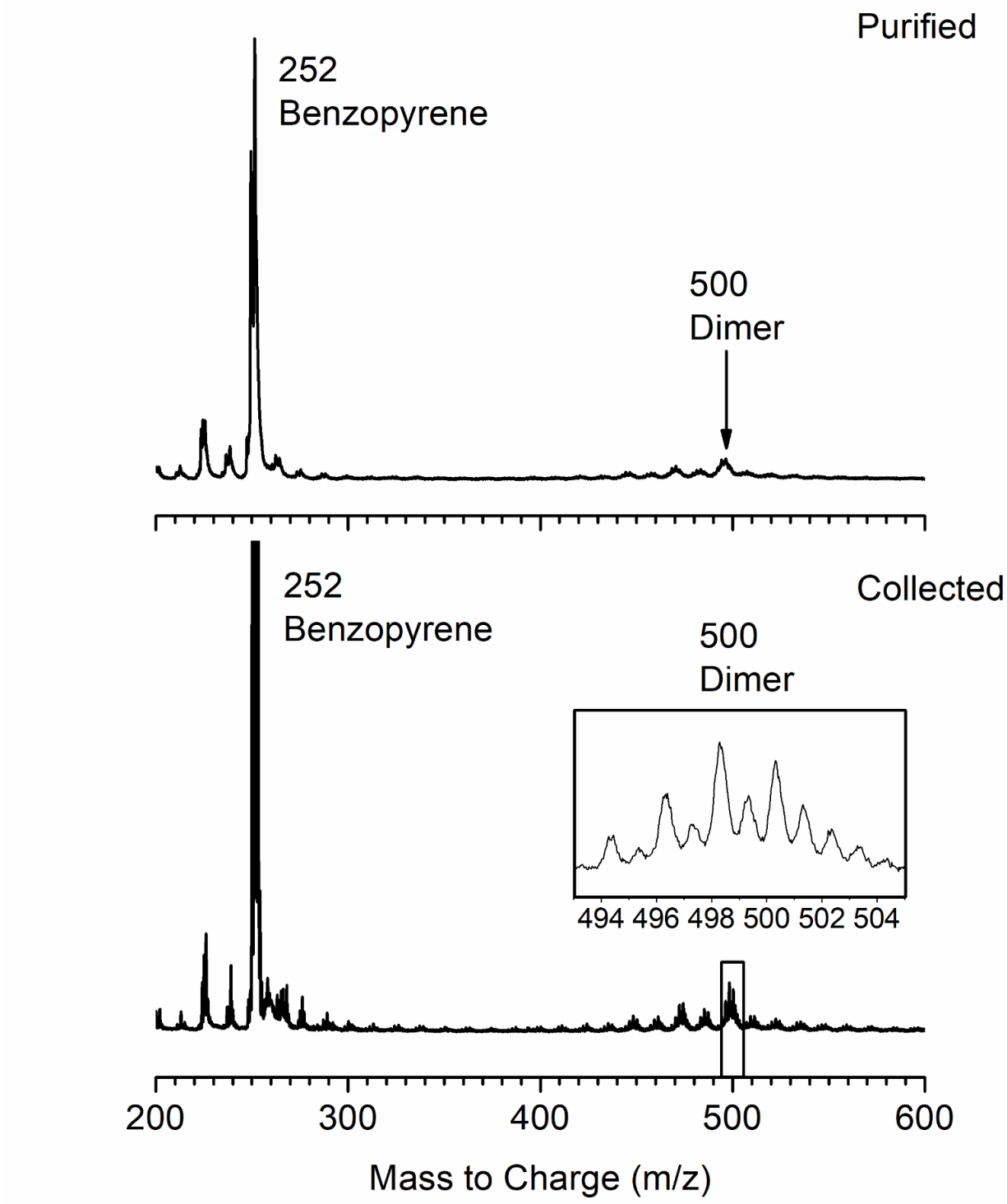

Figure 8.5. Collected vs purified mass spectra of benzopyrene at 532 nm.

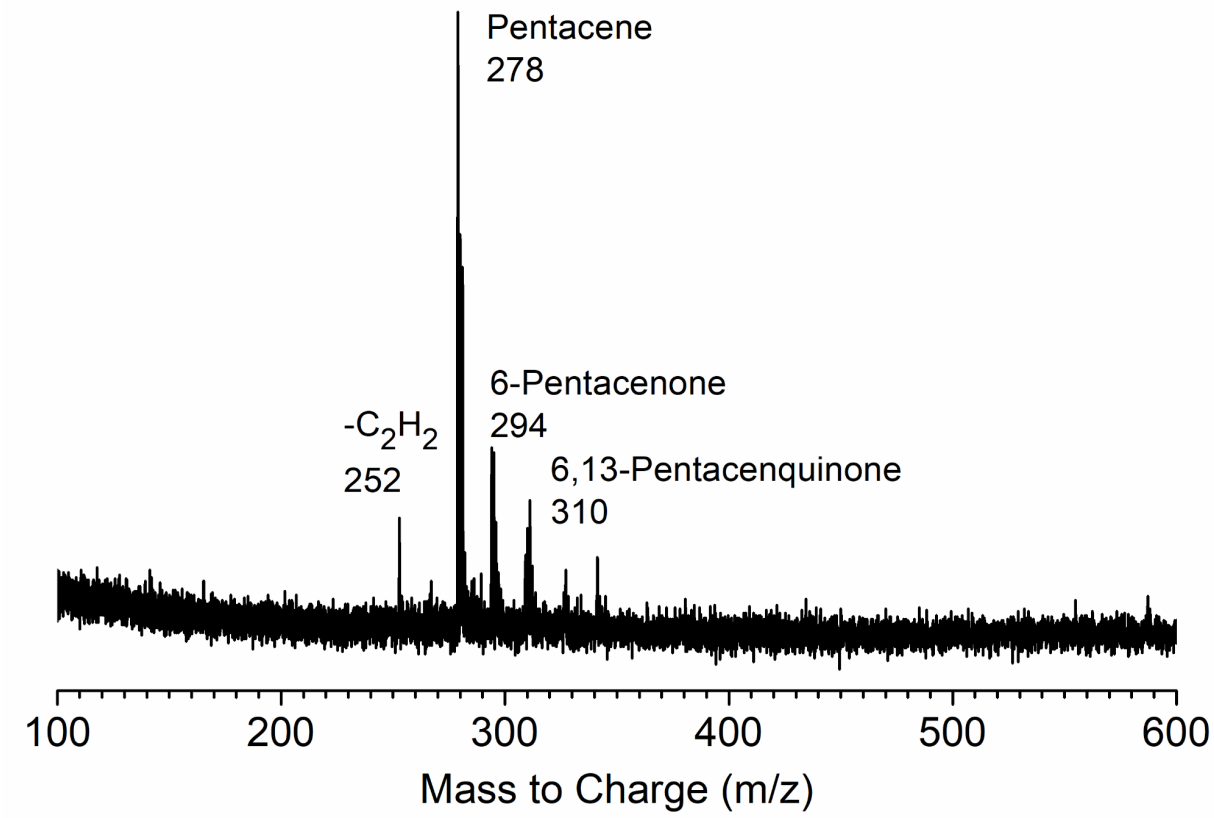

Figure 8.6. Thin film mass spectrum of pentacene taken at 355 nm.

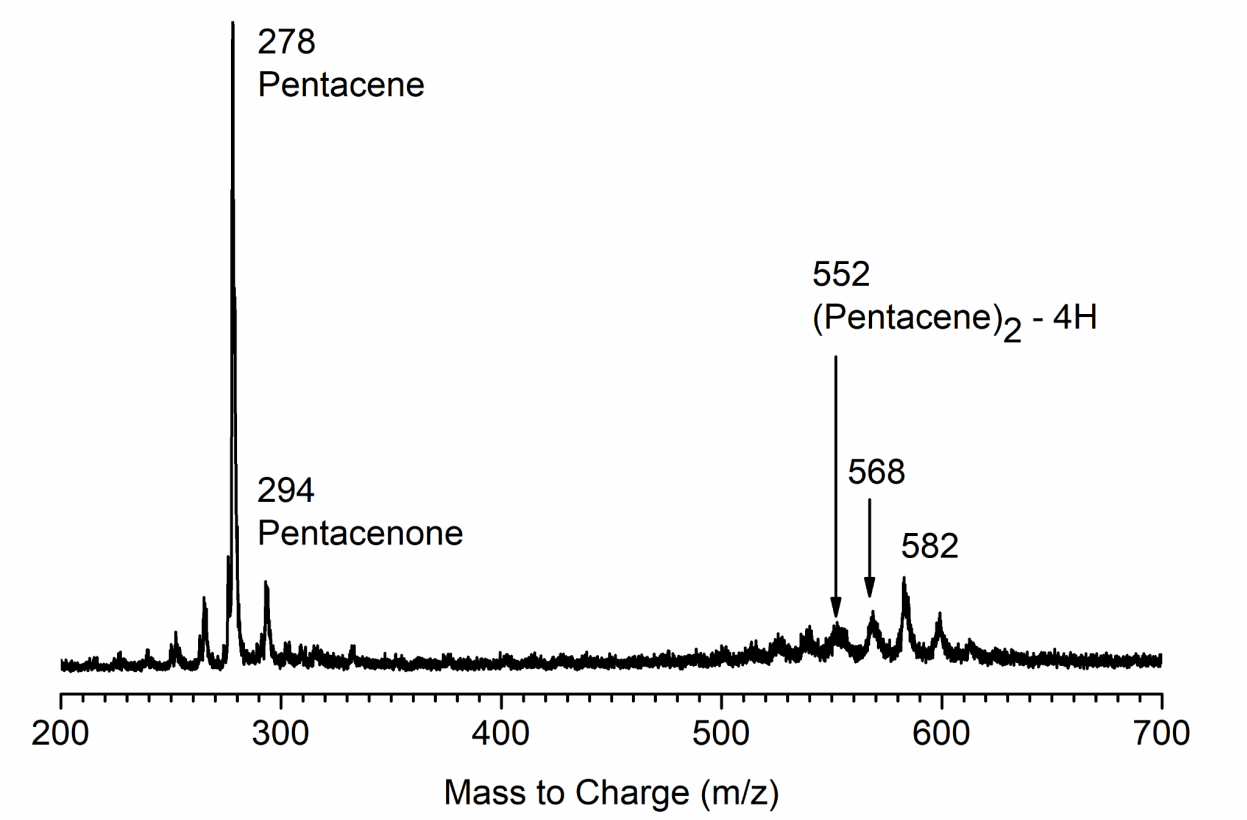

Figure 8.7. Collected pentacene sample mass spectrum at 355 nm after attempted purification.

Chapter 9

Mass Spectrometry & Photodissociation of Rubrene

Rubrene is an abnormally shaped PAH with four benzene rings bound orthogonally to the central two benzene rings of a tetracene body. It is also known to be capable of undergoing singlet fission making it a desirable molecule for further study. Rubrene was examined out of curiosity to investigate how possible dimer structures might form given the odd shape of the base molecule. However, before any oligomerization experiments could be performed, preliminary spectra on thin films and pressed pellets would need to be performed.

Initial mass spectra of rubrene contained peaks corresponding with the mass of rubrene and smaller mass peaks that correspond to masses of the loss of 1 and 2 phenyl groups from the parent rubrene. An example mass spectrum of the commercial rubrene pressed pellet is shown in Figure 9.1 along with the structure of rubrene. Additional mass peaks at m/z 167, 267, and 367 were discovered, but did not correspond with the loss of phenyl from a rubrene parent cation. Originally, the m/z 267 peak was presumed to correspond to a doubly-charged rubrene cation with a potential error of 1 amu, but later studies revealed this to be a false assumption. Mass spectra taken of both thin film and pressed pellet samples, at both 355 nm and 532 nm wavelengths, yielded the same results for commercial rubrene samples. No dimer peaks were present within the mass spectra for rubrene under similar conditions to the prior studied molecules.

To accompany the initial mass spectrometry studies, rubrene was also examined in molecular beam experiments. To prepare the sample for analysis, commercial rubrene sample

was loaded into a tungsten boat and sublimed under vacuum conditions, similar to those described in the purification of collected PAH dimers. Rubrene was heated to approximately 70°C to cause sublimation of the monomer. The sublimed material collected onto a rotating tungsten rod to produce an optically thick layer of PAH material for laser desorption analysis. The rubrene coated rod was attached to a translating, rotating motor within a high vacuum chamber for sample ablation. The external layer was desorbed through a focused Nd:YAG laser striking the tungsten rod within a laser desorption source commonly used within the Duncan lab.[2-3]

The resulting plume of material was skimmed into a second differentially pumped chamber and the ions were pulsed into the flight tube through charged plates similar to those described in Chapter 2. The resulting time-of-flight mass spectrum contained the same peaks as those seen in the LD-ToF-MS experiment and an example spectrum is shown in Figure 9.2. The rubrene peak was mass-selected through use of a biased deflection plate that was pulsed off to allow the rubrene ions through while repelling any other ions within the flight tube. The rubrene ions were deccelerated within a reflectron and struck with a 355 nm Nd:YAG photodissociation laser before being accelerated down a second flight tube to the detector. The resulting photodissociation mass spectrum of rubrene cation is presented in Figure 9.3. The difference mass spectrum is generated by subtraction of the mass selected spectrum resulting in the negative going rubrene parent peak. The two peaks that result from the photodissociation process correspond to the loss of one and two phenyl groups from the parent rubrene cation. No loss of a third phenyl group is detected from the photodissociation spectrum in agreement with the original laser desorption mass spectra taken.

In order to better understand the presence of the 267 m/z peak, the peak was also mass selected and analyzed under similar conditions with photodissociation as shown in Figure 9.3. Based on literature, the formation of rubrene is achieved through the fusion of two 1,1,3-triphenyl-2-propyn-1-ol molecules.[4] This triphenyl molecule without the hydroxide group has a molar mass of 267 amu, which matches the strange mass found in both spectrometers. The resulting photodissociation spectrum can be identified based on the mass losses present as depicted in Figure 9.4. These dissociation patterns also explain some of the lower mass peaks present within the pressed pellet spectrum in Figure 9.1.

Further analysis of these masses was done with theory calculations using the same methods presented in Chapter 4.[4] From these theoretical results, the most stable structures formed were determined. According to theory, the loss of the first phenyl group requires 54.3 kcal/mol of energy. Removal of a second phenyl group would require an additional 131.5 kcal/mol to reach the most stable structure missing two phenyl groups. However, a singular photon at 355 nm wavelength has 80.5 kcal/mol energy. The removal of two subsequent phenyl groups from the rubrene would require more than two photons worth of energy, yet the photodissociation shows the two phenyl loss as being the dominant product. To explain this phenomenon, the energy required to remove two phenyl groups by the production of a biphenyl fragment requires only 77.7 kcal/mol. Since the formation of biphenyl can reduce the energy required to under one photon, the process appears to be the favored dissociation route. The process for losing a third phenyl requires 105.5 kcal/mol more energy and can not be achieved with a two photon process even from the biphenyl loss structure. Example structures and energy barriers are depicted in Figure 9.5 with the most stable biphenyl loss structure shown. Both the mass spectrum and photodissociation spectrum do not contain peaks associated with the loss of

three phenyl groups from the rubrene parent ion in agreement with the high energy barrier calculated from theory.

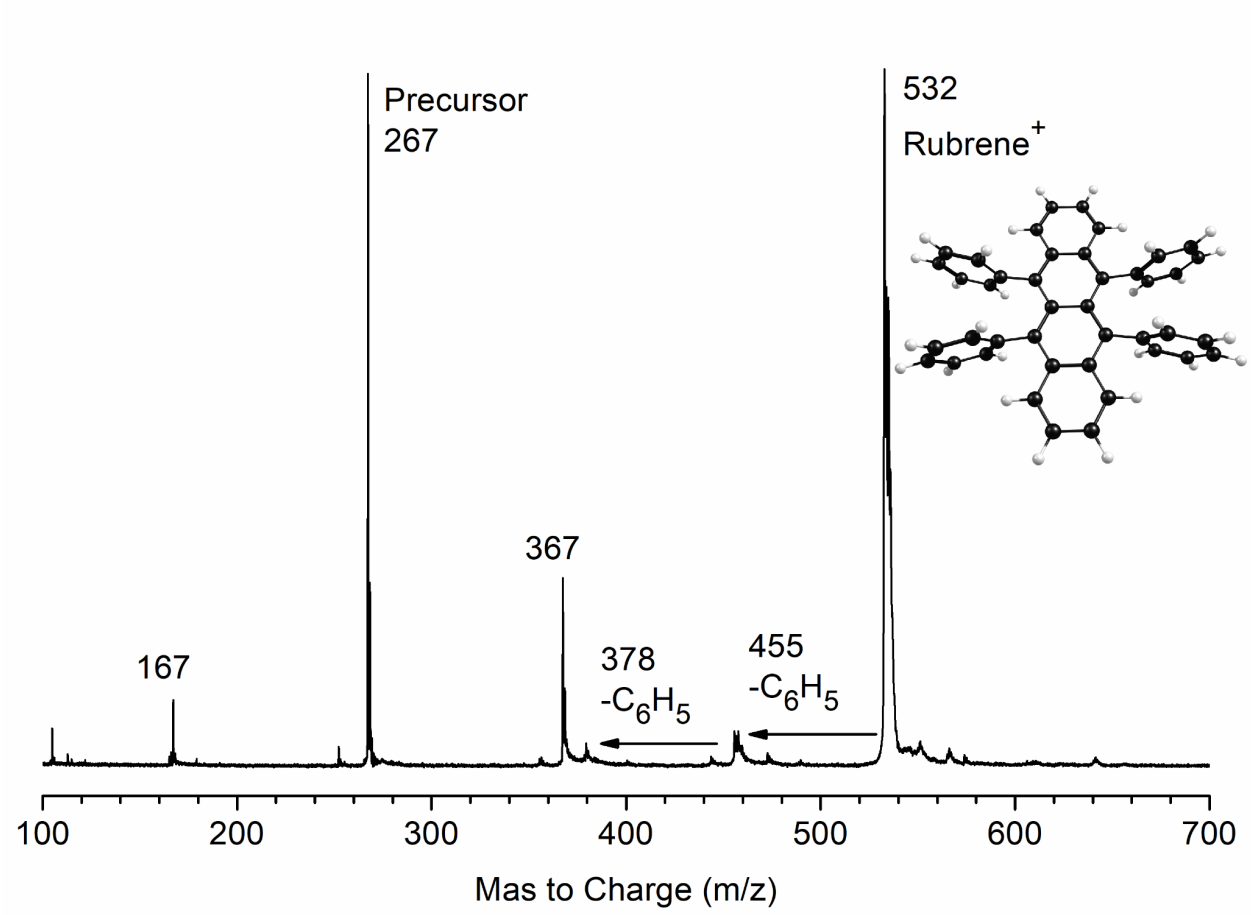

Figure 9.1. Mass spectrum of rubrene pressed pellet taken at 355 nm.

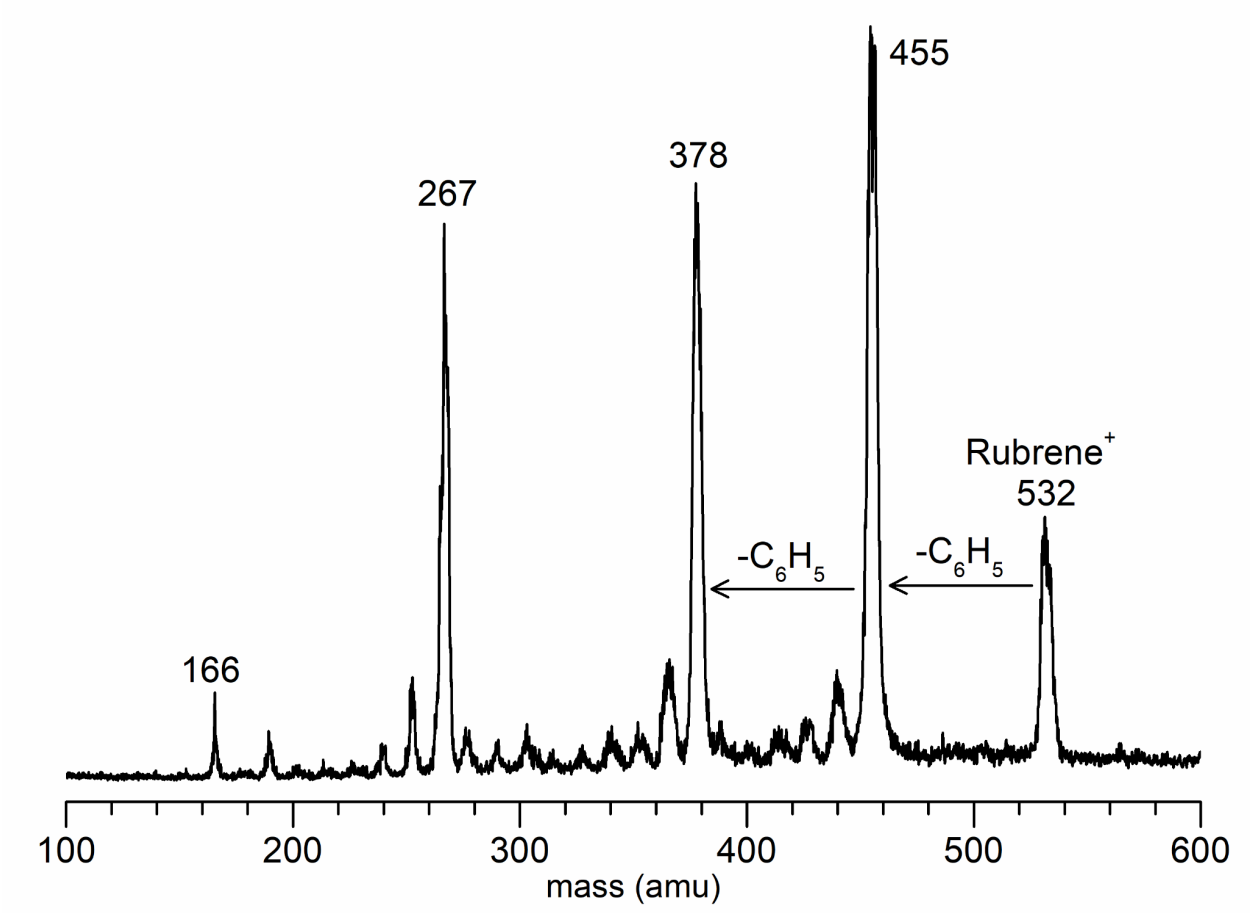

Figure 9.2. Laser desorption mass spectrum of rubrene coated tungsten rod with 355 nm desorption laser source.

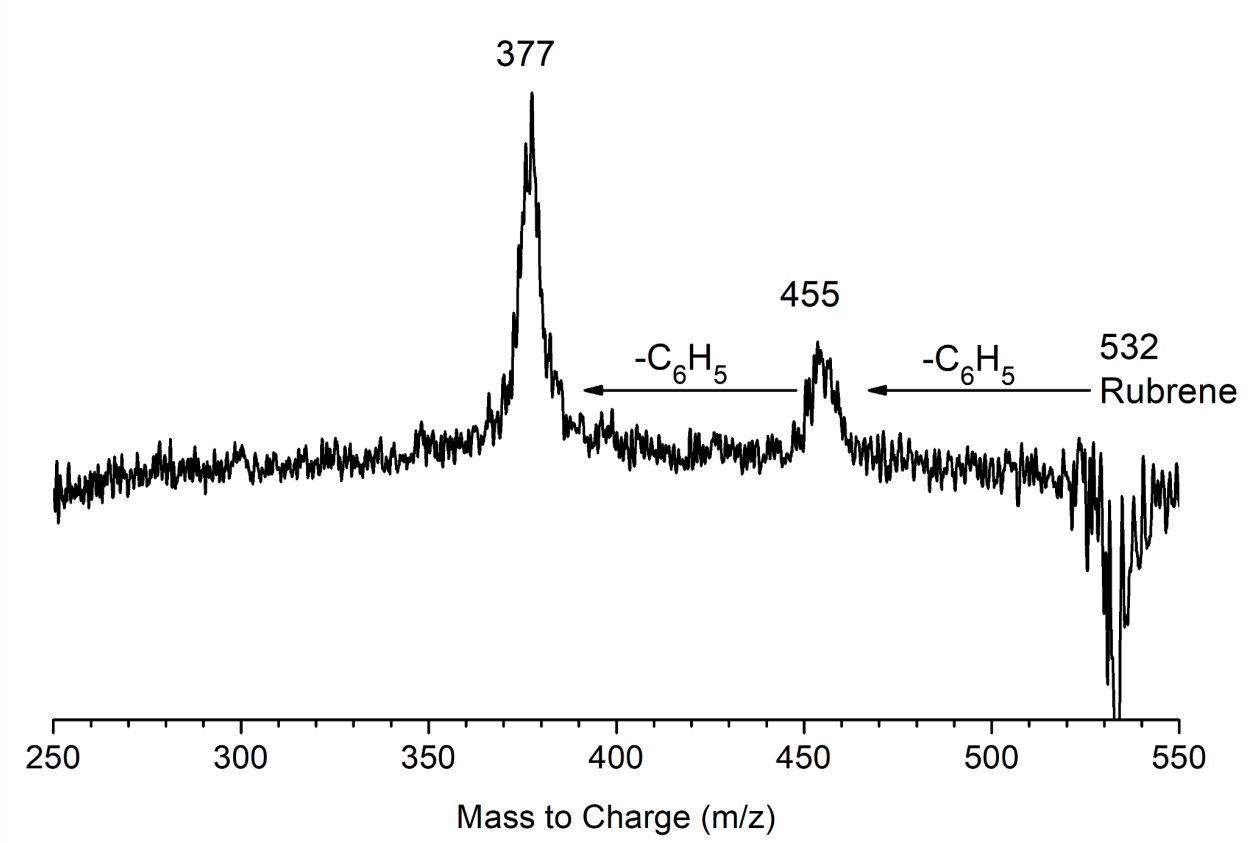

Figure 9.3. Photodissociation mass spectrum of rubrene with 355 nm Nd:YAG laser with 20 mJ of power.

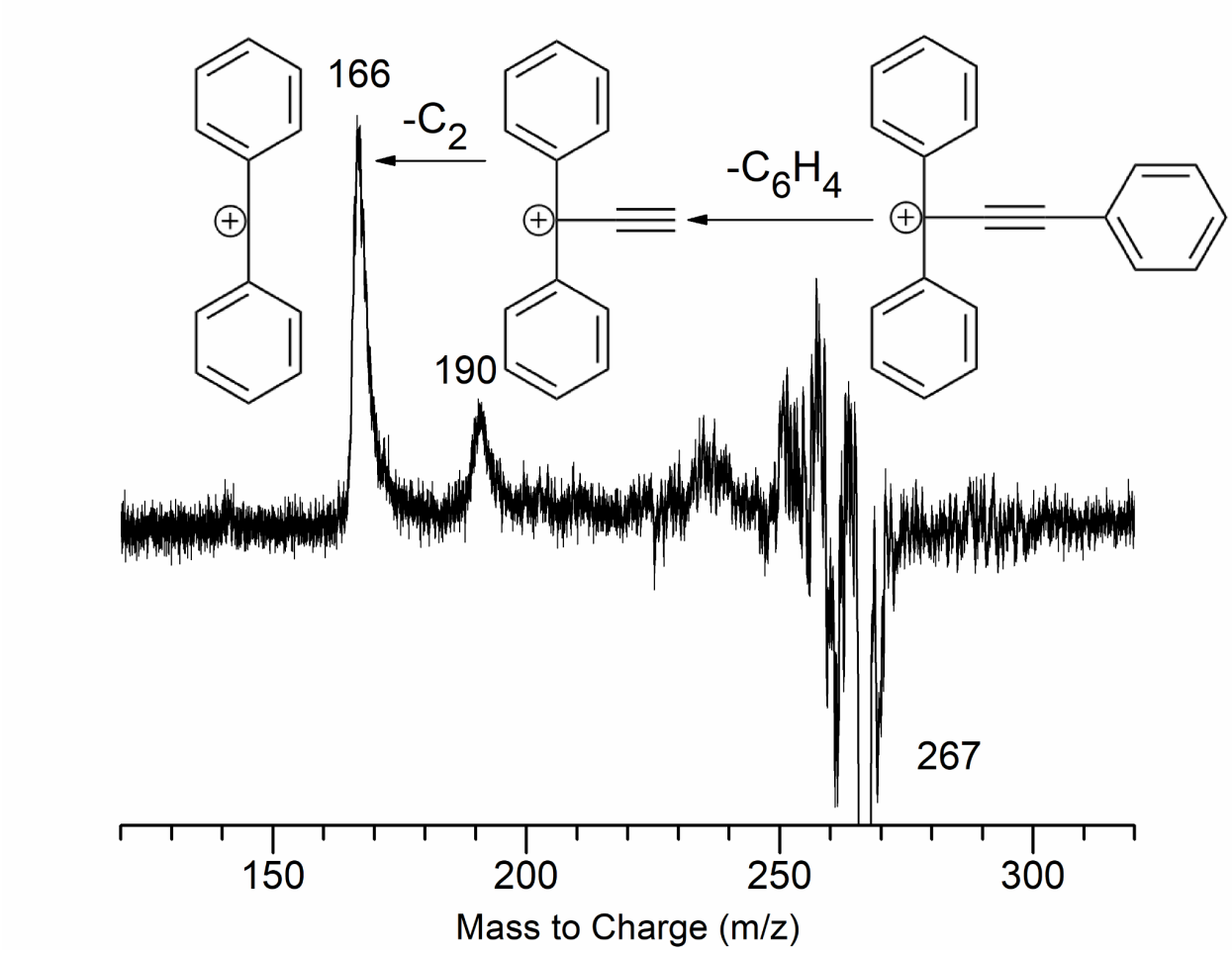

Figure 9.4. Photodissociation mass spectrum of the 267 m/z peak with 355 nm Nd:YAG laser with 20 mJ of power.

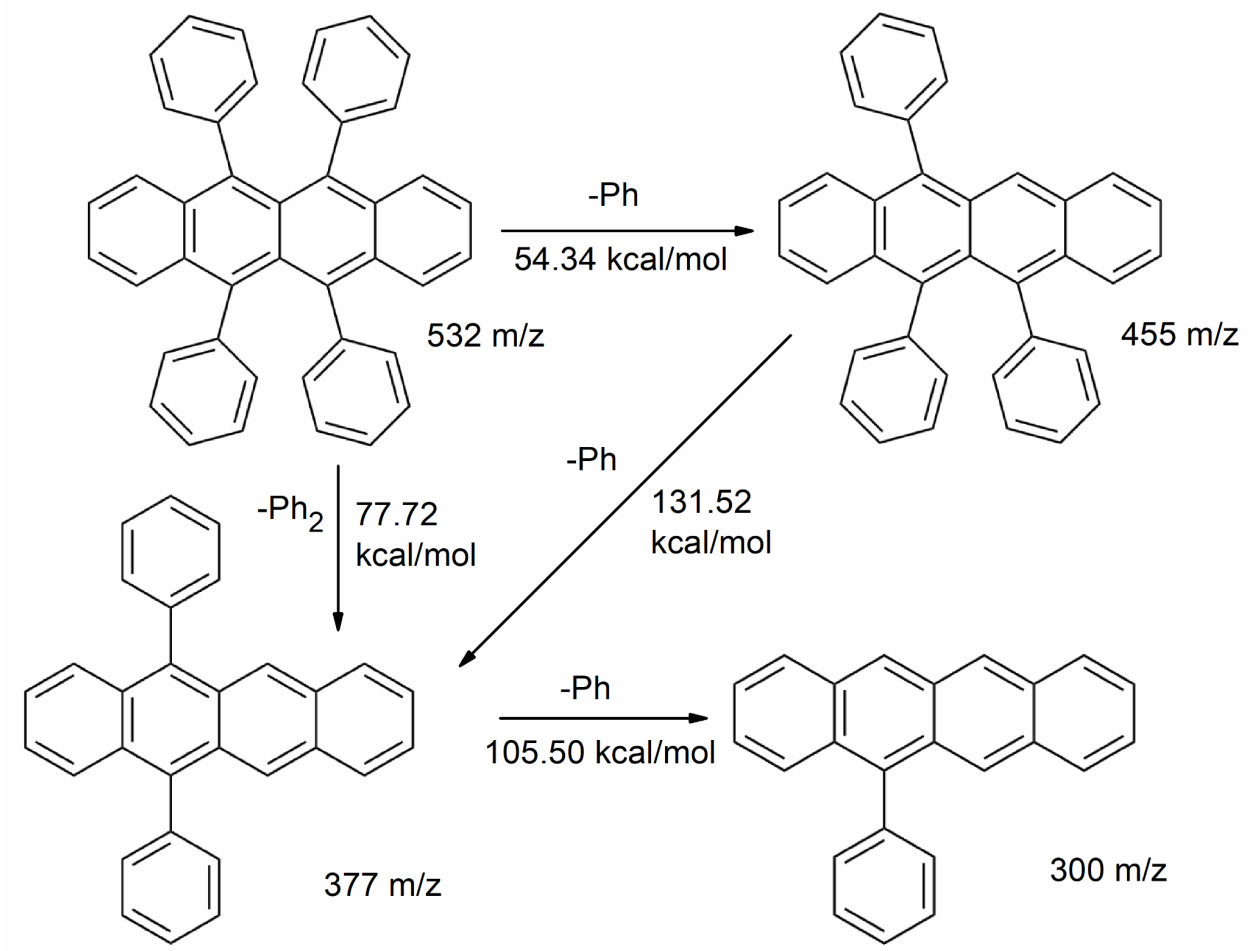

Figure 9.5. Theoretical energy differences between different rubrene phenyl losses.

References

1. Ma, L.; Zhang, K.; Kloc, C.; Sun, H.; Michel-Beyerle, M. E.; Gurzadyan, G. G. Singlet Fission in Rubrene Single Crystal: Direct Observation by Femtosecond Pump-Probe Spectroscopy. *Phys. Chem. Chem. Phys.* **2012**, *14*, 8307-8312.
2. Cornett, D. S.; Pescheke, M.; LaiHing, K.; Cheng, P. Y.; Willey, K. F.; Duncan, M. A. Reflectron Time-of-Flight Mass Spectrometer for Laser Photodissociation. *Rev. Sci. Instrum.* **1992**, *63*, 2177-2186.
3. LaiHing, K.; Cheng, P. Y.; Taylor, T. G.; Willey, K. F.; Peschke, M.; Duncan, M. A. Photodissociation in a Reflection Time-of-Flight Mass-Spectrometer: A Novel Mass Spectrometry/Mass Spectrometry Configuration for High-Mass Systems. *Anal. Chem.* **1989**, *61*, 1458-1460.
4. Furniss, B. *Vogel's Textbook of Practical Organic Chemistry* (5th ed.), Longman Scientific & Technical: Essex, England 1989.
5. Frisch, M. J.; Trucks, G. W.; Schlegel, H. B.; Scuseria, G. E.; Robb, M. A.; Cheeseman, J. R.; Scalmani, G.; Barone, V.; Petersson, G. A.; Nakatsuji, H.; Li, X.; Caricato, M.; Marenich, A. V.; Bloino, J.; Janesko, B. G.; Gomperts, R.; Mennucci, B.; Hratchian, H. P.; Ortiz, J. V.; Izmaylov, A. F.; Sonnenberg, J. L.; Williams-Young, D.; Ding, F.; Lipparini, F.; Egidi, F.; Goings, J.; Peng, B.; Petrone, A.; Henderson, T.; Ranasinghe, D.; Zakrzewski, V. G.; Gao, J.; Rega, N.; Zheng, G.; Liang, W.; Hada, M.; Ehara, M.; Toyota, K.; Fukuda, R.; Hasegawa, J.; Ishida, M.; Nakajima, T.; Honda, Y.; Kitao, O.; Nakai, H.; Vreven, T.; Throssell, K.; Montgomery, J. A., Jr.; Peralta, J. E.; Ogliaro, F.; Bearpark, M. J.; Heyd, J. J.; Brothers, E. N.; Kudin, K. N.; Staroverov, V. N.; Keith, T.

A.; Kobayashi, R.; Normand, J.; Raghavachari, K.; Rendell, A. P.; Burant, J. C.; Iyengar, S. S.; Tomasi, J.; Cossi, M.; Millam, J. M.; Klene, M.; Adamo, C.; Cammi, R.; Ochterski, J. W.; Martin, R. L.; Morokuma, K.; Farkas, O.; Foresman, J. B.; Fox, D. J. *Gaussian16*, Revision C.01, Gaussian, Inc.: Wallingford CT, 2016.